

1 Minute-scale oscillatory sequences in medial entorhinal cortex

2

3

4 Soledad Gonzalo Cogno¹, Horst A. Obenaus¹, R. Irene Jacobsen¹, Flavio Donato^{2*}, May-Britt Moser^{1*},
5 Edvard I. Moser^{1*}

6

7 ¹Kavli Institute for Systems Neuroscience and Centre for Neural Computation, Norwegian University of
8 Science and Technology, Trondheim, Norway; ²Biozentrum Universität Basel, Spitalstrasse 41, 4056,
9 Basel, Switzerland.

10

11

12 *Equal contribution.

13

14 Corresponding authors: Soledad Gonzalo Cogno, soledad.g.cogno@ntnu.no; Flavio Donato,
15 flavio.donato@unibas.ch; May-Britt Moser, may-britt.moser@ntnu.no; Edvard I. Moser,
16 edvard.moser@ntnu.no

17

18 Editorial correspondence: edvard.moser@ntnu.no

19

20

21 Abstract

22 The medial entorhinal cortex (MEC) hosts many of the brain's circuit elements for spatial navigation and
23 episodic memory, operations that require neural activity to be organized across long durations of
24 experience¹. While location is known to be encoded by a plethora of spatially tuned cell types in this
25 brain region²⁻⁶, little is known about how the activity of entorhinal cells is tied together over time. Among
26 the brain's most powerful mechanisms for neural coordination are network oscillations, which
27 dynamically synchronize neural activity across circuit elements⁷⁻¹⁰. In MEC, theta and gamma oscillations
28 provide temporal structure to the neural population activity at subsecond time scales^{1,11-13}. It remains
29 an open question, however, whether similarly powerful coordination occurs in MEC at behavioural time
30 scales, in the second-to-minute regime. Here we show that MEC activity can be organized into a minute-
31 scale oscillation that entrains nearly the entire cell population, with periods ranging from 10 to 100
32 seconds. Throughout this ultraslow oscillation, neural activity progresses in periodic and stereotyped
33 sequences. This activity was elicited while mice ran at free pace on a rotating wheel in darkness, with no
34 change in its location or running direction and no scheduled rewards. The oscillation sometimes
35 advanced uninterruptedly for tens of minutes, transcending epochs of locomotion and immobility.
36 Similar oscillatory sequences were not observed in neighboring parasubiculum or in visual cortex. The
37 ultraslow oscillation of activity sequences in MEC may have the potential to couple its neurons and
38 circuits across extended time scales and to serve as a scaffold for processes that unfold at behavioural
39 time scales, such as navigation and episodic memory formation.

40

41

42

43

44 Main

45 Brain function emerges from the dynamic coordination of interconnected neurons^{9,10,14-16}. At subsecond
46 time scales, cells are coordinated within and across dispersed brain regions by way of neuronal
47 oscillations^{7,9,13,17-20}. Studies have reported oscillations also at slower time scales, with periods lasting
48 from seconds to minutes, in individual neurons²¹⁻²⁶ and in local field potentials²⁷⁻²⁹. It remains unknown,
49 however, how pervasive these ultraslow oscillations are, whether they serve a role in neuronal
50 coordination, and if they do, how the activity of participating neurons is organized in space and time
51 across the neural circuit.

52 We directed our search for ultraslow oscillations to the medial entorhinal cortex (MEC), a brain circuit
53 that by containing many of the elements for navigational behavior²⁻⁶ and episodic memory
54 formation^{1,30,31}, may possess mechanisms to organize neural activity at time scales of seconds to
55 minutes. Ultraslow oscillations, if they exist in MEC, might structure neural activity over long time scales
56 and interact with faster oscillations, such as theta and gamma rhythms, which are predominant in this
57 brain area^{11,12,32}. To maximize the detectability of ultraslow MEC oscillations and to rule out variations
58 in external stimuli as sources of modulation, we monitored activity in hundreds of MEC cells with two-
59 photon calcium imaging while head-fixed mice ran on a rotating wheel for 30 or 60 minutes³³⁻³⁵, in
60 darkness and with no scheduled rewards^{36,37} (Fig. 1a).

61

62 *Activity of MEC neurons undergoes ultraslow oscillations*

63 Behavior on the rotating wheel was characterized by bouts of running, at variable speed and
64 acceleration, interleaved with periods of rest (Extended data Fig. 2a). To determine if neural activity in
65 MEC exhibits ultraslow oscillations in this task, for each recorded cell we deconvolved the calcium
66 signals^{38,39} and binarized the obtained signals, using a bin size of 129 ms. This process yielded a
67 deconvolved and binary calcium activity that had in each time bin a value of 1 in presence of calcium
68 events, and 0 otherwise (“calcium activity” for the rest of the paper). For each cell, we calculated the
69 autocorrelation of the calcium activity and the corresponding power spectral density (PSD). When the
70 autocorrelation diagrams of all cells from one session were stacked into a matrix with cells as rows and
71 time lags as columns, we observed vertical bands (Fig. 1b, left), suggesting that the calcium activity of
72 individual cells was oscillatory and that many cells shared a similar oscillation frequency. When sorting
73 the autocorrelations in the matrix according to the frequency at which the PSDs peaked (“primary
74 frequency”), the spread of oscillatory frequencies became clearer (Fig. 1b, right). Some cells had only
75 one prominent peak in their PSD (Fig 1c), suggesting that they were active at equidistant intervals
76 throughout the session. Other cells had several peaks, often with the higher frequencies appearing as
77 harmonics of a fundamental frequency, or they had wider peaks, indicating more variable activity
78 intervals (Fig. 1d and e). In the example session in Fig. 1b, most cells (72%, 348 of 484) had a primary
79 frequency lower than 0.01 Hz (44% of the cells had a primary frequency within the range 0.006-0.008
80 Hz), and there were no cells whose PSD peaked at frequencies higher than 0.1 Hz. In the complete data
81 set (15 sessions over 5 animals), there was some variation in frequencies across sessions and animals
82 but the primary frequency was always below 0.1 Hz (all 6231 cells; range of maximum frequencies across
83 15 sessions: 0.036-0.057 Hz). Taken together, these findings demonstrate ultraslow oscillations of single
84 cell calcium activity in MEC, at periods in the order of tens of seconds to minutes.

85

86

87

88

89 ***MEC population activity is organized into oscillatory sequences***

90 To determine whether the ultraslow oscillation of calcium activity of different cells is coordinated and
91 temporally structured at the neural population level, we introduced a two-step procedure. First, we
92 stacked the calcium activity of all cells to produce a matrix that had as many rows as recorded cells, and
93 as many columns as time bins (bin size 129 ms). Second, using time bins as data points, we calculated
94 instantaneous correlations between the calcium activity of all pairs of cells, and used these values to
95 sort the cells such that those that are nearby in the sorting are highly synchronized. The cell pair with
96 the highest correlation value was identified and one of the two cells was defined as the “lead” cell. The
97 remaining cells were sorted, in a descending manner, based on their correlation value with the lead cell.

98 When cells were sorted by correlations and their activity plotted across session time, we observed
99 periodic sequences of neuronal activation (Fig. 2a). The sequences unfolded successively at a steady
100 rate, with no interruption for tens of minutes. The periodic sequences indicate the presence of an
101 oscillation at the neural population level that coordinates the order of activity among the neurons. Each
102 cell was followed first by cells that were highly synchronous, and then successively by less synchronous
103 cells until synchronization caught up again (Extended data Fig. 3a).

104 While sorting cells according to their correlation values unveiled recurring sequences of activity,
105 computing correlations from the binarized calcium activity (or the raw calcium signals) can be inherently
106 noisy due to variability in the frequency of deconvolved calcium events and dependence on fine tuning
107 of hyperparameters such as the size of the kernel used to smooth the calcium activity. Thus, we sought
108 a sorting approach that did not rely on hyperparameters. We leveraged the fact that sequences of
109 activity constitute low-dimensional dynamics with intrinsic dimensionality equal to 1, and adopted an
110 unsupervised approach based on dimensionality reduction⁴⁰ to sort the cells. For each recording session
111 we applied principal component analysis (PCA) to the full matrix of calcium activity, including all epochs
112 of movement and immobility. We kept the first two principal components (PCs), which is the minimum
113 number of components needed to embed non-linear 1-dimensional dynamics. Expecting that the
114 ordering in cell activation would be expressed in the relationship between the cells’ loadings on the two
115 PCs, we measured for each cell the angle $\theta \in [-\pi, \pi)$ of the vector defined by the pair of loadings on
116 PC1 and PC2, and then sorted the neurons based on these angles in a descending manner (Extended
117 data Fig. 3b). Sorting the cells in this way (“PCA method”) revealed the same stereotyped sequences of
118 neuronal activation that we previously found through correlations among cell pairs (Fig. 2b); however,
119 the sequential organization was now more salient. Sequences proceeded uninterruptedly in a periodic
120 manner and seemed to involve the majority of the recorded MEC cells. We will refer to these oscillatory
121 sequences as the “population oscillation” to distinguish them from oscillations in single cell calcium
122 activity. The population oscillation was not present if cells were not sorted or if the PCA method was
123 applied to matrices of calcium activity in which the calcium events were temporally shuffled (Extended
124 data Fig. 3c, first and second row on the left). The population oscillation was similarly observed when
125 neurons were sorted according to unsupervised methods relying on a variety of non-linear
126 dimensionality reduction techniques (Extended data Fig. 3c, third row on the left, and second column),
127 and also when the neurons’ calcium activity was visualized by the unprocessed calcium signals (Fig. 2c),
128 suggesting that it is not an artifact of the spike deconvolution.

129 Since sequences of neural activity constitute low-dimensional dynamics, we next asked what is the
130 topology of the underlying manifold. First, we visualized the manifold by projecting the population
131 activity onto the first two PCs. The manifold resembled a ring, along which the population activity
132 propagated repeatedly with periodic boundary conditions (Fig. 2d left, Extended data Fig. 3d). However,
133 because the ring-shaped manifold could be lying on a curved surface, in which case the linear embedding
134 of PCA might result in distortions when the manifold is visualized, we next adopted a non-linear
135 dimensionality reduction method. A Laplacian Eigenmap (LEM) approach was chosen because it has a

136 lower number of hyperparameters as compared to the other non-linear techniques (Extended data Fig.
137 3c). We applied LEM to the matrix of calcium activity and then projected the population activity onto
138 the 2-dimensional embedding spanned by the first two LEM dimensions. The manifold still had the shape
139 of a ring, as previously suggested by the PCA projection, although now the circular pattern was more
140 salient (Fig. 2d right). The progression of population activity along the manifold was tracked through a
141 parameter that we call the “phase of the oscillation” and that we calculate as the arctangent of the ratio
142 between the population activity modes given by PC2 and PC1 (Fig. 2e, red trace). During one full rotation
143 of the population activity along the ring-shaped manifold, which we refer to as one “cycle”, the phase
144 of the oscillation traversed $[-\pi, \pi)$ rad.

145 While striking population oscillations were observed across multiple sessions and animals, the
146 population activity exhibited considerable variability, ranging from non-patterned activity to highly
147 stereotypic and periodic sequences (Extended data Fig. 4a). This variability was also observed when
148 examining the joint distribution of time lags (τ) that maximized the correlation between cells’ calcium
149 activity and the angular distances d in the PCA sorting (Fig. 2f left). In sessions with clear population
150 oscillations, the time lag τ increased with the distance d , which indicated sequential activation of neural
151 activity. This dependence was observed a discrete number of times in each session, which indicated that
152 cells were active periodically and at a fixed frequency or at an integer multiple of it (Fig. 2f right, built
153 on the example session shown in Fig. 2a, and Extended data Fig. 4b top for another example with a
154 different time scale). In sessions without detectable population oscillations such structure was not
155 observed (Extended data Fig. 4b bottom). This variability in population dynamics prompted us to
156 quantify, for each session, the extent to which the population activity was oscillatory through an
157 oscillation score that ranged from 0 (no oscillation) to 1 (strong oscillations). The score was calculated
158 by first binning the angular distance between cells in the PCA sorting, using 11 bins, and then counting
159 the fraction of bins in which the cross correlations between the calcium activity of cell pairs peaked at
160 regular intervals (Online Methods). The distribution of oscillation scores over the entire MEC dataset (27
161 recording sessions in 5 mice) was bimodal (Extended data Fig. 4c), with 12/27 sessions exhibiting scores
162 between 0 and 0.2 (no oscillations), and 15/27 sessions scoring between 0.72 and 1. The latter sessions
163 were classified as oscillatory (15 oscillatory sessions over 5 mice; one of the mice did not have any
164 oscillatory sessions; Extended data Fig. 4a).

165 For each oscillatory session, we investigated how the population activity varied across individual cycles
166 and whether the length of individual cycles varied within and between sessions. We identified individual
167 cycles by extracting the subset of adjacent time bins where the phase of the oscillation increased
168 smoothly within the range $[-\pi, \pi)$ (bin size 129 ms, Extended data Fig. 5a,b). We divided each cycle into
169 10 segments, and for each segment we calculated the mean rate of calcium events over recorded
170 neurons (total number of events across cells divided by cycle segment duration and number of cells).
171 Across sessions we found that the percentage rate change from the segment with the minimum event
172 rate to the segment with the maximum rate was no more than 18% (Extended data Fig. 5c). There was
173 no significant difference in median event rate between pairs of segments within cycles (Extended data
174 Fig. 5c). Next we quantified, within and across sessions and animals, the variability in the length of
175 individual cycles, or the time for population activity to traverse the ring once (Extended data Fig. 5a).
176 Cycle lengths ranged from tens of seconds to minutes (Fig. 2g) and showed high variability across
177 sessions and animals (Fig. 2h, Extended data Fig. 5d) but there was little variability within individual
178 sessions (Extended data Fig. 5a,e). Cycle length was independent of the number of recorded cells
179 (Extended data Fig. 5f).

180 Finally, we quantified the duration of epochs with uninterrupted population oscillation. We calculated
181 the inter-cycle interval (ICI) for all cycles in one session as the amount of time that elapsed between the
182 moment the phase of the oscillation reaches π after completing one turn along the ring, and the moment

183 it is equal to $-\pi$ prior to initiating the next turn along the ring. ICIs were then pooled across sessions.
184 ICIs were present at different lengths, ranging from 0 s when cycles are consecutive (69% of ICIs, 279 of
185 406 ICIs) to a maximum of 452 s (Fig. 2i). The fraction of session time with population oscillation varied
186 within and across animals (Extended data Fig. 5g), yet - when present - the oscillation could progress
187 uninterrupted for minutes in each of the animals and span up to 23 consecutive cycles (Extended data
188 Fig. 5h).

189 Taken together, these results suggest that when animals are engaged in a self-paced locomotor task
190 under minimal sensory stimulation and in the absence of rewards, population activity in the superficial
191 layers of the MEC is organized into a minute-scale population oscillation consisting of periodic sequences
192 of neural activity.

193

194 ***The majority of MEC neurons are locked to the population oscillation***

195

196 To determine the degree to which calcium activity in individual MEC neurons was tuned to the
197 population oscillation, we computed for each neuron the locking of its calcium activity to the phase of
198 the oscillation. For each cell, the locking degree was calculated as the length of the mean vector obtained
199 from the distribution of oscillation phases at which calcium events occurred, with a range from 0
200 (uniform distribution of oscillation phases at which calcium events occur) to 1 (all calcium events occur
201 at the same oscillation phase). Significant locking degrees were observed for the vast majority of the
202 recorded cells (Fig. 3a left, calculated on data from the example session in Fig. 2a; 458 significantly
203 locked neurons over 484 total neurons recorded, or 95%). For these cells, the locking degree was higher
204 than the 99th percentile of a null distribution obtained by temporally shuffling the cell's calcium events.
205 The observed values of locking degree were consistent with another measure of locking that does not
206 make any assumptions about unimodal distribution of the data: the mutual information between the
207 counts of calcium events and the phase of the oscillation (Fig. 3a right, Extended data Fig. 6a, bin size
208 0.52 s). The predominance of phase-locked neurons was observed in all 15 oscillatory sessions (Fig. 3b,
209 5841 locked neurons out of 6231, ~94%).

210

211 The locking degree was highest for cells with an oscillatory frequency similar to the frequency of the
212 population oscillation, which constituted the large majority of the cells (Extended data Fig. 6b,c).
213 However, neurons with weak phase locking were still engaged in the population oscillation, since the
214 oscillatory sequences were maintained when neurons with high locking degree were excluded
215 (Extended data Fig. 6d). Yet, the more cells were excluded, the harder it was to observe the population
216 oscillation, indicating that the oscillatory dynamics is a property of neural populations (Extended data
217 Fig. 6d). Because the population oscillation involves the vast majority of MEC neurons in the recording
218 region (~95%), the sequences most likely include a mixture of functional cell types such as grid, head-
219 direction, and object-vector cells, given that (i) no cell type accounts for more than 15-25% of the cells
220 in layer II of dorsal MEC^{41,42}, and (ii) functional cell types in this area are spatially intermixed within field
221 of views of the microscope that are smaller than the one we used⁴².

222

223 Each locked neuron exhibited a preference for activity within a narrow range of phases of the oscillation
224 (Fig. 3c calculated on the example session in Fig. 2a, Extended data Fig. 6e). Across the entire recorded
225 population, all phases of the oscillation were equally present when the cells' preferred phase was
226 calculated as the mean oscillation phase at which the cell's calcium events occurred. A uniform
227 distribution was observed both within individual experimental sessions (Fig. 3c) and across all sessions
228 with oscillations (Extended data Fig. 6e,f).

229

230 Not all neurons participated in each individual oscillation cycle, however. We quantified the degree to
231 which cells skipped cycles through a participation index (PI), calculated as the fraction of cycles needed
232 to account for 90% of the total amount of calcium events of a neuron in one session. For neurons that
233 were active only in a few cycles the participation index was small (participation index ~ 0), and for

234 neurons that were reliably active during most of the cycles the participation index was high
235 (participation index ~ 1 , Extended data Fig. 6g shows three example neurons of the session in Fig. 2a).
236 Participation index variability was observed both within individual experimental sessions (Fig. 3d left),
237 and across all oscillatory sessions (Fig. 3d right). The participation index did not correlate with the degree
238 to which the single cell oscillatory frequency matched the population oscillation frequency (Extended
239 data Fig. 6h).

240

241 We next asked how differences between cells' preferred phase or participation mapped onto the MEC
242 surface (Extended data Fig. 1c), keeping in mind that the population oscillation in MEC could have
243 features of travelling waves, where the population activity moves progressively across anatomical
244 space⁴³⁻⁴⁸. We calculated pairwise anatomical distances in the microscope's field of view (i) between
245 cells with similar preferred phases and (ii) between cells with different preferred phases (Extended data
246 Fig. 6i). If topographical organization were present, we would expect smaller pairwise anatomical
247 distances for the cells with the most similar preferred phases. The results showed, however, that cells
248 with similar and dissimilar preferred phases were anatomically intermingled (Movie 1 and Fig. 3e,f).
249 Changing the fraction of cells used to define the groups with similar and different preferred phases had
250 no impact on the degree of intermixing (Extended data Fig. 6j). There was also no topography in the
251 neurons' participation indexes (Fig. 3g,h; Extended data Fig. 6k,l).

252

253 Taken together, these findings suggest that even though the majority of MEC neurons were locked to
254 the population oscillation, both their locking degree and the participation in individual cycles varied
255 across the population.

256

257 ***The population oscillation consists of periodic and unidirectional activity sequences***

258 We next sought to quantify the sequential activation and periodicity of neural activity during the
259 population oscillation. In order to average out the variability observed at the single cell level in terms of
260 oscillation frequency, locking degree and participation index (Fig. 1,3), we decided to study the neural
261 population dynamics by means of ensembles of co-active cells (Extended data Fig. 7a). As expected, the
262 participation index increased when activity was considered for merged groups of cells, or neuronal
263 ensembles, instead of single neurons (Extended data Fig. 7b). Because the participation index plateaued
264 after 5 merging iterations, consisting of approximately 10 ensembles depending on the session, we
265 chose to assign neurons to a total of 10 ensembles, based on their proximity in the sorting obtained
266 through the PCA method (Fig. 4a, note that each cell belongs to only one ensemble). Ensembles were
267 representative of the activity of their assigned neurons (Extended data Fig. 7c-f), their activity oscillated
268 at the same frequency as the population oscillation (Extended data Fig. 7g,h), and the ensembles were
269 anatomically intermingled (Extended data Fig. 7i-k).

270 To quantify the temporal dynamics of the ensemble activity, we calculated the probability by which
271 activity transitioned between ensembles across adjacent time bins, and expressed the resulting
272 probabilities as a transition matrix (Fig. 4b). For each time bin of the recording session (bin size shown
273 in Extended data Fig. 7l), we only kept the ensemble with the highest activity (red rectangle in Extended
274 data Fig. 7m; Extended data Fig. 7n). The analysis revealed (i) that transitions between adjacent
275 ensembles were more frequent than transitions between ensembles that were farther apart, and (ii)
276 that transitions occurred with a preferred directionality (Fig 4b, left). Transitions from ensemble 10 to
277 ensemble 1 were equally frequent as transitions between consecutive ensembles (Extended data Fig.
278 7o), as expected from the periodic nature of the population oscillation. No such structure was seen in
279 transition matrices obtained after shuffling the calcium activity of all cells (Fig 4b, right). The findings
280 were upheld when the transition matrix was used as an adjacency matrix to build a directed weighted
281 graph (Extended data Fig. 7p).

282 We then asked whether preferences in nearby ensemble transitions gave rise to stereotyped activity
283 sequences. We calculated the probability of sequential ensemble activation by counting the number of
284 times that, within one session, a given number of ensembles was activated in a strictly ascending
285 manner. The procedure was applied on both recorded and shuffled data (Fig 4c). In the oscillatory
286 sessions the sequential activation of three or more ensembles was 2.3 times more likely in the recorded
287 data than in the shuffled data (probability of sequential activation of ≥ 3 ensembles in recorded data =
288 0.62; probability of sequential activation of ≥ 3 ensembles in shuffled data = 0.27). These findings
289 motivated us to compute a sequence score, which quantifies how sequential the ensemble activity is
290 within a session. The sequence score was calculated as the probability of observing three or more
291 ensembles sequentially activated. As expected, the score was larger for sessions that were classified as
292 oscillatory according to the oscillation score (which quantifies the presence of single cell periodic
293 activity, Extended data Fig. 7q). Statistical significance was assessed by temporally shuffling the matrix
294 of calcium activity. While sequence scores were significant in 100% of the oscillatory sessions (15 of 15),
295 significant sequential activity was demonstrated also in 41% of the non-oscillatory sessions (5 of 12,
296 Extended data Fig. 7r). Taken together, our results suggest that the population oscillation is composed
297 of periodic, sequential and unidirectional activation of ensembles of highly-correlated neurons.

298

299 ***The population oscillation is present during both running and immobility***

300 Fast oscillations and single cell firing in the entorhinal-hippocampal system can be modulated by a
301 number of movement-associated parameters, such as running state, position, travel distance, running
302 speed and acceleration^{2,3,49,50}. These relationships prompted us to investigate whether similar
303 dependencies are present for population oscillations that occur at the seconds-to-minutes time scale
304 (Fig. 5a).

305 We first sought to determine whether the population oscillation is associated with specific behavioural
306 states such as running (animal moves along the rotating wheel) or immobility (position on the wheel
307 remains unchanged, regardless of body movement). The amount of running vs. immobility varied
308 substantially across sessions (the fraction of time spent running ranged from 0.04 to 0.87, median =
309 0.53, Extended data Fig. 2a). Analyses of the relationship between movement and population
310 oscillations were restricted to 10 oscillatory sessions in 3 animals, for which the behavioural tracking
311 was successfully synchronized to imaging (Online Methods). By following a two-step approach, we
312 estimated for these sessions the probability of observing the population oscillation given that the animal
313 was either running or immobile. First, for each session we identified the time bins that belonged to
314 individual cycles of the oscillation (Extended data Fig. 5a), and we labeled those bins as “oscillation bins”.
315 The fraction of bins labeled as oscillation bins was 0.73 ± 0.07 (mean \pm S.E.M., $n = 10$ sessions). Next, to
316 compute the conditional probabilities we assigned a second label to each bin depending on whether it
317 occurred during running or immobility (speed \geq or $<$ 2cm/s; fraction of bins labeled as running = $0.43 \pm$
318 0.09, mean \pm SEM, $n = 10$ sessions). We found that the population oscillation was predominant during
319 running bouts (Fig. 5b, left), but it was also observed during immobility (Fig. 5b, right), suggesting that
320 the oscillation is not exclusive to epochs in which the animal is engaged in locomotion. Population
321 oscillation cycles were continuous for immobility durations spanning from 1 s to more than 25 s (Fig. 5c,
322 Extended data Fig. 2b). The continued presence of the population oscillation during long epochs of
323 immobility suggests that behavioural state and running distance have a limited role in driving the
324 progression of the population oscillation in MEC, and stands in contrast to previous observations in CA1
325 of the hippocampus, where stereotypic sequences of neural activity subsided within 2 seconds after
326 motion was terminated³⁶.

327 We then asked whether the population oscillation is modulated by the animal’s position, running speed
328 or acceleration on the wheel, which all varied substantially during the course of a session. Across the 10

329 sessions, the range of speed values was 0-75.4 cm/s, with a median of 0 cm/s and a median during
330 running behaviour of 7.8 cm/s, whereas acceleration values ranged from -86.3 to 108.9 cm/s², with a
331 median of 0 cm/s² for all the data as well as the running epochs specifically. The number of laps the
332 animals completed on the wheel during one oscillation cycle was also highly heterogeneous, ranging
333 from 0 to 86 laps per cycle across all animals (lap length~54 cm; Fig. 5d, Extended data Fig. 2c),
334 suggesting that the progression of oscillatory activity did not map the animal's position on the wheel.
335 To determine the impact of running speed on the population oscillation, we extracted all oscillation bins
336 and calculated the distribution of observed speed values during those bins. This distribution was almost
337 identical to the distribution of speed values observed during the full length of the sessions, which also
338 included epochs without the population oscillation (Fig. 5e, 314 cycles pooled across 10 oscillatory
339 sessions). Oscillation cycles took place during a wide range of speed values, spanning from 0 to more
340 than 50 cm/s (Fig. 5e). Oscillation bins were similarly independent of acceleration (Fig. 5f).

341 Finally, since the population oscillation was observed more often during running bouts (Fig. 5b), we
342 investigated whether changes in speed were associated with the initiation of oscillation cycles. We
343 found no difference in speed 10 s before and after cycle onset (Extended data Fig. 2d, left; see Extended
344 data Fig. 2e-h for individual recordings). This result also held for cycles that were 10 s or more apart, i.e.
345 for cycles that belonged to different epochs with uninterrupted population oscillation (Extended data
346 Fig. 2d, right). Altogether, our results show that the MEC population oscillation is not modulated by the
347 animal's position on the wheel and is only mildly modulated by the animal's running behavior, consistent
348 with the idea that the entorhinal network can generate such oscillations using intrinsic mechanisms.

349

350 ***Population oscillations were not observed in other brain regions***

351 The fact that ultraslow oscillations have been reported in widely different brain areas²¹⁻²⁹ prompted us
352 to investigate whether a population oscillation composed of oscillatory sequences of neural activity of
353 the kind we found in the MEC could be observed in other regions too. We recorded the activity of
354 hundreds of cells in the superficial layers of the parasubiculum (PaS), a high-end parahippocampal region
355 abundant with grid, head-direction and border cells but with a different circuit structure and a weaker
356 theta rhythmicity than MEC^{42,51} (25 sessions over 4 animals, Extended data Fig. 8a,b). In addition, we
357 investigated the superficial layers of visual cortex⁵² (VIS, 19 sessions over 3 animals, Extended data Fig.
358 8c), which differs from MEC^{53,54} in its network architecture and in the high dimensionality of its neural
359 population activity. The mice performed the same minimalistic self-paced running task as in the MEC
360 recordings (range of speed values in PaS/VIS animals across sessions=0-58.6/0-60.3 cm/s; median
361 number of completed laps on rotating wheel in PaS/VIS animals across sessions=145/104; maximum
362 number of completed laps on rotating wheel in PaS/VIS animals across sessions=502/1743).

363 To determine whether single-cell calcium activity in PaS and VIS was periodic and oscillated at ultraslow
364 frequencies we followed the same procedure as for the MEC sessions. We found that the calcium activity
365 of a fraction of cells in both brain areas was indeed periodic (Fig. 6a,b). However, in neither brain region
366 were these oscillations organized into sequences of neural activity. The population oscillation was
367 observed neither with the PCA method nor with pairwise correlations or any of the non-linear
368 dimensionality reduction techniques that we had used (Fig. 6c-f; Extended data Fig. 9a). When projected
369 onto a linear low-dimensional embedding, the population activity did not display a ring-shaped topology
370 (Extended data Fig. 9b,c). For all sessions in PaS and VIS, the oscillation scores were lower than the
371 threshold defined from the MEC data to classify sessions as oscillatory (Extended data Fig. 9d; threshold
372 = 0.72, see Extended data Fig. 4c), suggesting that a population oscillation was weak or absent (Fig. 6g).
373 Taken together, these results suggest that MEC has network mechanisms for sequential coordination of
374 single-cell oscillations that are not present in PaS or VIS.

375 While ensemble analyses showed no preference for transitions between co-active cells that were nearby
376 in the PCA sorting (Fig 6h; Extended data Fig. 10a-d), the probability of sequential activation in PaS was
377 significantly larger in experimental data than in shuffled data (Fig. 6i left, $n = 25$ sessions). No significant
378 difference was found in VIS (Fig. 6i right, $n = 19$ sessions). In line with this result, the percentage of
379 sessions with significant sequence scores (defined as the probability of observing the sequential
380 activation of 3 or more ensembles) was highest for oscillatory sessions in MEC (15 out of 15, 100%),
381 intermediate for PaS (7 out of 25, 28%) and lowest for VIS (1 out of 19, 0.05%) (Extended data Fig. 10e).
382 Features of the animal's behaviour were not different between sessions with significant and non-
383 significant sequence scores (Extended data Fig. 10f-i; all regions).

384 Finally, the presence of sequential ensemble activation in many PaS recordings, but not in VIS, motivated
385 us to investigate whether this difference could reflect a stronger tendency for VIS neurons to cluster
386 into a few synchronized states. We quantified synchronization through the absolute value of the
387 correlation between the calcium activity of all cell pairs, as well as co-activity, calculated as the fraction
388 of cells that had simultaneous calcium events in bins of 129 ms. Data from VIS had both higher
389 correlation values (Extended data Fig. 10j) and higher co-activity (Extended data Fig. 10k), compared to
390 PaS. The strong synchronization of calcium activity in VIS is consistent with previous observations of
391 recurring co-activity among subsets of neurons (ensembles) in this brain region^{37,55}.

392

393 Discussion

394 Our experiments identify an ultraslow neural population oscillation that organizes neural activity in the
395 majority of neurons recorded in the MEC of awake head-fixed mice during self-paced running as well as
396 intermittent segments of rest. Across recording sessions, the length of individual oscillation cycles can
397 range from tens of seconds to minutes, but the time scale is generally fixed within an individual recording
398 session. This oscillation is expressed as unidirectional sequences of activity that can repeat
399 uninterrupted for tens of minutes. The oscillation entrains periodic activity in individual neurons despite
400 some variability in the frequency of single cell activity. Individual cells are activated at specific phases of
401 the population oscillation, with phase preferences distributed uniformly across the population. Unlike
402 faster oscillations, which typically have the greater part of the neural activity centered within a narrow
403 segment of the oscillation cycle⁵⁶⁻⁵⁸, the population oscillation in MEC maintains a relatively constant
404 activity rate throughout the cycle, reflecting the steady progression of a sequence of neural activity.

405

406 Oscillations at time scales of tens of seconds to minutes have been reported in individual cells of multiple
407 brain areas and in a variety of brain states including anaesthesia, sleep and alert immobility²¹⁻²⁶. EEG and
408 fMRI recordings from awake humans⁵⁹⁻⁶², as well as LFP from anaesthetized and awake animals²⁷⁻²⁹ have
409 similarly demonstrated oscillatory changes at periods of 10 s or longer. However, we do not know from
410 those observations how the activity of individual neurons is organized with respect to each other during
411 the oscillation. The present data demonstrate an ultraslow population oscillation at a time scale ranging
412 from tens of seconds to minutes that, in a controlled behavioral setting and under minimal sensory
413 stimulation, engages sequentially the vast majority of neurons in the recorded area of MEC. The
414 population oscillation is only mildly modulated by the animal's running behavior and is therefore more
415 likely to emerge from intrinsic network mechanisms.

416

417 The ultraslow oscillatory sequences of the MEC stand out from instances of slow sequential neural activity
418 that have not been described in terms of oscillations. In the hippocampus, neural activity in CA1 cells is
419 organized into stereotypic sequences when rats or mice run on a rotating wheel in a cue-rich
420 environment⁶³ or in a sensory-restricted environment similar to the one used here^{36,64}. Unlike what we
421 observed in MEC, these sequences are more strictly coupled to ongoing behavioral activity and running

422 distance³⁶, and they have not been found to exhibit temporal periodic organization at a well-defined
423 frequency. Moreover, while nearly 95% of all MEC neurons in the present study were locked to the
424 population oscillation and most of them participated in at least half of the cycles, hippocampal sequences
425 involve only a small fraction of the network (5% in ref. 36). Such a difference in participation would be in
426 agreement with the view that the MEC supports a low-dimensional population code where the cells'
427 responses covary across environments and behavioural states^{53,54,65}, whereas the hippocampus supports
428 a more high-dimensional population code that may orthogonalize distinct experiences⁶⁶⁻⁶⁹. The MEC
429 population oscillation also differs from retinal waves and cortical waves in the developing nervous
430 system⁴³⁻⁴⁸, as well as travelling waves in the adult hippocampus^{70,71}, which all move progressively through
431 anatomical space, in a topographic manner not observed in the present data.

432

433 The presence of oscillatory activity in individual cells of all three regions – visual cortex, parasubiculum
434 and MEC – together with the absence of population oscillation in the former two, points to MEC as having
435 network mechanisms for sequential coordination of single cell oscillations that are not present in
436 parasubiculum or visual cortex. Such mechanisms might share similarities with prewired sequences in the
437 hippocampus⁷², or they may be supported by plasticity rules operating on slow time scales⁷³. The
438 population oscillation of the MEC is consistent with dynamics expected in a one-dimensional continuous
439 attractor network⁷⁴⁻⁷⁶ where cells are conceptualized as lying on a functional ring with positions
440 determined by the cells' loadings on the first two principal components. However, it has not been
441 determined whether such ring-like connectivity exists among the high percentage of MEC neurons
442 entrained by the population oscillation, and, if there is such connectivity, which signal is responsible for
443 moving the bump of activity along the ring. Sequential activity could also be generated by other types of
444 structured connectivity, for example in recurrently connected networks^{77,78} and in feedforward networks
445 in which sequences may arise through synfire chains or rate propagation⁷⁹⁻⁸³. But while structured
446 connectivity might allow for slow transitions in the ensemble activity^{84,85}, none of the mechanisms
447 proposed so far generate minute-scale repeating sequences with the variability at the single-cell level that
448 we here observed in the MEC population oscillation.

449 We propose two related functions for the MEC population oscillation. First, the reported oscillations might
450 have a role in large-scale coordination of entorhinal circuit elements^{7,10,86,87}, either by synchronizing faster
451 oscillatory activity^{25,29,60-62}, such as theta and gamma^{11,12,32}, or by organizing neural activity across
452 functionally dissociable cell classes, such as grid cells, head direction cells, border cells, and object-vector
453 cells^{2-6,88}. Given that each of these functional cell classes accounts for less than 15-25% of the local cell
454 population in dorsal MEC^{41,42}, whereas nearly all recorded neurons in the present study were locked to
455 and participated in the population oscillation, the population oscillation is likely to consist of a mixture of
456 functional cell types. Coordination by the population oscillation may prevent functional cell classes from
457 drifting apart and help the circuit maintain correlated firing over the entire duration of an experience^{89,90}.
458 Second, the MEC oscillatory sequences may act as a scaffold to support computations that must take place
459 on the fly with little time for extensive circuit plasticity, such as fast storage of memories associated with
460 one-time experiences^{69,91}, or the assembly of representations for complex sensory stimuli that evolve over
461 time^{37,92}. The ultraslow population oscillation may also enable the circuit to keep track of time during
462 extended behavioral experiences⁹³. The temporally organized firing of time cells in MEC^{94,95} and the more
463 extended temporal evolution of neural population activity in LEC⁹⁶ may be facilitated by an underlying
464 sequence template. Whether the population oscillations serve such coordination and scaffolding
465 functions across a broader spectrum of behaviors than in the minimalistic task used here remains to be
466 determined. If similarly slow periodic sequences are expressed across a wider span of behaviors, including
467 sleep and free exploration, they must interface with dynamics of MEC cells on a number of manifolds,
468 such as in ensembles of head direction cells and grid cells^{54,97,98}.

469

470

471 **Acknowledgments.** We thank W. Zong, C. Battistin, I. Davidovich, Y. Roudi and E. Kropff for discussion,
472 Y. Burak for discussion and comments on the manuscript, D.W. Tank for sharing hardware, software and
473 advice during the earliest stages of the study, and A. Tsao, G.B. Keller and T. Bonhoeffer for help in
474 setting up initial procedures for benchtop 2-photon imaging for mice running on a rotating wheel. We
475 thank A.M. Amundsgård, K. Haugen, K. Jenssen, E. Kråkvik, I. Ulsaker-Janke, and H. Waade for technical
476 assistance. The work was supported by a Synergy Grant to E.I.M. and Yoram Burak from the European
477 Research Council ('KILONEURONS', Grant Agreement N° 951319), an RCN FRIPRO grant to E.I.M. (grant
478 number 286225), a Centre of Excellence scheme grant to M.-B.M. and E.I.M. and a National
479 Infrastructure grant to E.I.M. and M.-B.M. from the Research Council of Norway (Centre of Neural
480 Computation, grant number 223262; NORBRAIN, grant number 295721), the Kavli Foundation (M.-B.M.
481 and E.I.M.), a direct contribution to M.-B.M. and E.I.M. from the Ministry of Education and Research of
482 Norway, and a European Research Council Starting Grant (ERC-ST2019 850769) and an Eccellenza Grant
483 from the Swiss National Science Foundation (PCEGP3_194220) to F.D.

484 **Author Contributions:** F.D., H.O., M.-B.M. and E.I.M. planned and designed the initial experiments, with
485 later input from S.G.C.; F.D. and R.I.J. performed the experiments; H.O. developed hardware and imaging
486 software, preprocessed the data and performed initial analysis; S.G.C., M.-B.M. and E.I.M.
487 conceptualized and proposed analyses, with input from F.D.; S.G.C. performed analyses of neural
488 activity; F.D. performed histological analyses; S.G.C., F.D., M.-B.M. and E.I.M. interpreted data; S.G.C.
489 and F.D. visualized data; S.G.C. and E.I.M. wrote the paper, with initial contributions from F.D. and with
490 periodic input from all authors; M.-B.M. and E.I.M. supervised and funded the project.

491

492 **Supplementary Information** is available for this paper.

493

494 Author Contact Information. Correspondence should be addressed to S.G.C., F.D., M.-B.M. or E.I.M.
495 Requests for materials should be directed to E.I.M. (edvard.moser@ntnu.no).

496

497 **Reprints and Permissions** information is available at www.nature.com/reprints

498

499 **Competing interests statement**

500 The authors declare that they have no competing financial interests.

501

502 **Keywords**

503 Ultraslow oscillations, rhythms, neuronal activity sequences, entorhinal cortex, navigation, episodic
504 memory, neural coordination.

505

506

507

508

509

510

511

512 **References**

- 513 1. Buzsáki, G., & Moser, E. I. (2013). Memory, navigation and theta rhythm in the hippocampal-
514 entorhinal system. *Nature Neuroscience*, *16*(2), 130-138.
- 515 2. Hafting, T., Fyhn, M., Molden, S., Moser, M. B., & Moser, E. I. (2005). Microstructure of a spatial map
516 in the entorhinal cortex. *Nature*, *436*(7052), 801-806.
- 517 3. Sargolini, F., Fyhn, M., Hafting, T., McNaughton, B. L., Witter, M. P., Moser, M. B., & Moser, E. I.
518 (2006). Conjunctive representation of position, direction, and velocity in entorhinal
519 cortex. *Science*, *312*(5774), 758-762.
- 520 4. Savelli, F., Yoganarasimha, D., & Knierim, J. J. (2008). Influence of boundary removal on the spatial
521 representations of the medial entorhinal cortex. *Hippocampus*, *18*(12), 1270-1282.
- 522 5. Solstad, T., Boccara, C. N., Kropff, E., Moser, M. B., & Moser, E. I. (2008). Representation of
523 geometric borders in the entorhinal cortex. *Science*, *322*(5909), 1865-1868.
- 524 6. Høydal, Ø. A., Skytøen, E. R., Andersson, S. O., Moser, M. B., & Moser, E. I. (2019). Object-vector
525 coding in the medial entorhinal cortex. *Nature*, *568*(7752), 400-404.
- 526 7. Singer, W. (1993). Synchronization of cortical activity and its putative role in information processing
527 and learning. *Annual Review of Physiology*, *55*(1), 349-374.
- 528 8. Laurent, G. (1996). Dynamical representation of odors by oscillating and evolving neural
529 assemblies. *Trends in Neurosciences*, *19*(11), 489-496.
- 530 9. Buzsáki, G. (2006). *Rhythms of the Brain*. Oxford University Press.
- 531 10. von der Malsburg, C. E., Phillips, W. A., & Singer, W. E. (2010). *Dynamic Coordination in the Brain:*
532 *From Neurons to Mind*. MIT Press.
- 533 11. Mitchell, S. J., & Ranck Jr, J. B. (1980). Generation of theta rhythm in medial entorhinal cortex of
534 freely moving rats. *Brain Research*, *189*(1), 49-66.
- 535 12. Chrobak, J. J., & Buzsáki, G. (1998). Gamma oscillations in the entorhinal cortex of the freely
536 behaving rat. *Journal of Neuroscience*, *18*(1), 388-398.
- 537 13. Colgin, L. L. (2016). Rhythms of the hippocampal network. *Nature Reviews Neuroscience*, *17*(4),
538 239-249.
- 539 14. Rabinovich, M., Huerta, R., & Laurent, G. (2008). Transient dynamics for neural
540 processing. *Science*, *321*(5885), 48-50.
- 541 15. Vyas, S., Golub, M. D., Sussillo, D., & Shenoy, K. V. (2020). Computation through neural population
542 dynamics. *Annual Review of Neuroscience*, *43*, 249-275.
- 543 16. György Buzsáki, M. D. (2019). *The Brain from Inside Out*. Oxford University Press.
- 544 17. Petsche, H., Stumpf, C., & Gogolak, G. (1962). The significance of the rabbit's septum as a relay
545 station between the midbrain and the hippocampus I. The control of hippocampus arousal activity by
546 the septum cells. *Electroencephalography and Clinical Neurophysiology*, *14*(2), 202-211.
- 547 18. Gray, C. M., König, P., Engel, A. K., & Singer, W. (1989). Oscillatory responses in cat visual cortex
548 exhibit inter-columnar synchronization which reflects global stimulus properties. *Nature*, *338*(6213),
549 334-337.

- 550 19. Laurent, G., Wehr, M., & Davidowitz, H. (1996). Temporal representations of odors in an olfactory
551 network. *Journal of Neuroscience*, 16(12), 3837-3847.
- 552 20. Harris, K. D., Csicsvari, J., Hirase, H., Dragoi, G., & Buzsáki, G. (2003). Organization of cell assemblies
553 in the hippocampus. *Nature*, 424(6948), 552-556.
- 554 21. Albrecht, D., Royl, G., & Kaneoke, Y. (1998). Very slow oscillatory activities in lateral geniculate
555 neurons of freely moving and anesthetized rats. *Neuroscience Research*, 32(3), 209-220.
- 556 22. Penttonen, M., Nurminen, N., Miettinen, R., Sirviö, J., Henze, D. A., Csicsvári, J., & Buzsáki, G.
557 (1999). Ultra-slow oscillation (0.025 Hz) triggers hippocampal afterdischarges in Wistar
558 rats. *Neuroscience*, 94(3), 735-743.
- 559 23. Ruskin, D. N., Bergstrom, D. A., Kaneoke, Y., Patel, B. N., Twery, M. J., & Walters, J. R. (1999).
560 Multisecond oscillations in firing rate in the basal ganglia: robust modulation by dopamine receptor
561 activation and anesthesia. *Journal of Neurophysiology*, 81(5), 2046-2055.
- 562 24. Allers, K. A., Kreiss, D. S., & Walters, J. R. (2000). Multisecond oscillations in the subthalamic
563 nucleus: effects of apomorphine and dopamine cell lesion. *Synapse*, 38(1), 38-50.
- 564 25. Allers, K. A., Ruskin, D. N., Bergstrom, D. A., Freeman, L. E., Ghazi, L. J., Tierney, P. L., & Walters, J.
565 R. (2002). Multisecond periodicities in basal ganglia firing rates correlate with theta bursts in
566 transcortical and hippocampal EEG. *Journal of Neurophysiology*, 87(2), 1118-1122.
- 567 26. Wichmann, T., Kliem, M. A., & Soares, J. (2002). Slow oscillatory discharge in the primate basal
568 ganglia. *Journal of Neurophysiology*, 87(2), 1145-1148.
- 569 27. Aladjalova, N. A. (1957). Infra-slow rhythmic oscillations of the steady potential of the cerebral
570 cortex. *Nature*, 179(4567), 957-959.
- 571 28. Leopold, D. A., Murayama, Y., & Logothetis, N. K. (2003). Very slow activity fluctuations in monkey
572 visual cortex: implications for functional brain imaging. *Cerebral Cortex*, 13(4), 422-433.
- 573 29. Lecci, S., Fernandez, L. M., Weber, F. D., Cardis, R., Chatton, J. Y., Born, J., & Lüthi, A. (2017).
574 Coordinated infraslow neural and cardiac oscillations mark fragility and offline periods in mammalian
575 sleep. *Science Advances*, 3(2), e1602026.
- 576 30. Squire, L. R., Stark, C. E., & Clark, R. E. (2004). The medial temporal lobe. *Annual Review of*
577 *Neuroscience*, 27, 279-306.
- 578 31. Hasselmo, M. E. (2011). *How we remember: Brain Mechanisms of Episodic Memory*. MIT press.
- 579 32. Alonso, A., & Garcia-Austt, E. (1987). Neuronal sources of theta rhythm in the entorhinal cortex of
580 the rat. *Experimental Brain Research*, 67(3), 493-501.
- 581 33. Dombeck, D. A., Khabbaz, A. N., Collman, F., Adelman, T. L., & Tank, D. W. (2007). Imaging large-
582 scale neural activity with cellular resolution in awake, mobile mice. *Neuron*, 56(1), 43-57.
- 583 34. Heys, J. G., Rangarajan, K. V., & Dombeck, D. A. (2014). The functional micro-organization of grid
584 cells revealed by cellular-resolution imaging. *Neuron*, 84(5), 1079-1090.
- 585 35. Gu Y, Lewallen S, Kinkhabwala AA, Domnisoru C, Yoon K, Gauthier JL, Fiete IR, Tank DW (2018). A
586 map-like micro-organization of grid cells in the medial entorhinal cortex. *Cell*, 175(3), 736-750.

- 587 36. Villette, V., Malvache, A., Tressard, T., Dupuy, N., & Cossart, R. (2015). Internally recurring
588 hippocampal sequences as a population template of spatiotemporal information. *Neuron*, *88*(2), 357-
589 366.
- 590 37. Carrillo-Reid, L., Miller, J. E. K., Hamm, J. P., Jackson, J., & Yuste, R. (2015). Endogenous sequential
591 cortical activity evoked by visual stimuli. *Journal of Neuroscience*, *35*(23), 8813-8828.
- 592 38. Friedrich, J., Zhou, P., & Paninski, L. (2017). Fast online deconvolution of calcium imaging
593 data. *PLoS Computational Biology*, *13*(3), e1005423.
- 594 39. Pachitariu, M., Stringer, C., Dipoppa, M., Schröder, S., Rossi, L. F., Dalglish, H., ... & Harris, K. D.
595 (2017). Suite2p: beyond 10,000 neurons with standard two-photon microscopy. *BioRxiv*
596 doi: <https://doi.org/10.1101/061507>.
- 597 40. Cunningham, J. P., & Byron, M. Y. (2014). Dimensionality reduction for large-scale neural
598 recordings. *Nature Neuroscience*, *17*(11), 1500-1509.
- 599 41. Rowland, D. C., Obenhaus, H. A., Skytøen, E. R., Zhang, Q., Kentros, C. G., Moser, E. I., & Moser, M.
600 B. (2018). Functional properties of stellate cells in medial entorhinal cortex layer II. *Elife*, *7*, e36664.
- 601 42. Obenhaus, H. A., Zong, W., Jacobsen, R. I., Rose, T., Donato, F., Chen, L., ... & Moser, E. I. (2022).
602 Functional network topography of the medial entorhinal cortex. *Proceedings of the National Academy*
603 *of Sciences*, *119*(7), e2121655119.
- 604 43. Meister, M., Wong, R. O., Baylor, D. A., & Shatz, C. J. (1991). Synchronous bursts of action
605 potentials in ganglion cells of the developing mammalian retina. *Science*, *252*(5008), 939-943.
- 606 44. Wong, R. O., Meister, M., & Shatz, C. J. (1993). Transient period of correlated bursting activity
607 during development of the mammalian retina. *Neuron*, *11*(5), 923-938.
- 608 45. Garaschuk, O., Linn, J., Eilers, J., & Konnerth, A. (2000). Large-scale oscillatory calcium waves in the
609 immature cortex. *Nature Neuroscience*, *3*(5), 452-459.
- 610 46. Adelsberger, H., Garaschuk, O., & Konnerth, A. (2005). Cortical calcium waves in resting newborn
611 mice. *Nature Neuroscience*, *8*(8), 988-990.
- 612 47. Ackman, J. B., Burbridge, T. J., & Crair, M. C. (2012). Retinal waves coordinate patterned activity
613 throughout the developing visual system. *Nature*, *490*(7419), 219-225.
- 614 48. Muller, L., Chavane, F., Reynolds, J., & Sejnowski, T. J. (2018). Cortical travelling waves:
615 mechanisms and computational principles. *Nature Reviews Neuroscience*, *19*(5), 255-268.
- 616 49. Ahmed, O. J., & Mehta, M. R. (2012). Running speed alters the frequency of hippocampal gamma
617 oscillations. *Journal of Neuroscience*, *32*(21), 7373-7383.
- 618 50. Kropff, E., Carmichael, J. E., Moser, E. I., & Moser, M. B. (2021). Frequency of theta rhythm is
619 controlled by acceleration, but not speed, in running rats. *Neuron*, *109*(6), 1029-1039.
- 620 51. Boccara, C. N., Sargolini, F., Thoresen, V. H., Solstad, T., Witter, M. P., Moser, E. I., & Moser, M. B.
621 (2010). Grid cells in pre-and parasubiculum. *Nature Neuroscience*, *13*(8), 987-994.
- 622 52. Stringer, C., Pachitariu, M., Steinmetz, N., Carandini, M., & Harris, K. D. (2019). High-dimensional
623 geometry of population responses in visual cortex. *Nature*, *571*(7765), 361-365.
- 624 53. Yoon, K., Buice, M. A., Barry, C., Hayman, R., Burgess, N., & Fiete, I. R. (2013). Specific evidence of
625 low-dimensional continuous attractor dynamics in grid cells. *Nature Neuroscience*, *16*(8), 1077-1084.

- 626 54. Gardner, R. J., Hermansen, E., Pachitariu, M., Burak, Y., Baas, N. A., Dunn, B. A., Moser, M.-B. &
627 Moser, E. I. (2022). Toroidal topology of population activity in grid cells. *Nature*, 602(7895), 123-128.
- 628 55. Miller, J. E. K., Ayzenshtat, I., Carrillo-Reid, L., & Yuste, R. (2014). Visual stimuli recruit intrinsically
629 generated cortical ensembles. *Proceedings of the National Academy of Sciences*, 111(38), E4053-
630 E4061.
- 631 56. Buzsáki, G., & Vanderwolf, C. H. (1983). Cellular bases of hippocampal EEG in the behaving
632 rat. *Brain Research Reviews*, 6(2), 139-171.
- 633 57. Csicsvari, J., Hirase, H., Czurkó, A., Mamiya, A., & Buzsáki, G. (1999). Oscillatory coupling of
634 hippocampal pyramidal cells and interneurons in the behaving rat. *Journal of Neuroscience*, 19(1), 274-
635 287.
- 636 58. Csicsvari, J., Jamieson, B., Wise, K. D., & Buzsáki, G. (2003). Mechanisms of gamma oscillations in
637 the hippocampus of the behaving rat. *Neuron*, 37(2), 311-322.
- 638 59. Novak, P., Lepicovska, V., & Dostalek, C. (1992). Periodic amplitude modulation of
639 EEG. *Neuroscience Letters*, 136(2), 213-215.
- 640 60. Vanhatalo, S., Palva, J. M., Holmes, M. D., Miller, J. W., Voipio, J., & Kaila, K. (2004). Infralow
641 oscillations modulate excitability and interictal epileptic activity in the human cortex during
642 sleep. *Proceedings of the National Academy of Sciences*, 101(14), 5053-5057.
- 643 61. Nir, Y., Mukamel, R., Dinstein, I., Privman, E., Harel, M., Fisch, L., ... & Malach, R. (2008).
644 Interhemispheric correlations of slow spontaneous neuronal fluctuations revealed in human sensory
645 cortex. *Nature Neuroscience*, 11(9), 1100-1108.
- 646 62. Watson, B. O. (2018). Cognitive and physiologic impacts of the infralow oscillation. *Frontiers in*
647 *Systems Neuroscience*, 44.
- 648 63. Pastalkova, E., Itskov, V., Amarasingham, A., & Buzsaki, G. (2008). Internally generated cell
649 assembly sequences in the rat hippocampus. *Science*, 321(5894), 1322-1327.
- 650 64. Malvache, A., Reichinnek, S., Villette, V., Haimerl, C., & Cossart, R. (2016). Awake hippocampal
651 reactivations project onto orthogonal neuronal assemblies. *Science*, 353(6305), 1280-1283.
- 652 65. Fyhn, M., Hafting, T., Treves, A., Moser, M. B., & Moser, E. I. (2007). Hippocampal remapping and
653 grid realignment in entorhinal cortex. *Nature*, 446(7132), 190-194.
- 654 66. McNaughton, B. L., & Morris, R. G. (1987). Hippocampal synaptic enhancement and information
655 storage within a distributed memory system. *Trends in Neurosciences*, 10(10), 408-415.
- 656 67. Leutgeb, S., Leutgeb, J. K., Treves, A., Moser, M. B., & Moser, E. I. (2004). Distinct ensemble codes
657 in hippocampal areas CA3 and CA1. *Science*, 305(5688), 1295-1298.
- 658 68. Alme, C. B., Miao, C., Jezek, K., Treves, A., Moser, E. I., & Moser, M. B. (2014). Place cells in the
659 hippocampus: eleven maps for eleven rooms. *Proceedings of the National Academy of*
660 *Sciences*, 111(52), 18428-18435.
- 661 69. Buzsáki, G., & Tingley, D. (2018). Space and time: the hippocampus as a sequence
662 generator. *Trends in Cognitive Sciences*, 22(10), 853-869.
- 663 70. Lubenov, E. V., & Siapas, A. G. (2009). Hippocampal theta oscillations are travelling
664 waves. *Nature*, 459(7246), 534-539.

- 665 71. Patel, J., Fujisawa, S., Berényi, A., Royer, S., & Buzsáki, G. (2012). Traveling theta waves along the
666 entire septotemporal axis of the hippocampus. *Neuron*, 75(3), 410-417.
- 667 72. Dragoi, G., & Tonegawa, S. (2011). Preplay of future place cell sequences by hippocampal cellular
668 assemblies. *Nature*, 469(7330), 397-401.
- 669 73. Bittner, K. C., Milstein, A. D., Grienberger, C., Romani, S., & Magee, J. C. (2017). Behavioral time
670 scale synaptic plasticity underlies CA1 place fields. *Science*, 357(6355), 1033-1036.
- 671 74. Ben-Yishai, R., Bar-Or, R. L., & Sompolinsky, H. (1995). Theory of orientation tuning in visual
672 cortex. *Proceedings of the National Academy of Sciences*, 92(9), 3844-3848.
- 673 75. Skaggs, W. E., Knierim, J. J., Kudrimoti, H. S. & McNaughton, B. L. A model of the neural basis of the
674 rat's sense of direction. *Adv. Neural Inf. Process. Syst.* 7, 173–180 (1995).
- 675 76. Zhang, K. (1996). Representation of spatial orientation by the intrinsic dynamics of the head-
676 direction cell ensemble: a theory. *Journal of Neuroscience*, 16(6), 2112-2126.
- 677 77. Fiete, I. R., Senn, W., Wang, C. Z., & Hahnloser, R. H. (2010). Spike-time-dependent plasticity and
678 heterosynaptic competition organize networks to produce long scale-free sequences of neural
679 activity. *Neuron*, 65(4), 563-576.
- 680 78. Rajan, K., Harvey, C. D., & Tank, D. W. (2016). Recurrent network models of sequence generation
681 and memory. *Neuron*, 90(1), 128-142.
- 682 79. Hebb DO (1949) The organization of behaviour. New York: Wiley.
- 683 80. Abeles, M. (1991). *Corticonics: Neural Circuits of the Cerebral Cortex*. Cambridge University Press.
- 684 81. Diesmann, M., Gewaltig, M. O., & Aertsen, A. (1999). Stable propagation of synchronous spiking in
685 cortical neural networks. *Nature*, 402(6761), 529-533.
- 686 82. Kumar, A., Rotter, S., & Aertsen, A. (2008). Conditions for propagating synchronous spiking and
687 asynchronous firing rates in a cortical network model. *Journal of Neuroscience*, 28(20), 5268-5280.
- 688 83. Kumar, A., Rotter, S., & Aertsen, A. (2010). Spiking activity propagation in neuronal networks:
689 reconciling different perspectives on neural coding. *Nature Reviews Neuroscience*, 11(9), 615-627.
- 690 84. Litwin-Kumar, A., & Doiron, B. (2012). Slow dynamics and high variability in balanced cortical
691 networks with clustered connections. *Nature Neuroscience*, 15(11), 1498-1505.
- 692 85. Schaub, M. T., Billeh, Y. N., Anastassiou, C. A., Koch, C., & Barahona, M. (2015). Emergence of slow-
693 switching assemblies in structured neuronal networks. *PLoS Computational Biology*, 11(7), e1004196.
- 694 86. Steriade, M. (1997). Synchronized activities of coupled oscillators in the cerebral cortex and
695 thalamus at different levels of vigilance. *Cerebral Cortex* 7(6), 583-604.
- 696 87. Buzsáki, G. (2002). Theta oscillations in the hippocampus. *Neuron*, 33(3), 325-340.
- 697 88. Taube, J. S., Muller, R. U., & Ranck, J. B. (1990). Head-direction cells recorded from the
698 postsubiculum in freely moving rats. I. Description and quantitative analysis. *Journal of*
699 *Neuroscience*, 10(2), 420-435.
- 700 89. Mosheiff, N., & Burak, Y. (2019). Velocity coupling of grid cell modules enables stable embedding
701 of a low dimensional variable in a high dimensional neural attractor. *Elife*, 8, e48494.

- 702 90. Waaga, T., Agmon, H., Normand, V. A., Nagelhus, A., Gardner, R. J., Moser, M. B., ... & Burak, Y.
703 (2022). Grid-cell modules remain coordinated when neural activity is dissociated from external sensory
704 cues. *Neuron*, 50896-6273(22)00247-1. doi: 10.1016/j.neuron.2022.03.011. Epub ahead of print. PMID:
705 35385698.
- 706 91. Nicola, W., & Clopath, C. (2019). A diversity of interneurons and Hebbian plasticity facilitate rapid
707 compressible learning in the hippocampus. *Nature Neuroscience*, 22(7), 1168-1181.
- 708 92. Luczak, A., Bartho, P., & Harris, K. D. (2013). Gating of sensory input by spontaneous cortical
709 activity. *Journal of Neuroscience*, 33(4), 1684-1695.
- 710 93. Zhou, S., Masmanidis, S. C., & Buonomano, D. V. (2020). Neural sequences as an optimal dynamical
711 regime for the readout of time. *Neuron*, 108(4), 651-658.
- 712 94. Kraus, B. J., Brandon, M. P., Robinson II, R. J., Connerney, M. A., Hasselmo, M. E., & Eichenbaum, H.
713 (2015). During running in place, grid cells integrate elapsed time and distance run. *Neuron*, 88(3), 578-
714 589.
- 715 95. Heys, J. G., & Dombeck, D. A. (2018). Evidence for a subcircuit in medial entorhinal cortex
716 representing elapsed time during immobility. *Nature Neuroscience*, 21(11), 1574-1582.
- 717 96. Tsao, A., Sugar, J., Lu, L., Wang, C., Knierim, J. J., Moser, M. B., & Moser, E. I. (2018). Integrating
718 time from experience in the lateral entorhinal cortex. *Nature*, 561(7721), 57-62.
- 719 97. Rybakken, E., Baas, N., & Dunn, B. (2019). Decoding of neural data using cohomological feature
720 extraction. *Neural Computation*, 31(1), 68-93.
- 721 98. Chaudhuri, R., Gerçek, B., Pandey, B., Peyrache, A., & Fiete, I. (2019). The intrinsic attractor
722 manifold and population dynamics of a canonical cognitive circuit across waking and sleep. *Nature*
723 *Neuroscience*, 22(9), 1512-1520.
- 724
- 725
- 726
- 727
- 728
- 729
- 730
- 731
- 732
- 733
- 734
- 735
- 736

737 **Legends:**

738 **Figure 1**

739 **Ultraslow oscillations in calcium activity of MEC neurons.**

740 **a.** Schematic representation of the experimental set-up. Neural activity is monitored through a prism
741 from GCaMP6m-expressing neurons of the medial entorhinal cortex (MEC) in head-fixed mice running
742 in darkness on a non-motorized running wheel. Mice alternate freely between running and rest.

743 **b.** Stacked autocorrelations of single-cell calcium activity for one example session (3600 s, or 1 h, of
744 continuous recording, 484 neurons; session 17 from animal #60584.). Each row is the autocorrelation of
745 one cell's deconvolved and binarized calcium activity (subsequently referred to as the cell's "calcium
746 activity"), plotted as a function of time lag. Z-scored autocorrelations are color-coded. Left: Neurons are
747 sorted according to the maximum power of the power spectral density (PSD) calculated on each
748 autocorrelation separately, in a descending order. The vertical bands suggest that single cell calcium
749 activity is periodic. Right: The same neurons sorted according to peak frequency in the PSD. The curved
750 nature of the bands illustrates that while most cells exhibited slow oscillation, the frequency of the
751 oscillation showed some variation across cells.

752 **c.** PSD (left) calculated on the autocorrelation (right) of one example cell's calcium activity. The dashed
753 red line indicates the primary frequency at which the PSD peaks. The sole narrow peak at 0.0066 Hz is
754 mirrored by the well-defined oscillatory pattern in the autocorrelation.

755 **d.** As in (c) but for another example cell. The PSD peaks at 0.0066 Hz and has harmonics at 0.0132, 0.0207
756 and 0.0273 Hz.

757 **e.** As in (c) but for another example cell in the same recording. The PSD peaks at 0.0038 Hz and 0.0264
758 Hz. Both peaks are much wider than in (c), corresponding to a weaker oscillatory pattern in the
759 autocorrelation.

760

761 **Figure 2**

762 **Ultraslow oscillations in MEC consist of neuronal sequences.**

763 **a.** Raster plot representation of the matrix of calcium activity obtained after stacking the calcium activity
764 of all cells recorded in one experimental session (same as in Fig. 1b). Each row of the raster plot shows
765 the calcium activity of one neuron plotted as a function of time (in seconds, bin size 129 ms). Time bins
766 with calcium events are indicated with black dots. Time bins with no calcium events are white. Neurons
767 are sorted according to the correlation between the calcium activity. The sorting revealed sequences of
768 neuronal activity. One example sequence is indicated in red. Notice the slow temporal scale of the
769 sequences (121 s for the highlighted sequence).

770 **b.** As in (a) but now with neurons sorted according to the PCA method, where we calculated for each
771 cell the arctangent of the ratio between the cell's loading on principal component 2 (PC2) and PC1, and
772 then sorted the cells according to those values in a descending manner.

773 **c.** As in (b) but showing the fluorescence calcium signals instead of the deconvolved calcium activity. Z-
774 scored calcium signals are color-coded. Neurons are sorted according to the PCA method.

775 **d.** Projection of neural activity of the session presented in (a-c) onto a low-dimensional embedding
776 defined by the first two principal components of PCA (left), and by the first two dimensions of a LEM
777 analysis (right). Time is color-coded. Neural trajectories are circular, with population activity propagating

778 along a ring-shaped manifold. One full rotation of the population activity along the ring-shaped manifold
779 is defined as a “cycle” of the population oscillation.

780 **e.** Raster plot as in (b), with the phase of the oscillation overlaid in red (right y axis: phase of the
781 oscillation in radians).

782 **f.** Left: Distance d between two neurons in the PCA sorting is calculated as the difference between the
783 angles of the vectors defined by the loadings of each neuron on PC1 and PC2 with respect to PC1. The
784 schematic shows the distance between two neurons, one in orange and the other in green. The length
785 of the vectors is disregarded in this quantification. Right: Joint distribution of the time lag τ that
786 maximizes the cross-correlation between the calcium activity of any given pair of neurons and their
787 distance d in the PCA sorting. Color code: normalized frequency, each count is a cell pair. The increasing
788 relationship between τ and d indicates sequential organization of neural activity.

789 **g.** Distribution of cycle lengths across 15 oscillatory sessions over 5 animals (one animal did not have
790 detectable oscillations, 421 cycles in total). Each count is an individual cycle.

791 **h.** Cycle lengths shown separately for each animal with oscillations (421 cycles in total). For each animal
792 all oscillatory sessions were pooled. Cycle length was heterogenous across sessions and animals.

793 **i.** Distribution of inter-cycle intervals (ICI; 406 ICIs in total across 15 oscillatory sessions). Each count is
794 an ICI. During uninterrupted oscillations the ICI is 0.

795

796 **Figure 3**

797 **Nearly all MEC neurons are locked to the population oscillation**

798 **a.** Left: Distribution of locking degrees for all imaged neurons in the example session in Fig. 2a. The
799 locking degree, computed as the length of the mean vector over the distribution of phases at which
800 calcium events occurred, takes values between 0 (absence of locking) and 1 (perfect locking). Black dots
801 indicate locked neurons, red dots non-locked neurons, grey dots the 99th percentile of the null
802 distribution used to assess locking. For locked cells the locking degree is larger than the 99th percentile
803 of the null distribution (458 of 484 cells were locked to the phase of the oscillation). Neurons are sorted
804 according to their locking degree in an ascending manner. Bin size = 129 ms. Right: Distribution of values
805 of mutual information (MI, in bits) between the phase of the oscillation and the counts of calcium events
806 (“event counts”) for all imaged neurons in the example session in Fig. 2a. Black dots indicate the values
807 of MI and grey dots the estimated bias in the MI. For all cells the MI is larger than the bias. Neurons are
808 sorted according to their MI value in an ascending manner. Bin size = 0.52 s.

809 **b.** Box plot showing percentage of locked neurons over all sessions (median = 94%; one sample t-test
810 for a null hypothesis of 50% locked and non-locked cells, $n=15$ oscillatory sessions, $p = 1 \times 10^{-15}$,
811 $t = 38.6$). Red line indicates median across sessions, bottom and top lines in blue indicate lower and
812 upper quartiles, respectively. The length of the whiskers indicates 1.5 times the interquartile range. Red
813 crosses show outliers exceeding 1.5 times the interquartile range. *** $p < 0.001$, ** $p < 0.01$, * $p < 0.05$,
814 n.s. $p > 0.05$.

815 **c.** Tuning of single cell calcium activity to the phase of the oscillation. Left: Each row indicates the tuning
816 curve of one locked neuron of the example session in Fig. 2a ($n = 458$ locked cells). Right: Same as left,
817 but now for the tuning curves obtained in one shuffle realization of the data in which the calcium events
818 were temporally shuffled. Tuning curves were calculated by determining the fraction of event counts
819 across phase bins of the oscillation (bin size ~ 0.16 rad, 40 bins in total). Tuning curves are color coded.

820 **d.** Left: Distribution of participation indexes across neurons in the example session shown in Fig. 2a ($n =$
821 484 cells). The participation index (PI) quantifies the extent to which a cell's calcium activity is distributed
822 across all cycles of the population oscillation, or rather concentrated in a few cycles, regardless of its
823 locking degree. PI was calculated for each cell separately as the number of cycles needed to account for
824 90% of the total number of event counts. Right: Distribution of participation indexes across all 15
825 oscillatory sessions ($n = 6231$ cells). Each count in each of the plots is a neuron.

826 **e.** Anatomical distribution of neurons in the field of view (FOV) of the example session in Fig. 2a. The
827 preferred phase of each neuron, calculated as the mean phase at which the calcium events occurred, is
828 color-coded. Neurons in red are not significantly locked to the phase of the oscillation. The preferred
829 phases are anatomically intermingled. Dorsal MEC on top, medial on the right, as in Extended data Fig.
830 1.

831 **f.** Left: Box plot of pairwise anatomical distances between cells with similar preferred phase (each cell
832 in the pair has a preferred phase ~ 0 rad) or different preferred phase (one cell in the pair has a preferred
833 phase ~ 0 , and the other one a preferred phase $\sim \pi$ rad). Data are for the example session in Fig. 2a
834 ($n = 990$ distances in the similar group, 2025 distances in the different group, $p = 0.65$, $Z = 0.46$,
835 Wilcoxon rank-sum test). Right: Similar to the left panel but for all 15 oscillatory sessions, including the
836 example session in the left panel ($p = 0.80$, $Z = 0.25$, Wilcoxon rank-sum test). A fraction of 10% of the
837 total number of locked cells was used to define the groups with preferred phase ~ 0 rad or $\sim \pi$ rad.
838 Symbols as in Fig. 3b.

839 **g.** Same as (e) but for the participation index. Note that also the PIs are anatomically intermingled.

840 **h.** Similar to (f) but for the participation index. Left: Box plot of pairwise anatomical distances between
841 cells with similar or different participation indexes for the example session in Fig. 2a ($n = 990$ distances
842 in the similar group, 2025 distances in the different group, $p = 0.62$, $Z = 0.5$, Wilcoxon rank-sum test).
843 Right: Similar to the left panel but for all 15 oscillatory sessions, including the example in the left panel
844 ($n = 15$ sessions, $p = 0.87$, $Z = 0.17$, Wilcoxon rank-sum test). A fraction of 10% of the total number of
845 locked cells was used to define the groups with small and large participation indexes. Symbols as in Fig.
846 3b.

847

848 **Figure 4**

849 **The population oscillation consists of unidirectional periodic activity sequences**

850 **a.** Schematic of the process for splitting neurons into ensembles of co-active cells. Neurons sorted
851 according to the PCA method are allocated to 10 equally sized ensembles (color-coded).

852 **b.** Left: Matrix of transition probabilities between pairs of ensembles at consecutive time points. Data
853 are from the example session in Fig. 2a (bin size = 15.12 s). Right: Same as left panel but for one shuffle
854 realization. Transition probabilities are color coded. In the left diagram, note the higher probability of
855 transitions between consecutive ensembles (increased probabilities near the diagonal), the
856 directionality of transitions (increased probabilities above diagonal) and the periodic boundary
857 conditions in ensemble activation (presence of transitions from ensemble 10 to ensemble 1).

858 **c.** Probability of sequential ensemble activation as a function of the number of ensembles that are
859 sequentially activated (mean \pm S.D.; For 3-9 ensembles: $n = 15$ oscillatory sessions, 7500 shuffle
860 realizations, $p \leq 5.4 \times 10^{-11}$, range of Z values: 6.45 to 59.18, one-tailed Wilcoxon rank-sum test).
861 Blue, recorded data; orange, shuffled data. For each session, the probability of sequential ensemble

862 activation was calculated over 500 shuffled realizations, and shuffled realizations were pooled across
863 sessions.

864

865 **Figure 5**

866 **The MEC population oscillation is independent of movement**

867 **a.** Top: raster plot of one recorded session (30 min, 520 neurons). Time bins colored in blue indicate that
868 the animal ran faster than 2 cm/s. Inset indicates 160 s of neural activity. Middle: Instantaneous speed
869 of the animal. Bottom: Position of the animal on the wheel, expressed relative to an arbitrary point on
870 the wheel.

871 **b.** Box plot showing probability of observing the population oscillation given that the animal was either
872 running or immobile (median probability of oscillations during running = 0.93; median probability of
873 oscillations during immobility = 0.69; two sample Wilcoxon signed-rank test on the probability of
874 oscillation for running vs. immobility, $n = 10$ oscillatory sessions over the 3 animals that had the tracking
875 synchronized to imaging, $p = 0.002$, $W = 55$). Box-plot symbols as in Fig. 3b.

876 **c.** Fraction of immobility epochs with population oscillation as a function of length of the immobility
877 epoch (mean \pm S.D.). For each length bin, the fraction of immobility epochs with population oscillation
878 was averaged across sessions ($n = 10$ oscillatory sessions over 3 animals). Note the continued presence
879 of oscillations during extended immobility intervals. Blue: recorded data ($n = 10$ per length bin); Orange:
880 shuffled data ($n = 5000$ per length bin, 500 shuffled realizations per session were pooled). Recorded vs
881 shuffled data: $p \leq 2.62 \times 10^{-6}$, $4.7 \leq Z \leq 47.5$, Wilcoxon rank-sum test.

882 **d.** Number of completed laps as a function of cycle number. Each dot indicates one individual cycle.
883 Three sessions recorded in one animal are pooled. Dashed line indicates separation between sessions.

884 **e.** Distribution of speed values during the fraction of the session with population oscillation (blue bars;
885 $n = 167389$ time bins across cycles of 10 oscillatory sessions, bin size = 129 ms) and for the entire session
886 (blue solid line, with and without oscillation; $n = 238505$ time bins across 10 oscillatory sessions over 3
887 animals, bin size = 129 ms). Note the almost identical shape of the distributions, suggesting there is no
888 specific range of speed values associated with the population oscillation.

889 **f.** As in (e) but for the distribution of acceleration values. There is no difference in the range of
890 acceleration values during the fraction of the session with population oscillation.

891

892 **Figure 6**

893 **The population oscillation is not observed in parasubiculum or visual cortex.**

894 **a,b.** Stacked autocorrelations for two example sessions recorded in parasubiculum (a, PaS; 1800 s, 402
895 simultaneously recorded neurons) and visual cortex (b, VIS; 1800 s, 289 simultaneously recorded
896 neurons). Each row is the autocorrelation of one cell's calcium activity, plotted as a function of time lag.
897 Z-scored autocorrelations are color-coded. Cells are sorted according to maximum power (left of each
898 panel) or peak frequency (right of each panel) of the PSD, as in Fig. 1b.

899 **c,d.** PCA-sorted raster plots (as in Fig. 2b) for two example sessions recorded in PaS (Fig. 6a) and VIS (Fig.
900 6b). Notice lack of stereotyped sequences of activity. Oscillation score and sequence score are indicated
901 at the top.

902 **e,f.** Joint distributions of time lag τ that maximizes the cross-correlation between any given pair of
903 neurons and their distance d in the PCA sorting (as in Fig. 2f), applied to the recordings in Fig. 6a (PaS)
904 and 6b (VIS). Normalized frequency is color-coded. Notice lack of linear relationship between d and τ ,
905 in contrast to Fig. 2f.

906 **g.** Number of sessions with and without population oscillation in MEC (blue, 27 sessions in total), VIS
907 (green, 19 sessions) and PaS (yellow, 25 sessions) based on oscillation scores and threshold defined from
908 the MEC dataset (see Extended data Fig. 4c).

909 **h.** Transition probabilities between ensembles across consecutive time bins (bin size ~ 8.5 s) for the PaS
910 example session in Fig. 6a (left) and the VIS example session in Fig. 6b (right). Symbols as in Fig. 4b.

911 **i.** Probability of sequential ensemble activation as a function of the number of ensembles that are
912 sequentially activated in PaS (left) and VIS (right) (mean \pm S.D.). Blue, recorded data (25 PaS sessions; 19
913 VIS sessions); orange, shuffled data. For each session, the probability of sequential ensemble activation
914 was calculated over 500 shuffled realizations, and shuffled realizations were pooled across sessions for
915 each brain area separately. Probability is shown on a log-scale. In PaS the probability of long sequences
916 was significantly larger in experimental data than in shuffled data (For 3-7 ensembles: $n = 25$ PaS
917 sessions, 12500 shuffled realizations, range of p values: 5.7×10^{-4} to 0.036, range of Z values: 1.80 to
918 3.25, one-tailed Wilcoxon rank-sum test). This was not the case in VIS (For 3-6 ensembles: $n = 19$ VIS
919 sessions, 9500 shuffled realizations, range of p values: 0.09 to 0.99, range of Z values: -3.34 to 1.36,
920 one-tailed Wilcoxon rank-sum test).

921

922 **Extended data Figure 1**

923 **Histology showing imaging locations for each animal in the MEC group**

924 **a.** Left: Representative sagittal image indicating GCaMP6m expression in the superficial layers of the
925 MEC upon local viral injection at postnatal day P1 (sagittal section). Images were acquired with a 20 \times
926 objective mounted on a confocal laser scanning microscope LSM 880 (Zeiss). Scale bar 500 μ m. Red inset
927 and top right: 60 \times magnification of the most dorsal portion of the MEC. Scale bar 150 μ m. Bottom right:
928 Fraction of neurons in the image that express GCaMP6m; data are shown for all 5 animals with MEC
929 imaging. Error bar indicates the S.D. calculated across multiple adjacent slices.

930 **b.** Location of the ventro-lateral edge of the prism in stereotactic coordinates, and area of the FOV
931 occupied by cells expressing GCaMP6m. Data are shown for each MEC-imaged animal. Mouse #59911
932 had no oscillations.

933 **c.** Prism location in mice that underwent calcium imaging in MEC. Top: Maximum intensity projections
934 of 50 μ m thick sagittal brain sections. For each of the 5 mice in (b), 3 sections, shown from lateral (left)
935 to medial (right), were acquired with an LSM 880, 20 \times . A DiL-coated piano wire pin was inserted at the
936 ventrolateral corner of FOV to enable identification of the FOV on histology sections. Green is GCaMP6m
937 signal, red is DiL signal. Scale bar is 400 μ m. The white stippled line encapsulates the superficial layers
938 of MEC. The blue dot adjacent to the leftmost image of the series marks the location of the ventro-
939 lateral corner of the prism. Bottom: estimated location of the FOV for two-photon imaging, projected
940 onto a flat map encompassing MEC (brown outline) and parasubiculum (PaS, yellow outline). The blue
941 dot marks the location of the pin used to demarcate the most lateral-ventral border of the prism, while
942 the green square inset is the microscope's FOV. Inset images show the mean (left) and maximum (right)
943 intensity projections of the FOV. Anteroposterior (AP) and dorsoventral (DV) axes are indicated in panels
944 a and c.

945 **Extended data Figure 2**

946 **Relationship between the population oscillation and behavior**

947 **a.** Quantification of the animals' behavior during head-fixation on the wheel. Distribution of duration of
948 running (speed ≥ 2 cm/s, left) and immobility (speed < 2 cm/s, right) epochs for 10 oscillatory sessions
949 over the 3 animals with synchronized behavioral tracking and imaging (1289 running bouts and 1286
950 immobility bouts in total). Each count is an epoch.

951 **b.** Left: Schematic of the change in phase of the oscillation during immobility epochs that were longer
952 than 25 s and that occurred during the population oscillation. Right: 44 of these epochs from the same
953 3 mice as in (a). As in the schematic on the left, each line represents the progression of the phase of the
954 oscillation (y axis, from $-\pi$ to π rad) as a function of time (x axis, in seconds). The start of each immobility
955 epoch is aligned at $t=0$, and the epoch lasts for as long as the line continues. Different epochs have
956 different lengths, covering a range from 25 s to 258 s. For visualization purposes only the first 120 s are
957 displayed (3 of the epochs were truncated; these had durations of 127.9, 258.2, 136.1 s). Sudden
958 transitions from π to $-\pi$ rad reflect the periodic nature of the oscillation.

959 **c.** Number of completed laps on the wheel per cycle of the population oscillation as a function of the
960 cycle number after pooling sessions (range of completed laps on rotating wheel across 10 sessions = 10-
961 1164, median = 624). Sessions are pooled for each animal separately (mouse #60584, 4 sessions; mouse
962 #60585, 3 sessions; the third animal is shown in Fig. 5d). Each dot indicates one individual cycle. The
963 dashed line indicates separation between sessions.

964 **d.** Left: To determine whether the population oscillation is modulated by onset of running we calculated
965 the mean running speed during time intervals of 10 s right before and right after the cycle onset (one
966 sample Wilcoxon signed-rank test on the difference between speed before and after cycle onset, $n =$
967 310 cycle onsets over 10 sessions from 3 animals, $p = 0.82$, $W = 25$). Right: Same as left but only for
968 cycles that were 10 s or more apart, i.e. for cycles belonging to different oscillatory epochs (one sample
969 Wilcoxon signed-rank test on the difference between speed before and after cycle onset, $n = 70$ cycle
970 onsets over 10 sessions from 3 animals, $p = 0.12$, $W = 857$). Note that there is no systematic change
971 in speed after onset of cycles.

972 **e-h.** Examples of fractions of sessions with increased speed after cycle onset (exceptions from the
973 general pattern shown in d). Top of each panel: Raster plots, symbols as in Fig. 2a (bin size = 129 ms).
974 Bottom of each panel: Instantaneous speed of the animal during the recording in the top panel. Length
975 of the displayed fraction of the session was 400, 1000, 400 and 500 s, respectively, for (e-h). Notice that
976 while speed is higher after onset of the cycle in these examples, the increase of speed does not always
977 occur right after cycle onset, but sometimes before (e,f), and sometimes tens of seconds after (g,h).

978

979 **Extended data Figure 3**

980 **Oscillatory sequences shown by cell sorting based on correlation or dimensionality reduction**

981 **a.** Left: Because neural activity progresses sequentially, the time lag that maximizes the correlation
982 between the calcium activity of pairs of cells increases with their distance in the correlation sorting.
983 Sorting is performed as in Fig. 2a. Time lag is expressed in seconds, distance is expressed as the number
984 of cells between the two cells in the sorting. Notice that for large distances (e.g. > 300 cells), the time
985 lag to peak correlation is either larger than 60 s or close to zero. This bimodality is due to the periodicity
986 of the MEC population oscillation. The dashed line indicates a linear regression ($n = 301$ cell pairs, $R^2 =$
987 0.17 , $p = 2 \times 10^{-14}$, the line was fitted between the intermediate samples to avoid the effect of the

988 periodic boundary conditions). Right: The cross correlation between the calcium activity of pairs of cells
989 is oscillatory and temporally shifted. Examples are shown for 3 cell pairs with different distances in the
990 sorting based on correlation values. Orange: cells are 5 cells apart; purple: cells are 199 cells apart;
991 green: cells are 401 cells apart. The dotted line indicates the time lag at which the cross correlation
992 peaks within the first peak. Note that the larger the distance between the cells in the sorting, the larger
993 the time lag that maximizes the cross correlation.

994 **b.** Schematic representation of the “PCA method”. Principal component analysis (PCA) was applied to
995 the binarized matrix of deconvolved calcium activity (“matrix of calcium activity”) of individual sessions
996 by considering every neuron as a variable, and every population vector as an observation. The first two
997 principal components (PC1, PC2) were identified. In the plane defined by PC1 and PC2 (left), the loading
998 of each neuron defines a vector, which has an associated angle $\theta \in [-\pi, \pi)$ with respect to the axis of
999 PC1 (in the schematic, neuron N_i (orange) is characterized by an angle θ_i). Neurons were sorted
1000 according to their angles θ in a descending order (right). Cyan: neuron sorting before application of the
1001 PCA method. Orange: neuron sorting after the application of the PCA method.

1002 **c.** Population oscillations consisting of oscillatory sequences are not revealed with a random sorting of
1003 the cells (top left) or when the PCA sorting method is applied to temporally shuffled data (middle left).
1004 A population oscillation similar to that of Fig. 2a,b (with correlation sorting or PCA method) is recovered
1005 when neurons are sorted according to non-linear dimensionality reduction techniques (UMAP, Isomap,
1006 LEM, t-SNE). Each row of each raster plot is a neuron, whose calcium activity is plotted as a function of
1007 time (as in Fig. 2a). Every black dot represents a time bin where a neuron was active (bin size = 129 ms).

1008 **d.** Projection of neural activity during the population oscillation onto a low-dimensional embedding
1009 generated by the first two principal components obtained by applying PCA to the matrix of calcium
1010 activity of each session. Each plot shows one session; all 15 oscillatory sessions are presented. Time is
1011 color-coded and shown in minutes, and the temporal range corresponds to all concatenated epochs
1012 with population oscillation in the session. Neural trajectories are circular, with population activity
1013 propagating along a ring-shaped manifold.

1014

1015 **Extended data Figure 4**

1016 **Sorted raster plots for the complete MEC dataset**

1017 **a:** PCA-sorted raster plots (as in Fig. 2b) for all analysed sessions across the 5 animals in which MEC
1018 population activity was recorded, sorted by animals and day of recording. Session numbering starts the
1019 first day of habituation on the wheel, with 15 habituation sessions. One session was recorded per day,
1020 and recordings were conducted on consecutive days. Note that sessions had lengths of approximately
1021 1800 s or 3600 s. Oscillation score and sequence score were calculated for each session separately and
1022 are indicated at the top right corner of every calcium matrix. The scores colored in green correspond to
1023 sessions with population oscillation (see panel c), scores colored in red to sessions without population
1024 oscillation.

1025 **b:** Example sessions with (top) and without (bottom) population oscillation. These sessions were
1026 recorded in the same area of the MEC in the same animal, but on different days (Mouse #60355 in panel
1027 a). Left: Raster plots of the matrices of calcium activity. Right: Joint distributions of the time lag τ that
1028 maximizes the correlation between the calcium activity of any given pair of neurons and their distance
1029 d in the PCA sorting (as in Fig. 2f). Color code: normalized frequency, each count is a cell pair. Notice the
1030 lack of linear pattern in the session without population oscillation.

1031 **c.** Left: Distribution of oscillation scores for sessions recorded in MEC (27 sessions in total over 5
1032 animals). Each count is a session. The oscillation score quantifies the extent to which single cell calcium
1033 activity is periodic, and ranges from 0 (no oscillations) to 1 (oscillations). Dashed line: Threshold used
1034 for classifying sessions as oscillatory (oscillation score ≥ 0.72) or non-oscillatory sessions (oscillation
1035 score < 0.72). The threshold was chosen based on the bimodal nature of the distribution. Right: List of
1036 sessions sorted by animal and number of sessions the animals experienced on the wheel. Session
1037 numbering as in panel a. Red, sessions classified as not oscillatory; green, session classified as oscillatory.

1038

1039 **Extended data Figure 5**

1040 **Identification of individual cycles and population oscillation characterization**

1041 **a.** Top: Raster plot of the PCA-sorted matrix of calcium activity of the example session in Fig. 2a. Bottom:
1042 Phase of the oscillation calculated on the session shown in the top panel is shown in black, and phase of
1043 individual cycles is colored in cyan. During one cycle of the population oscillation the phase of the
1044 oscillation traversed $[-\pi, \pi)$ rad. To identify individual cycles, first the phase of the oscillation was
1045 calculated across the entire session, second discontinuities in the succession of such phases were
1046 identified and used to extract putative cycles and third, putative cycles were classified as cycles if the
1047 phase of the oscillation progressed smoothly and in an ascending manner, allowing for the exception of
1048 small fluctuations (lower than 10% of 2π , e.g. as in the sequence at 500 s). Points of sustained activity
1049 were ignored. Fractions of cycles in which the phase of the oscillation traversed 50% or more of the
1050 range $[-\pi, \pi)$ rad were also analysed (for example at the beginning of the session).

1051 **b.** Total number of individual cycles per session, across 15 oscillatory sessions. Animal number is color-
1052 coded.

1053 **c.** Box plot showing mean event rate as a function of cycle segment for all 15 oscillatory sessions. Each
1054 cycle was divided into 10 segments of equal length, and for each cycle segment the mean event rate
1055 was calculated as the total number of calcium events across cells divided by the length of the segment
1056 and the number of recorded cells. Red lines indicate median across sessions, the bottom and top lines
1057 in blue indicate lower and upper quartiles, respectively. The length of the whiskers indicates 1.5 times
1058 the interquartile range. Red crosses show outliers that lie more than 1.5 times outside the interquartile
1059 range. The mean event rate remained approximately constant across the length of the cycle. While a
1060 non-parametric analysis revealed an overall difference ($n = 15$ oscillatory sessions per segment,
1061 $p=0.0052$, $\chi^2=23.49$, Friedman test), the rate change from the segment with minimum to maximum
1062 event rate was no more than 18% and there were no significant differences in the event rate between
1063 pairs of segments (Wilcoxon rank-sum test with Bonferroni correction, $p>0.05$ for all pairs). *** $p <$
1064 0.001 , ** $p < 0.01$, * $p < 0.05$, n.s. $p > 0.05$.

1065 **d.** Box plot of cycle length for each cycle of the oscillation, for the 15 oscillatory sessions. Note the
1066 relatively fixed length of cycles in individual sessions. Symbols as in (c).

1067 **e.** Left: Box plot of the standard deviation of cycle length within a session, in experimental and shuffled
1068 data. The standard deviation of cycle length is smaller in the experimental data ($n = 15$ oscillatory
1069 sessions, 7500 shuffle realizations, $p = 1.8 \times 10^{-7}$, $Z = 5.08$, one-tailed Wilcoxon rank-sum test). Right:
1070 Box plot of the ratio between the shortest cycle length and the longest cycle length for all pairs of cycles
1071 within and between sessions. This fraction is larger for cycle pairs in the within-session group ($n = 15$
1072 oscillatory sessions, the mean fraction per session and group was calculated separately, $p = 1.7 \times 10^{-6}$,
1073 $Z = 4.64$, one-tailed Wilcoxon rank-sum test). Notice that for each cycle pair, the larger this ratio, the
1074 more similar the length of the cycles are.

1075 **f.** The cycle length is not correlated with the number of recorded cells in the session ($n = 421$ cycles
1076 across 15 oscillatory sessions, $\rho = 0.02$, $p = 0.64$, Spearman correlation). Each dot is a cycle. Animal
1077 number is color-coded as in (b).

1078 **g.** Fraction of the session in which the MEC population engaged in the oscillation. Session length was 30
1079 min for mice 59914 and 60355, and 60 min for mice 60584 and 60585.

1080 **h.** Duration of the longest epoch with uninterrupted population oscillation. Only epochs that met the
1081 strict criterion of no separation between cycles were considered.

1082

1083 **Extended data Figure 6**

1084 **Characterization of locking degree and participation index**

1085 **a.** Consistency between two measures of phase locking for individual neurons. The locking degree was
1086 calculated for each cell as the length of the mean vector over the distribution of oscillation phases ($[-\pi, \pi)$ rad)
1087 at which the calcium events occurred (bin size = 129 ms). The locking degree was consistent
1088 with the mutual information between the calcium event counts and the phase of the oscillation (bin size
1089 = 0.52 s). Scatter plots show the relation between the two measures, with each dot representing one
1090 neuron. Left: Data from the example session in Fig. 2a ($n = 484$ cells). Right: All neurons from all 15
1091 oscillatory sessions are pooled ($n = 6231$ cells). Red dots indicate neurons that did not meet criteria for
1092 locking. The consistency between the two measures strengthens the conclusion that the vast majority
1093 of the neurons in MEC are locked to the population oscillation.

1094 **b.** Left: Box plot comparing locking degree for cells with an oscillatory frequency that was similar
1095 (relative frequency ~ 1) or different (relative frequency $\neq 1$) from the frequency of the population
1096 oscillation in the example session in Fig. 2a ($n = 48$ cells in each group, $p = 3.4 \times 10^{-11}$, $Z = 6.63$,
1097 Wilcoxon rank-sum test). Right: As left panel but for the locking degree across all 15 oscillatory sessions,
1098 including the example in the left panel ($n = 15$ sessions, $p = 2.8 \times 10^{-5}$, $Z = 4.19$, Wilcoxon rank-sum
1099 test). Ten per cent of the total number of cells was used to define each of the groups with similar
1100 (relative frequency ~ 1) and different (relative frequency $\neq 1$) oscillatory frequency as compared to the
1101 population oscillation frequency. Relative frequency was calculated for each cell as the oscillatory
1102 frequency of the cell's calcium activity divided by the oscillatory frequency of the population oscillation
1103 in the session. Symbols as in Fig. 3b. Note that cells with relative frequency similar to 1 are more locked
1104 to the phase of the oscillation. For all percentages considered to define similar and different groups (5,
1105 10, 20, 30, 40, and 50%) the p-values were significant.

1106 **c.** Histogram showing the distribution of single-cell oscillatory frequency divided by the population
1107 oscillation frequency of the session ($n = 6231$ cells pooled across 15 oscillatory sessions). A value of 1.0
1108 indicates that single-cell and population frequency coincide. The left and right dashed lines indicate 25th
1109 (0.52) and 75th (1.08) percentiles respectively. Note that for approximately half of the data the oscillatory
1110 frequency is very similar at single-cell and population level.

1111 **d.** The population oscillation remains visible after excluding increasing fractions of neurons and keeping
1112 only those with the lowest locking degree. Each row shows a PCA-sorted raster plot (left, symbols as in
1113 Fig. 2b) and the corresponding joint distributions of the time lag τ that maximizes the correlation
1114 between the calcium activity of neuron pairs and their distance d in the PCA sorting (right, symbols as
1115 in Fig. 2f). The fraction of included neurons is indicated on top of the raster plot. For building the raster
1116 plots neurons were sorted according to their locking degree value and neurons with the highest locking
1117 degrees were removed.

1118 **e.** Distribution of preferred phases (the mean phase at which the calcium events occurred) in the
1119 population of locked neurons for all 15 oscillatory sessions. Black line indicates the preferred phases;
1120 red intervals indicate one standard deviation (calculated over the oscillation phases at which the calcium
1121 events of an individual cell occurred). Neurons are sorted according to their preferred phase in an
1122 ascending manner. The preferred phases cover the entire range of phases from $-\pi$ to π .

1123 **f.** Phase preferences are distributed evenly across the MEC cell population. Left: The nearly-flat nature
1124 of the phase distribution is illustrated by comparing the entropy of the distribution of preferred phases
1125 in recorded (y axis) and shuffled data (x axis). H_{ratio} is the entropy of the distribution of preferred phases
1126 (calculated as in e) estimated from the data and divided by the entropy of a flat distribution ($H_{\text{ratio}} = 1$ if
1127 the distribution of preferred phases is perfectly flat, $H_{\text{ratio}} = 0$ if all neurons have the same preferred
1128 phase). Each point in the scatterplot indicates one session (15 sessions). Horizontal error bars indicate
1129 one S.D across shuffled realizations. The black dashed line indicates identical values for recorded and
1130 shuffled data. Animal number if color-coded. Notice the discontinuity in the y axis between 0 and 0.85.
1131 H_{ratio} is substantially larger for recorded data than for shuffled data. Right: Box plot of H_{ratio} for recorded
1132 and shuffled data. For each session the 1000 shuffled realizations were averaged ($n = 15$ oscillatory
1133 sessions, $p = 6 \times 10^{-6}$, $Z = 4.52$, Wilcoxon rank-sum test). Symbols as in Fig. 3b.

1134 **g.** Three example neurons from the example session in Fig. 2a. Top: Raster plot of the calcium matrix
1135 shown in Fig. 2a. Calcium events from the neuron with high participation index (PI, 0.72) are highlighted
1136 in light blue; from the neuron with intermediate PI (0.56) are highlighted in purple; from the neuron
1137 with low PI (0.36) are highlighted in orange.

1138 Bottom three panels: Z-scored fluorescence calcium signals as a function of time from the above neurons
1139 with high (top), intermediate (middle), and low (bottom) PIs. Colored arrows represent the time points
1140 at which the population oscillation is at the neuron's preferred phase. Notice how the neuron with high
1141 PI tends to exhibit a peak in the calcium signal for most of the cycles. Neurons with intermediate and
1142 low PIs demonstrate the same but to a lesser extent, with the calcium signal not peaking in each cycle.

1143 **h.** Similar to (b), but for the participation index. Left: Data from the example session shown in Fig. 2a
1144 ($n = 48$ cells in each group, $p = 0.51$, $Z = 0.66$, Wilcoxon rank-sum test). Right: As left panel but for data
1145 pooled across 15 oscillatory sessions. The mean participation index was calculated for each group
1146 ("relative frequency ~ 1 " and "relative frequency $\neq 1$ ") and each session separately and the data was
1147 then pooled across sessions ($n = 15$ sessions, $p = 0.56$, $Z = 0.58$, Wilcoxon rank-sum test). For all
1148 percentages considered to define the similar and different groups (5, 10, 20, 30, 40, and 50%) the p -
1149 values were non-significant.

1150 **i.** Histogram of preferred phases for the two groups of cells used to quantify the anatomical distribution
1151 of preferred phases for the example session in Fig. 2a. Cells in group one (two) had preferred phase $\sim \pi$
1152 rad (~ 0 rad). Each group had 45 locked cells, which is approximately ten per cent of the total number
1153 of locked cells in that session (454). Group one: blue; group two: orange. Distances between cells in
1154 group one (similar preferred phase), or between one cell in group one and one cell in group two
1155 (different preferred phase) were calculated.

1156 **j.** p -value for the difference in anatomical distance between the groups of cell pairs with similar
1157 preferred phase or different preferred phase (defined as in panel i), as a function of the percentage of
1158 cells used to build the groups of cells. The p -value was obtained through a Wilcoxon rank-sum test ran
1159 on the anatomical distances between cells with similar preferred phase (cells in group one) and cells
1160 with different preferred phase (distance between one cell in group 1 and one cell in group 2, for all pairs
1161 of cells). For all percentages considered (5, 10, 20, 30, 40, and 50%), the mean distances for the similar
1162 and the different classes were computed for each session. The means were then pooled across sessions

1163 (n = 15 oscillatory sessions). The dashed line indicates a level of significance of 0.05. Note that all p-
1164 values are much larger than the level of significance.

1165 **k.** Similar to (i) but for participation indexes. Cells in group one (two) had small (large) participation
1166 index.

1167 **l.** Similar to (j) but for the participation indexes. Symbols as in (j).

1168

1169 **Extended data Figure 7**

1170 **The population oscillation consists of periodic sequences of ensemble activation**

1171 **a.** Schematic of calcium activity merging steps. We began by sorting the neurons according to the PCA
1172 method. Next, in successive iterations, or merging steps, we added up the calcium activity of pairs of
1173 consecutive neurons (merging step = 1) or consecutive ensembles (merging step > 1).

1174 **b.** Participation index (PI) as a function of merging step (mean \pm S.D.). Black trace, example session in
1175 Fig. 2a; red trace, all 15 oscillatory sessions. The more neurons per ensemble, the higher the
1176 participation index of the ensemble. Note that the participation index plateaus after 5 merging steps,
1177 which corresponds to approximately 10 ensembles (Wilcoxon rank-sum test to compare the
1178 participation indexes in merging steps 5 and 6; Black trace: $n = 30$ PIs in merging step 5, $n = 15$ PIs in
1179 merging step 6, $p = 0.23$, $Z = 1.20$; Red trace: $n = 15$ PIs in merging step 5 and 6, PIs of each merging
1180 step were averaged for each session separately, $p = 0.14$, $Z = 1.49$).

1181 **c.** Tuning of single cell calcium activity to ensemble activity calculated as the Pearson correlation
1182 between the calcium activity of each neuron and the activity of each ensemble for the example session
1183 in Fig. 2a. Ensemble activity was calculated as the mean calcium activity across neurons in the ensemble.
1184 Each row is the tuning curve of one neuron, and neurons are sorted according to the PCA method. For
1185 each neuron, the calcium activity was positively correlated with a small subset of consecutive
1186 ensembles, and negatively correlated with the others. Pearson correlation is color-coded.

1187 **d.** The relationship between the calcium activity of each neuron and the activity of each ensemble was
1188 expressed by a Pearson correlation, as in (c). By repeating this calculation for all neurons across all
1189 ensembles, we could identify, for each neuron, the most representative ensemble (the one with
1190 maximal Pearson correlation). Left: 2D histogram of the most representative ensemble of each neuron
1191 and the ensemble it was assigned to based on the PCA sorting. Data are for the example session in Fig.
1192 2a. Each count is a neuron; counts are color-coded (484 cells). Right: The same 2D histogram calculated
1193 on one shuffled realization of the data for the example session in Fig. 2a (484 cells). In the left diagram,
1194 note that the method for assigning cells into ensembles based on the PCA sorting correctly recovers the
1195 dependency between cells' calcium activity and ensemble activity (higher number of counts along the
1196 diagonal).

1197 **e.** Same as (d), but for all neurons across all 15 oscillatory sessions (left, $n = 6231$), or one shuffled
1198 realization of the data (right, $n = 6231$).

1199 **f.** Probability distribution showing, for recorded data and shuffled data, the distance, in numbers of
1200 ensembles, between the assigned ensemble based on the PCA sorting and the most representative
1201 ensemble (as in d). The probability was calculated as the number of times that one given distance was
1202 observed in one session divided by the total number of recorded cells. Each count was one neuron. Note
1203 that the distance between the most representative ensemble and the assigned ensemble based on the
1204 PCA sorting reflects the periodic boundary conditions in ensemble activation and ranges from 0 to 5 (x
1205 axis). 500 shuffled realizations per session were averaged and compared to the mean distance per

1206 session in the recorded data. The probability of finding small distances (lower than 2) was larger in the
1207 recorded data ($n = 15$ sessions, for distances of 0 to 5 ensemble: $p \leq 3.4 \times 10^{-6}$, range of Z : 4.64 to
1208 4.67; Wilcoxon rank-sum test), suggesting that single cell calcium activity was maximally correlated with
1209 the activity of the ensemble it was assigned to. Blue, recorded data; orange, shuffled data. Error bars
1210 indicate S.E.M.

1211 **g.** Ensemble activity oscillated at the same frequency as the population oscillation. Ensemble activity
1212 was calculated as the mean calcium activity across neurons in the ensemble. Power spectral density was
1213 calculated on the activity of each of the ten ensembles from the example session in Fig. 2a. Ensemble
1214 frequency was calculated as the peak frequency of the PSD, population oscillation frequency was
1215 computed as the total number of cycles (24 in this session) normalized by the amount of time in which
1216 the network engaged in the oscillation (~ 3600 s). The dashed line indicates the frequency of the
1217 population oscillation. Note that the dashed lines coincide with the peak of the PSD.

1218 **h.** Histogram showing the ratio between ensemble oscillatory frequency and population oscillation
1219 frequency in the session (calculated as in panel g; $n = 150$ data points given by 10 ensembles in each of
1220 the 15 oscillatory sessions). Each count is one ensemble. Note the two peaks at 1 and 2, indicating that
1221 ensembles tend to oscillate at the frequency of the population oscillation, or at an integer multiple of it.

1222 **i.** Anatomical distribution of recorded neurons for the example session in Fig. 2a. The ensemble each
1223 neuron has been assigned to based on the PCA sorting is color-coded. Neurons indicated in red were
1224 not locked to the phase of the oscillation. Note that ensembles are anatomically intermingled. Dorsal
1225 MEC on top, medial on the right, as in Extended data Fig. 1.

1226 **j.** Box plot of pairwise anatomical distance between neurons within an ensemble and between those
1227 neurons and the rest of the imaged neurons, i.e. across ensembles. Data are shown for each ensemble
1228 of the session in (i) (Wilcoxon rank-sum test to compare the within and across group distances for each
1229 ensemble separately; $n = 1125$ pairwise distances in the within ensemble group, except for ensemble
1230 10, in which $n = 1326$; $n = 20928$ pairwise distances in the across ensemble group, except for ensemble
1231 10, in which $n = 22464$, $0.0005 \leq p \leq 0.9528$, $0.06 \leq Z \leq 3.50$). Symbols as in Fig. 3b. Purple, distances
1232 between cells within one ensemble; green, distances between cells in different ensembles.

1233 **k.** Box plots of pairwise anatomical distance between neurons within one ensemble and across
1234 ensembles for the example session in (j) (left, $n = 10$ ensembles, $p = 0.57$, $Z = 0.57$, Wilcoxon rank-
1235 sum test) and across 15 oscillatory sessions including the example session in (j) (right). For each session
1236 the means for each of the “within” and “across” groups were computed across ensembles ($n = 15$
1237 oscillatory sessions, $p = 0.93$, $Z = 0.08$, Wilcoxon rank-sum test). Symbols as in (j).

1238 **l.** To quantify the temporal progression of the population activity at the time scale at which the
1239 population oscillation evolved, we calculated, for each session, an oscillation bin size. This bin size is
1240 proportional to the inverse of the peak frequency of the PSD calculated on the phase of the oscillation,
1241 and hence captures the time scale at which the oscillation progresses. The oscillation bin size is shown
1242 for each of the 15 oscillatory sessions.

1243 **m.** Schematic of the method for quantifying temporal dynamics of ensemble activity. For each session
1244 and each ensemble we calculated the mean ensemble activity at each time bin (oscillation bin size). Only
1245 the ensemble with the highest activity within each time bin (red rectangle) was considered. The number
1246 of transitions between ensembles in adjacent time bins divided by the total number of transitions was
1247 used to calculate the transition matrices in Fig. 4b.

1248 **n.** The ensemble with the highest activity in each time bin, indicated in yellow and calculated as in (m),
1249 plotted as a function of time for the example session in Fig. 2a. All other ensembles are indicated in
1250 purple. Notice that the transformation in (m) preserves the population oscillation.

1251 **o.** Box plot showing transition probabilities between consecutive ensembles for all 15 oscillatory
1252 sessions. The probabilities remain approximately constant across transitions between ensemble pairs
1253 ($n = 15$ oscillatory sessions per transition, $p = 0.56$, $\chi^2 = 7.77$, Friedman test), and there were no
1254 significant differences between pairs of transitions (Wilcoxon rank-sum test with Bonferroni correction,
1255 $p > 0.05$ for all transitions). Symbols as in Fig. 3b.

1256 **p.** We further visualized the structure of the transitions in Fig. 4b by using the transition matrix as an
1257 adjacency matrix to build a directed weighted graph. Nodes indicate ensembles (color-coded as in m).
1258 Edges (lines) between any two nodes represent the transition probabilities between any two ensembles.
1259 The thickness of the edge is proportional to the value of the transition probability, while the arrows on
1260 each edge indicate the directionality of the transition. Red edges indicate edges whose associated
1261 transition probability is significant. Edges with significant transition probability were only found
1262 between consecutive or nearby nodes as well as between the nodes corresponding to ensemble 1 and
1263 10, once again mirroring the periodic boundary conditions in ensemble activation. In shuffled
1264 realizations of the data there were edges that corresponded to significant transition probabilities, but
1265 those were not between neighboring nodes.

1266 **q.** Scatter plot showing relation between oscillation score and sequence score. The oscillation score
1267 quantifies the extent to which the calcium activity of single cells is periodic and ranges from 0 (no
1268 oscillation) to 1 (oscillation). The sequence score quantifies the probability of observing sequential
1269 activation of 3 or more ensembles. Each dot corresponds to one session. The sequence score increases
1270 with the oscillation score, and is highest for oscillatory sessions. Note that non-oscillatory sessions
1271 display non-zero values of sequence score, indicating the presence of sequential ensemble activity also
1272 in sessions below criteria for oscillation.

1273 **r.** Percentage of sessions with significant sequence score in sessions classified as oscillatory vs non-
1274 oscillatory. In MEC sessions with oscillations, 100% (15 of 15) of the sessions showed significant
1275 sequence scores, while in MEC sessions without oscillations, 41% (5 of 12) of the sessions demonstrated
1276 significant sequence scores. For corresponding raster plots, see Extended data Fig. 4a.

1277

1278 **Extended data Figure 8**

1279 **Histology showing imaging location in animals with FOVs in parasubiculum and visual cortex**

1280 **a.** Histological determination of prism location in parasubiculum-implanted mice. Top: Maximum
1281 intensity projection of 50 μm thick sagittal brain sections (sections acquired with an LSM 880, 20x). Three
1282 consecutive sections from the same mouse are shown, from the most lateral (left) to the most medial
1283 (right). Green is GCaMP6m signal, while red is Di I signal (used to demarcate ventrolateral corner of the
1284 prism, as in Extended data Fig. 1). Scale bar is 400 μm . The white stippled line encapsulates the
1285 superficial layers of the parasubiculum (PaS). Dorsal PaS on top, layer 1 on the left. Bottom: Estimated
1286 location of the field of view (FOV) on a flat map encompassing MEC (brown outline) and PaS (yellow
1287 outline). The blue dot marks the location of the pin used to demarcate the most lateral-ventral border
1288 of the prism, while the green square inset shows the microscope FOV. Inset images show mean (left)
1289 and maximum (right) intensity projections of the FOV. Dorsoventral (DV), and mediolateral (ML) axes
1290 are indicated.

1291 **b.** Location of the ventro-lateral edge of the prism in stereotactic coordinates, and area of the FOV
1292 occupied by cells expressing GCaMP6m for each PaS-imaged animal.

1293 **c.** Histological determination of imaging location in the visual cortex (VIS) in mice that underwent
1294 calcium imaging. Green is GCaMP6m signal. Images are taken from coronal slices, and zoomed in on
1295 visual cortex (Scale bar is 100 μ m; L1 at the top, L6 at the bottom). Dorsal pole of the brain is on top.
1296 Maximum intensity projection, LSM 880, 20x.

1297

1298 **Extended data Figure 9**

1299 **Lack of population oscillations in parasubiculum and visual cortex**

1300 **a:** Alternative sorting methods, as in Extended data Fig. 3c, but applied to sessions recorded in the PaS
1301 (left) or VIS (right). The PCA sorting method applied to temporally shuffled data did not unveil a
1302 population oscillation (first row). No population oscillation was recovered when neurons were sorted
1303 according to their correlation values (second row), or according to different dimensionality reduction
1304 techniques (UMAP, Isomap, LEM, t-SNE). Each row of each raster plot shows the calcium activity of a
1305 single neuron, with activity plotted as a function of time, as in Fig 2a. Every dot indicates that one neuron
1306 was active at one specific time bin (bin size = 129 ms). Sequence scores and oscillation scores are
1307 presented in Fig 6c,d.

1308 **b,c.** Projection of the neural activity onto the low-dimensional embedding defined by the first two
1309 principal components obtained from applying PCA to the matrix of calcium activity of the PaS session
1310 (b) and the VIS session (c) shown in Fig. 6a. Bin size = 8.5 s. Note lack of obvious ring topology. Time is
1311 color-coded.

1312 **d.** Distribution of oscillation scores for the entire data set, as in Extended data Fig. 4c (19 VIS sessions,
1313 25 PaS sessions, 27 MEC sessions of which 15 were classified as oscillatory). Dashed line indicates
1314 threshold for classifying sessions as oscillatory with reference to the MEC data. Note that the bars for
1315 different brain regions sometimes overlap, and that bars are colored with transparency for visualization
1316 purposes (e.g. for sessions in PaS with oscillation score 0, the count is 24).

1317

1318 **Extended data Figure 10**

1319 **Population activity is less synchronized and more sequentially organized in PaS than VIS**

1320 **a.** Tuning of single cell calcium activity to ensemble activity expressed as the Pearson correlation
1321 between the calcium activity of each neuron and the activity of each ensemble, shown for the PaS (left,
1322 402 cells) and the VIS (right, 289 cells) example sessions presented in Fig. 6a. Each row is the tuning
1323 curve of one neuron, and neurons are sorted according to the PCA method. Color indicates Pearson
1324 correlation. Note that the VIS session exhibits a cluster of high correlation values for ensembles 5-10,
1325 which might indicate the presence of high co-activity in cells allocated to those ensembles.

1326 **b.** Cumulative distribution of the maximum Pearson correlation value between each cell's calcium
1327 activity and the ensemble activity. Data are for the same two example sessions as in (a). Note that VIS
1328 exhibits larger correlation between single-cell calcium activity and ensemble activity ($n = 6037$ VIS cells
1329 across 19 sessions, $n = 10868$ PaS cells across 25 sessions, $p = 1$, $D = 0.4179$, Kolmogorov Smirnov
1330 test).

1331 **c.** Probability that the ensemble a cell was assigned to based on the PCA sorting coincides with its most
1332 representative ensemble, calculated as the ensemble for which the Pearson correlation between the

1333 cell's calcium activity and ensemble activity is maximal. The probability is calculated as the fraction of
1334 cells in an individual session for which the PCA-assigned ensemble and the most representative
1335 ensemble coincide. In the box plot; all PaS sessions (n=25) and all visual cortex sessions (n=19) were
1336 pooled. For each session in each brain area the matrix of calcium activity was shuffled 500 times, next
1337 the PCA-assigned and most representative ensemble were calculated for each cell in the session and the
1338 probability that these coincide was computed over all cells and averaged across shuffle realizations per
1339 session. Ensemble activity was representative of cells' calcium activity in both brain areas (Wilcoxon
1340 rank-sum test comparing recorded and shuffled data for each brain area separately; PaS: $n = 25$
1341 sessions, $p = 1.42 \times 10^{-9}$, $Z = 6.05$; VIS: $n = 19$ sessions, $p = 1.48 \times 10^{-7}$, $Z = 5.25$), although this
1342 effect was more pronounced for VIS than for PaS neurons ($n = 25$ PaS sessions, 19 VIS sessions; $p =$
1343 0.0077 , $Z = 2.42$, one-tailed Wilcoxon rank-sum test; median VIS = 0.47, median PaS = 0.40). Symbols
1344 as in Fig. 3b.

1345 **d.** Based on the transition matrices calculated in Fig. 6h, we built directed weighted graphs as in
1346 Extended data Fig. 7p. Red edges indicate edges whose associated transition probability is higher than
1347 the 95th percentile of the transition probabilities obtained after temporally shuffling the data.

1348 **e.** Percentage of sessions with significant sequence score (MEC oscillatory sessions: 15 of 15, PaS: 7 of
1349 25; VIS: 1 of 19). The sequence score quantifies the probability of observing sequential activation of 3
1350 or more ensembles.

1351 **f.** Box plot of mean speed for sessions with and without significant sequence score. Mean speed was
1352 not different between these sessions ($n = 21$ sessions with significant sequence score and behavioural
1353 tracking synchronized to imaging: 13 MEC from which 10 were oscillatory + 7 PaS + 1 VIS; $n = 30$ sessions
1354 without significant sequence score and behavioural tracking synchronized to imaging: 1 MEC + 11 PaS +
1355 18 VIS; $p = 0.39$, $Z = 0.85$, Wilcoxon rank-sum test). Symbols as in Fig. 3b.

1356 **g.** Same as (f) but for total running distance ($p = 0.42$, $Z = 0.79$, Wilcoxon rank-sum test).

1357 **h.** Same as (f) but for fraction of the session with running behaviour ($p = 0.63$, $Z = 0.47$, Wilcoxon rank-
1358 sum test).

1359 **i.** Same as (f) but for the total amplitude of acceleration values, estimated as the maximum acceleration
1360 minus the minimum acceleration value observed in one session ($p = 0.1$, $Z = 1.62$, Wilcoxon rank-sum
1361 test).

1362 **j.** Normalized distribution of the Pearson correlation values (absolute value) between the activity of cell
1363 pairs in VIS (green) and in PaS (yellow). Each dot indicates the mean across sessions (25 PaS sessions, 19
1364 VIS sessions; all sessions in the data set were used, not only those with behavioural tracking
1365 synchronized to imaging), error bars indicate S.E.M. Probability is shown on a log-scale.

1366 **k.** Same as (j) but for the distribution of values of coactivity for all sessions recorded in PaS (yellow) and
1367 VIS (green). Coactivity was estimated for each session separately as the fraction of the recorded cells
1368 that was simultaneously active in 129 ms bins. Probability is shown on a log-scale.

1369

1370 **Movie 1**

1371 Motion corrected video of one oscillatory session (session 17) from animal #60584. Time in seconds in
1372 top left, scale bar is 50 microns. The video was obtained by sampling every 10th frame of the motion-
1373 corrected Suite2p output, and using a 3 frame moving average (inter-frame time ~ 310 ms). The video
1374 shows 10 consecutive sequences.

1375 **Methods:**

1376 All experiments were performed in accordance with the Norwegian Animal Welfare Act and the
1377 European Convention for the Protection of Vertebrate Animals used for Experimental and Other
1378 Scientific Purposes, Permit numbers 6021, 6008, and 7163.

1379 **Subjects**

1380 C57/Bl6 mice were housed in social groups of 2-6 individuals per cage, with access to nesting material
1381 and a planar running wheel. The mice were kept on a 12h light/12h darkness schedule in a temperature-
1382 and humidity-controlled vivarium. Food and water were provided ad libitum. The data were collected
1383 from a cohort of 12 animals (5 implanted in medial entorhinal cortex (MEC), 4 in parasubiculum (PaS), 3
1384 in visual cortex (VIS)).

1385 **Surgeries**

1386 Surgeries were performed according to a two-step protocol. During the first procedure, newborn pups
1387 or adult animals were injected in MEC/PaS or adult animals were injected in VIS with a virus carrying a
1388 construct for the expression of the calcium indicator GCaMP6m. The virus (for all injections: AAV1-Syn-
1389 GcaMP6m; titer: 3.43e13 GC/ml, Cat#AV-1-PV2823, UPenn Vector Core, University of Pennsylvania,
1390 USA) was diluted 1:1 in sterile DPBS (1X Dulbecco's Phosphate Buffered Saline, Gibco, ThermoFisher).
1391 During the second procedure, two weeks later, a microprism was implanted to gain optical access to
1392 infected neurons located in MEC and PaS, or a glass window was inserted to obtain similar access in VIS.

1393 For all surgeries, anesthesia was induced by placing the subjects in a plexiglass chamber filled with
1394 isoflurane vapor (5% isoflurane in medical air, flow of 1 l/min). Surgery was performed on a heated
1395 surgery table (38°C). Air flow was kept at 1 l/min with 1.5–3% isoflurane as determined from
1396 physiological monitoring of breathing and heartbeat. The mice were allowed to recover from surgery in
1397 a heated chamber (33°C) until they regained complete mobility and alertness.

1398 Virus Injection and microprism implantation in MEC and PaS

1399 In the first surgical procedure, newborn pups received injections of AAV1-Syn-GCaMP6m one day after
1400 birth⁹⁹. Analgesics were provided immediately before the surgery (Rymadil, Pfizer, 5 mg/kg). Pre-heated
1401 ultrasound gel (39°C, Aquasonic 100, Parker) was generously applied on the pup's head in order to
1402 create a large medium for the transmission of ultrasound waves. Real-time ultrasound imaging (Vevo
1403 1100 System, Fujifilm Visualsonics) allowed for targeted delivery of the viral mixture to specific areas of
1404 the brain. During ultrasound imaging, the pup was immobilized through a custom-made mouth adapter.
1405 The ultrasound probe (MS-550S) was lowered to be in close contact with the gel and hence the pup's
1406 head to allow visualization of the targeted structures. The probe was kept in place for the whole duration
1407 of the procedure via the VEVO injection mount (VEVO Imaging Station. Imaging in B-Mode, frequency:
1408 40 MHz; power: 100%; gain: 29 dB; dynamic range: 60 dB). Target regions were identified by structural
1409 landmarks: the MEC or PaS were identified in the antero-posterior and medio-lateral axis by the
1410 appearance of the aqueduct of Sylvius and the lateral sinus. The target area for injection was comparable
1411 to a coronal section at ~-4.7 mm from bregma in the adult animal. The solution containing the virus
1412 (250 ± 50 nl per injection) was injected in the target regions via beveled glass micropipettes (Origio,
1413 custom made; outer tip opening: 200 µm; inner tip opening: 50 µm) using a pressure-pulse system
1414 (Visualsonics, 5 pulses, 50 nl per pulse). The pipette tip was pushed through the brain without any
1415 incision on the skin, or craniotomy through the skull, and, to reduce the duration of the procedure,
1416 retracted immediately after depositing the virus in the target area. The anatomical specificity of the
1417 infection was verified by imaging serial sections of the infected hemispheres after experiment
1418 completion (see "Histology and reconstruction of field of view location").

1419 Two weeks after the viral injection, we performed a second procedure, in which a microprism was
1420 implanted to gain optical access to the superficial layers of MEC and PaS¹⁰⁰. The implanted microprism
1421 was a right-angle prism with 2 mm side length and reflective enhanced aluminum coating on the

1422 hypotenuse (Tower Optical). The prism was glued to a 4mm-diameter (CS-4R, thickness #1) round
1423 coverslip with UV curable adhesive (Norland). On the day of surgery, mice were anesthetized with
1424 isoflurane (IsoFlo, Zoetis, 5 % isoflurane vaporised in medical air delivered at 0.8-1 l/min) after which
1425 two analgesics were provided through intraperitoneal injection (Metacam, Boehringer Ingelheim, 5
1426 mg/kg or Rimadyl, Pfizer, 5 mg/kg, and Temgesic, Indivior, 0.05-0.1 mg/kg) and one local analgesic was
1427 applied underneath the skin covering the skull (Marcaïn, Aspen, 1-3 mg/kg). Their scalp was removed
1428 with surgical scissors and the surface of the bone was dried before being generously covered with
1429 optibond (Kerr). To increase the thickness and stability of the skull and overall preparation, a thin layer
1430 of dental cement (Charisma, Kulzer) was applied on the exposed skull, except in the location above the
1431 implant, where a 4 mm-wide circular craniotomy was made. The craniotomy was positioned over the
1432 dorsal surface of the cortex and cerebellum, with the center positioned ~ 4 mm lateral from the center
1433 of the medial sinus, and above the transverse sinus just above the MEC and PaS. After the dura was
1434 removed above the cerebellum, the lower edge of the prism was slowly pushed in the empty space
1435 between the forebrain and the cerebellum, just posterior to the transverse sinus. The edges of the
1436 coverslip were secured to the surrounding skull with UV-curable dental cement (Venus Diamond
1437 Flow, Kulzer). A custom-designed steel headbar was attached to the dorsal surface of the skull, centered
1438 upon and positioned parallel to the top face of the microprism. All exposed areas of the skull, including
1439 the headbar, were finally covered with dental cement (Paladur, Kulzer) and made opaque by adding
1440 carbon powder (Sigma Aldrich) until the dental cement powder became dark grey.

1441 Virus injection and glass window implantation in VIS

1442 In a different cohort of animals than those used for MEC/PaS imaging, we induced the expression of
1443 GCaMP6m in neurons of the adult VIS for subsequent imaging. We targeted the injection of the same
1444 AAV1-Syn-GCaMP6m viral solution used in the developing MEC and PaS to the primary visual cortex. On
1445 the day of surgery, 3-5 months old mice were anesthetized with isoflurane (IsoFlo, Zoetis, 5 % isoflurane
1446 vaporised in medical air delivered at 0.8-1 l/min) after which two analgesics were provided through
1447 intraperitoneal injection (Metacam, Boehringer Ingelheim, 5 mg/kg or Rimadyl, Pfizer, 5 mg/kg, and
1448 Temgesic, Indivior, 0.05-0.1 mg/kg) and one local anaesthetic was applied underneath the skin covering
1449 the skull (Marcaïn, Aspen, 1-3 mg/kg). The virus was injected at three locations in VIS, all of which were
1450 within the following anatomical ranges: 2.3-2.5 mm lateral from the midline, 0.9-1.3 mm anterior from
1451 lambda¹⁰¹. At each injection site, 50 nl of the virus was injected 0.5 mm below the dura and the pipette
1452 was left in place for 3-4 min to enable the virus to diffuse. The pipette was then brought to 0.3 mm
1453 below the dura and another 50 nl was injected. The pipette was then left in place for 5-10 min before
1454 retracting it completely. The speed of the injections was 5 nl/s.

1455
1456 Two weeks after the viral injection, a surgery to chronically implant a glass window on VIS was
1457 performed. The animals were handled as previously described for the prism surgery in MEC/PaS,
1458 including anesthesia, delivery of analgesics, and scalp removal. Optibond was applied to the exposed
1459 skull except in the location of the craniotomy. A 4 mm-wide craniotomy was made, centered on the
1460 virus injection coordinates, and a 4 mm glass window was placed underneath the skull edges of the
1461 craniotomy. The glass was slightly larger than the craniotomy, so after it was maneuvered in place, the
1462 upward pressure exerted by the brain secured it in place against the skull, thereby minimizing the
1463 presence of empty gaps that might favor tissue and bone regrowth. The edges of the window were
1464 secured with UV-curable dental cement and superglue before the positioning of the headbar as
1465 described for the MEC-PaS implantation. All exposed areas of the skull, including the headbar, were
1466 finally covered with dental cement (Paladur, Kulzer) that was made opaque by adding carbon powder
1467 (Sigma Aldrich) until the dental cement powder became dark grey.

1468 **Self-paced running behavior under sensory-minimized conditions**

1469 Training of animals began 2 days after the prism implantation in MEC and PaS, and 12 days after the
1470 implantation of a cranial window in VIS. Mice were head-restrained by a headbar with their limbs resting

1471 on a freely rotating styrofoam wheel with a metal shaft fixed through the center. The radius of the wheel
1472 was ~85 mm and the width 70 mm. Low friction ball bearings (HK 0608, Kulelager AS, Molde, NO) were
1473 affixed to the ends of the metal shaft and held in place on the optical table using a custom mount. This
1474 arrangement allowed the mice to self-regulate their movement. The position of the animal on the
1475 rotating wheel was measured using a rotary encoder (E6B2-CWZ3E, YUMO) attached to its center axis.
1476 Step values of the encoder (4096 per full revolution, ~130 μm resolution) were digitized by a
1477 microcontroller (Teensy 3.5, PJRC) and recorded using custom python scripts at 40-50 Hz. Wheel tracking
1478 was triggered at the start of imaging and synchronized to the ongoing image acquisition through a digital
1479 input from the 2-photon microscope. In a subset of mice (3 out of 12; 2 implanted in MEC, 1 implanted
1480 in PaS), the precise synchronization was not available to us and these data were hence not used for
1481 comparison of movement and imaging data. A T-slot photo interrupter (EE-SX672, Omron) served as a
1482 lap (full-revolution) counter. Design and code of the wheel are publicly available under
1483 https://github.com/kavli-ntnu/wheel_tracker.

1484 The self-paced task was performed under conditions of minimal sensory stimulation, in darkness, and
1485 with no rewards to signal elapsed time or distance run^{36,37}. Prior to the imaging sessions, mice were
1486 accustomed to the setup through daily exposures over the course of two weeks (i.e., 15 sessions over
1487 15 days, one session per day). In each session, after the mice were positioned on the wheel, they were
1488 gently head-restrained and free to run or rest for 30 or 60 min.

1489 **2-photon imaging in head-fixed animals**

1490 A custom-built 2-photon benchtop microscope (Femtonics, Hungary) was used for 2-photon imaging of
1491 the target areas (i.e., superficial layers of MEC, PaS, and VIS). A Ti:Sapphire laser (MaiTai Deepsee eHP
1492 DS, Spectra-Physics) tuned to a wavelength of 920 nm was used as the excitation source. Average laser
1493 power at the sample (after the objective) was 50–120 mW. Emitted GCaMP6m fluorescence was routed
1494 to a GaAsP detector through a 600 nm dichroic beamsplitter plate and 490-550 nm band-pass filter.
1495 Light was transmitted through a 16x/0.8NA water-immersion objective (Cat#MRP07220, Nikon)
1496 carefully lowered in close contact to the coverslip glued to the microprism (for MEC-PaS imaging) or
1497 above the coverslip in contact with the brain surface (for VIS imaging). For the microprism-implanted
1498 animals, the objective lens was aligned to the ventrolateral corner of the prism, to consistently identify
1499 the position of MEC and PaS across animals. Ultrasound gel (Aquasonic 100, Parker) or water was used
1500 to fill the gap between the objective lens and the glass coverslips. The software MESc (v 3.3 and 3.5,
1501 Femtonics, Hungary) was used for microscope control and data acquisition. Imaging time series of either
1502 ~30 min or ~60 min were acquired at 512x512 pixels (sampling frequency: 30.95 Hz, frame duration:
1503 ~32 ms; pixel size: either 1.78x1.78 μm^2 or 1.18x1.18 μm^2). Time series acquisition was initiated
1504 arbitrarily after the animal was head-restrained on the setup.

1505 **Histology and reconstruction of field-of-view location**

1506 On the last day of imaging, after the imaging session, the mice were anesthetized with isoflurane (IsoFlo,
1507 Zoetis) and then received an overdose of sodium pentobarbital before transcardial perfusion with
1508 freshly prepared PFA (4% in PBS). After perfusion, the brain was extracted from the skull and kept in 4%
1509 PFA overnight for post-fixation. The PFA was exchanged with 30% sucrose to cryoprotect the tissue.

1510 To verify the anatomical location of the imaged field of views (FOVs) in the microprism implanted
1511 animals, we used small, custom-made pins, derived from a thin piano wire coated with a solution of 1,1'-
1512 Dioctadecyl-3,3',3',3'-Tetramethylindocarbocyanine Perchlorate ('Dil'; DiI18(3)) (commercial name: Dil,
1513 ThermoFischer), to mark the location of the imaged tissue in relation to the prism footprint. A Dil-coated
1514 pin was inserted into the brain tissue at the location left empty by the prism footprint, and specifically
1515 targeted to the ventro-lateral corner of the footprint (see "Surgeries"). The pin was left in place to favor
1516 transfer of Dil from the metal pin to the brain tissue, and to leave a fluorescent mark on the location of
1517 the imaged FOV. After 30 to 60 seconds, the pin was removed and the brain was sliced on a cryostat in
1518 30-50 μm thick sagittal sections. All slices were collected sequentially in a 24-well plate filled with PBS,
1519 before being mounted in their appropriate anatomical order on a glass slide in custom-made mounting

1520 medium. For confocal imaging, a Zeiss LSM 880 microscope (Carl Zeiss, Germany) was used to scan
1521 through the whole series of slices and locate the position of the Dil fluorescent mark. Images were then
1522 acquired using an EC Plan-Neofluar 20×/0.8 NA air immersion, 40×/1.3 oil immersion, or 63×/1.4 oil
1523 immersion objective (Zeiss, laser power: 2-15%; optical slice: 1.28–1.35 airy units, step size: 2 μm).
1524 Before acquisition, gain and digital offset were established to optimize the dynamic range of acquisition
1525 to the dynamic range of the GCaMP6m and Dil signals. Settings were kept constant during acquisition
1526 across brains. Based on the location of the red fluorescent mark, we could infer where, on the medio-
1527 lateral and dorso-ventral extent of the brain, the ventro-lateral corner of the microprism (and hence the
1528 2-photon FOV aligned to it) was located.

1529 We used the Paxinos mouse brain atlas¹⁰¹ to produce a reference flat map representing the medio-
1530 lateral and dorso-ventral extent of the MEC and PaS. Flat maps helped delineate the extent of the FOV
1531 that fell within the anatomical boundaries of either the MEC and adjacent PaS, and allowed for a
1532 standardized comparison across animals. For each imaged animal, we mapped the dorsoventral and
1533 mediolateral location of the Dil mark on the reference flat map (Extended data Fig. 1c). Animals were
1534 assigned to “MEC Imaging” or “PaS imaging” groups depending on the location of the FOV: a mouse
1535 would be further analysed as being part of the “MEC imaging” group if more than 50% of the area of the
1536 FOV occupied by GCaMP6m+ cells could be located in the MEC.

1537 To verify the anatomical location of the FOVs in VIS in the glass-window implanted mice, we sliced the
1538 brain until we reached the anatomical coordinates at which the virus was infused (see “Surgeries”).
1539 Coronally cut slices of 50 μm thickness were collected sequentially in a 24 well plate, and immediately
1540 mounted in their appropriate anatomical order on a glass slide in custom-made mounting medium. For
1541 confocal imaging, a Zeiss LSM 880 microscope (Carl Zeiss, Germany) was used according to the same
1542 specification as described above for MEC/PaS.

1543 **Analysis of imaging timeseries**

1544 Imaging timeseries data was analyzed using the Suite2p³⁹ python library
1545 (<https://github.com/MouseLand/suite2p>). We used its built-in routines for motion correction, region of
1546 interests (ROI) extraction, neuropil signal estimation, and spike deconvolution. Non-rigid motion
1547 correction was chosen to align each frame iteratively to a template. Quality was assessed by visual
1548 inspection of the corrected stacks and built-in motion correction metrics. The Suite2p GUI was used to
1549 manually sub-select putative neurons based on anatomical and signal characteristics and to discard
1550 obvious artefacts that accumulated during the analysis, e.g., ROIs with footprints spanning large areas
1551 of the FOV, ROIs that did not have clearly delineated circumferences in the generated maximum
1552 intensity projection, or ROIs that were extracted automatically but showed no visible calcium transients.

1553 Raw fluorescence calcium traces of each ROI were neuropil-corrected to create a fluorescence calcium
1554 signal “ F_{corr} ” by subtracting 0.7 times the neuropil signal from the raw fluorescence traces. We used the
1555 Suite2p integrated version of non-negative deconvolution³⁸ with $\tau=1$ s to deconvolve F_{corr} , yielding the
1556 basis for the binarized sequences that we refer to as the calcium activity (see section below “Binary
1557 deconvolved calcium activity and matrix of calcium activity”). To estimate the signal-to-noise-ratio (SNR)
1558 of each cell, we further thresholded the calcium activity (without binarization) at 1 standard deviation
1559 over the mean, yielding filtered calcium activity, and classified the remaining activity as noise. We
1560 additionally ensured that noise was temporally well segregated from filtered calcium activity by
1561 requiring datapoints classified as noise to be separated by at least one second before and ten seconds
1562 after filtered calcium activity. The SNR of the cell was then estimated as the ratio of the mean amplitude
1563 of F_{corr} during episodes of filtered calcium activity over the standard deviation of F_{corr} during episodes of
1564 noise. If no datapoints remained after the filtering of calcium activity, the cell was assigned a SNR of
1565 zero.

1566

1567

1568 **Binary deconvolved calcium activity and matrix of calcium activity**

1569 In order to denoise the recorded fluorescence calcium signals and have good temporal resolution all
1570 analyses in the study were performed using the deconvolved calcium activity of the recorded cells. For
1571 each cell whose SNR was larger than 4, the deconvolved calcium activity (see “Analysis of imaging
1572 timeseries”) was downsampled by a factor of 4 by calculating the mean over time windows of ~129 ms
1573 (original sampling frequency = 30.95 Hz, sampling frequency used in the analyses = 7.73 Hz). Next, this
1574 signal was averaged over time and its standard deviation was calculated. A threshold equal to this
1575 average plus 1.5 times the standard deviation was used to convert the deconvolved calcium activity into
1576 a binary deconvolved calcium activity, such that all values above the threshold were set to 1 (“calcium
1577 events”), and all values below or equal to that threshold were set to 0. Unless stated otherwise, for all
1578 analyses throughout the study we used the deconvolved and binary calcium activity, to which for
1579 simplicity we refer to as “deconvolved calcium activity” or simply “calcium activity”. The calcium activity
1580 of all cells in a session with SNR > 4 was stacked to construct a binary “matrix of calcium activity” which
1581 had as many rows as neurons, and as many columns as time bins sampled at 7.73 Hz. The *population*
1582 *vectors* are the columns of the matrix of calcium activity.

1583 **Autocorrelations and spectral analysis of single cell calcium activity**

1584 To determine if the calcium activity of single cells displays ultraslow oscillations, for each neuron the
1585 power spectral density (PSD) was calculated on the autocorrelation of its calcium activity. The PSD was
1586 computed using Welch's method (“pwelch”, built-in Matlab function), with Hamming windows of 17.6
1587 min (8192 bins of 129 ms in each window) and 50% of overlap between consecutive windows. Note that
1588 when calculating the PSD a large window was needed to identify oscillation frequencies $\ll 0.1$ Hz.

1589 To visualize whether specific oscillatory patterns at fixed frequencies were present in the neural
1590 population, all autocorrelations from one session were sorted and stacked into a matrix, where rows
1591 are cells and columns are time lags. The sorting of autocorrelations was performed either (1) according
1592 to the maximum power of each PSD in a descending manner, or (2) according to the frequency at which
1593 each PSD peaked, in a descending manner. The frequency at which the PSD peaked was used as an
1594 estimate of the oscillatory frequency of the cell's calcium activity.

1595 **Correlation and PCA sorting methods**

1596 To determine whether neural population activity exhibits temporal structure we visualized the
1597 population activity by means of raster plots in which we sorted all cells according to different methods.

1598 Correlation method: This method sorts cells such that those that are nearby in the sorting are more
1599 synchronized than those that are further away. First, each calcium activity was downsampled by a factor
1600 4 by calculating the mean over counts of calcium events in bins of 0.52 s. The obtained calcium activity
1601 was then smoothed by convolving it with a gaussian kernel of width equal to four times the oscillation
1602 bin size, a bin size that was representative of the temporal scale of the population dynamics (see
1603 “Oscillation bin size”). The cross correlations between all pairs of cells were calculated using time bins
1604 as data points, and a maximum time lag of 10 time points, equivalent to ~5 s. This small time lag allowed
1605 us to identify near instantaneous correlation while keeping information about the temporal order of
1606 activity between cell pairs. The maximum value of the cross correlation between cell i and cell j was
1607 stored in the entry (i, j) of the correlation matrix C , which was a square matrix of N rows and N columns,
1608 where N was the total number of recorded neurons in the session with SNR > 4. If the cross correlation
1609 peaked at a negative time lag the value in the entry (i, j) was multiplied by -1. The entry with the highest
1610 cross correlation value was identified and its row, denoted by i_{max} , was used as the lead cell for the
1611 sorting procedure and chosen to be the first cell in the sorting. Cells were then sorted according to the

1612 values in the entries (i_{max}, j) , $j = 1, 2, \dots, N, j \neq i_{max}$, i.e. their correlations with the lead cell, in a
1613 descending manner.

1614 PCA method: Computing correlations from the calcium activity or the calcium signals can be noisy due
1615 to variability in the frequency of the calcium events and fine tuning of hyperparameters (e.g. the size of
1616 the kernel used to smooth the calcium activity of all cells). To avoid this, we leveraged the fact that the
1617 periodic sequences of neural activity in the population oscillation constitute low dimensional dynamics
1618 with intrinsic dimensionality equal to 1, and sorted the cells based on an unsupervised dimensionality
1619 reduction approach (a similar approach was used in ref. 102). For each recording session, principal
1620 component analysis (PCA) was applied to the matrix of calcium activity (bin size = 129 ms; using Matlab's
1621 built-in function "pca"), including all epochs of movement and immobility and using the rows (neurons)
1622 as variables and the columns (population vectors) as observations. The first two principal components
1623 (PCs) were kept, since two is the minimum number of components needed to embed non-linear 1-
1624 dimensional dynamics. Cells were sorted according to their loadings in PC1 and PC2, expecting that the
1625 relationship between these loadings would express the ordering in cell activation during the sequences.

1626 The plane spanned by PC1 and PC2 was named the PC1-PC2 plane. In the PC1-PC2 plane, the loadings
1627 of each neuron (the components of the eigenvectors without being multiplied by the eigenvalues)
1628 defined a vector, for which we computed its angle $\theta_i = \arctg\left(\frac{l_{PC2}^i}{l_{PC1}^i}\right) \in [-\pi, \pi]$, $1 \leq i \leq N$, with respect
1629 to the axis of PC1, where l_{PCj}^i is the loading of cell i on PCj . Cells were sorted according to their angle θ
1630 in a descending manner.

1631 Note that while we keep the first 2 PCs to sort the neurons, all PCs and the full matrices of calcium
1632 activity were used in the analyses (except for visualization purposes, e.g. see "Manifold visualization for
1633 MEC sessions"). Finally, note that because in PCA a PC is equivalent to -1 times the PC, the sorting and
1634 an inversion of the sorting are equivalent. The sorting was chosen so that sequences would progress
1635 from the bottom to the top in the raster plot.

1636 The PCA method was used throughout the paper for sorting the recorded cells unless otherwise stated.

1637 Random sorting of cell identities: A random ordinal integer $\in [1, N]$, where N is the total number of
1638 recorded cells with $SNR > 4$, was assigned to each neuron without repetition across cells. Neurons were
1639 sorted according to those assigned numbers.

1640 Sorting of temporally shuffled data: A shuffled matrix of calcium activity was built by temporally shuffling
1641 the calcium activity of each cell separately. For each cell, each time bin of the calcium activity was
1642 assigned a random ordinal integer $\in [1, T]$ without repetition across time bins, where T is the total
1643 number of time bins (bin size = 129 ms), and time bins were ordered according to their assigned number.
1644 The assignment of random ordinal integers was made separately for each cell, so that the obtained
1645 random orderings were not shared across cells. The PCA method was then applied to the shuffled matrix
1646 of calcium activity.

1647 **Sorting methods based on non-linear dimensionality reduction techniques**

1648 The PCA method for sorting cells relies on a two-dimensional linear embedding. This linear embedding
1649 might not be optimal if the population vectors describe temporal trajectories that, despite being low-
1650 dimensional, lie on a curved surface. To take into account potential non-linearities, four additional
1651 sorting methods were implemented, based on the following non-linear dimensionality reduction
1652 techniques¹⁰³: t-SNE, Laplacian Eigenmaps (LEM), Isomap, and UMAP¹⁰⁴ (see parameters below). First,
1653 to express in the sortings the ordering of the cells during the slow temporal progression of the
1654 sequences, the four methods used a resampled matrix of calcium activity as input. To compute this
1655 matrix, for each session, we downsampled each calcium activity by a factor 4 by calculating its mean in

1656 bins of 0.52 s. The calcium activity of all cells was then smoothed by convolving them with a gaussian
1657 kernel whose width was given by the oscillation bin size (see “Oscillation bin size”). After applying t-SNE,
1658 LEM, Isomap or UMAP to the resampled matrix of calcium activity, we kept the first two dimensions
1659 obtained with each method, for the same reasons as presented for the PCA sorting method. To obtain
1660 the sorting, the following procedure was applied: We let Dim1 and Dim2 be the first two dimensions
1661 obtained with the chosen dimensionality reduction technique that we had applied to the resampled
1662 matrix. In analogy with the PCA method, the Dim1-Dim2 plane was spanned by Dim1 and Dim2 and for
1663 each cell the components on those dimensions defined a vector in this plane for which the angle $\theta \in$
1664 $[-\pi, \pi)$ with respect to the axis of Dim1 was computed. Cells were then sorted according to their angles
1665 in a descending manner.

1666 To apply t-SNE to the population activity we used a perplexity value of 50. First, we applied PCA to the
1667 resampled matrix of calcium activity, and then we used the projection of the neural activity onto the
1668 first 50 principal components as input to t-SNE. To apply LEM to the population activity, we used as
1669 hyperparameters $k=15$ and $\sigma=2$. Similarly, we used $k=15$ for running isomap. Finally, we used
1670 $n_neighbors=30$, $min_dist=0.3$ and correlation as metric for running UMAP.

1671 We used the MATLAB implementation of UMAP¹⁰⁵ and the Matlab Toolbox for Dimensionality Reduction
1672 (<https://lvdmaaten.github.io/drtoolbox/>). Finally, when displaying the raster plots that resulted from
1673 the different sortings, the first cell (located at the bottom of the raster plot) was always the same. This
1674 was accomplished by circularly shifting the cells in the different sortings such that the initial cell in all
1675 sortings coincided with the initial cell of the sorting obtained with the PCA method.

1676 **Manifold visualization for MEC sessions**

1677 Sorting the cells and visualizing their combined neural activity through raster plots revealed the
1678 presence of oscillatory sequences of neural activity in the recorded data. To visualize the topology of
1679 the manifold underlying the oscillatory sequences of activity, both PCA and LEM were used.

1680 PCA was applied to the matrix of calcium activity, which first had each row convolved with a gaussian
1681 kernel of width equal to 4 times the oscillation bin size (see “Oscillation bin size”). The manifold was
1682 visualized by plotting the neural activity projected onto the embedding defined by PC1 and PC2. In Fig.
1683 2d (left) the neural activity of the entire session was projected onto the low-dimensional embedding. In
1684 Extended data Fig. 3d the neural activity corresponding to the concatenated epochs of uninterrupted
1685 population oscillation was projected onto the embedding.

1686 For the LEM approach, first PCA was applied to the matrix of calcium activity, which was previously
1687 resampled to bins of 0.52 s as in “Sorting methods based on non-linear dimensionality reduction
1688 techniques”, and the first 5 principal components were kept. Next LEM was applied to the matrix
1689 composed of the 5 PCs, using as parameters $k=15$ and $\sigma=2$. We decided to keep 5 PCs prior to applying
1690 LEM to denoise the data, for which we leveraged the fact that sequences of activity constitute low-
1691 dimensional dynamics with intrinsic dimensionality equal to 1, and therefore truncating the data to the
1692 first 5 PCs should preserve the sequential activity. The manifold was visualized by plotting the neural
1693 activity projected onto the embedding defined by the first two LEM dimensions. In Fig. 2d (right) the
1694 neural activity of the entire session was projected onto the embedding.

1695 Both approaches revealed a ring-shaped manifold along which the population activity propagated
1696 repeatedly with periodic boundary conditions. One “cycle” of the population oscillation was defined as
1697 one full turn of the population activity along the ring-shaped manifold.

1698

1699

1700 Phase of the oscillation

1701 To track the progression of the population activity over time, we leveraged the low dimensionality of
1702 the ring-shaped manifold and the circular nature of the population activity, and parametrized the
1703 population activity with a single time-dependent parameter, which we called the “phase of the
1704 oscillation”. Hence, the phase of the oscillation varied as a function of time (bin size = 129 ms) and
1705 tracked the progression of the neural activity during the population oscillation. The neural activity was
1706 projected onto a two-dimensional plane using PCA. The use of PCA avoided the selection of
1707 hyperparameters, which is required in all non-linear dimensionality reduction techniques including LEM.
1708 Let $PCi_t(t)$ be the projection of the neural population activity onto Principal Component i (PC i). The
1709 neural population activity at time point t projected onto the plane defined by PC1 and PC2 is then given
1710 by $(PC1_t(t), PC2_t(t))$, which defines a vector in this plane. The phase of the oscillation is defined as the
1711 angle of this vector with respect to the PC1 axis and is given by

$$1712 \quad \varphi(t) = \arctg\left(\frac{PC2_t(t)}{PC1_t(t)}\right). \quad (\text{Equation 1})$$

1713 During one cycle of the population oscillation, the phase of the oscillation continuously traversed the
1714 range $[-\pi, \pi)$, which was consistent with the population activity propagating through the network and
1715 describing one turn along the ring-shaped manifold.

1716 Joint distribution of cross correlation time lag and angular distance in the PCA sorting

1717 To further characterize the sequential activation in the MEC neural population and to introduce a score
1718 that would determine the extent to which a session exhibited population oscillations (see “Oscillation
1719 score”), we determined the relationship between the time lags that maximized the cross correlation
1720 between the calcium activity of two cells (τ) and their angular distances in the PCA sorting (d). In the
1721 plane generated by PC1 and PC2, the loadings of each neuron defined a vector, for which we computed
1722 the angle $\theta_i = \arctg\left(\frac{l_{PC2}^i}{l_{PC1}^i}\right) \in [-\pi, \pi)$, $1 \leq i \leq N$, with respect to the axis of PC1, where l_{PCj}^i is the
1723 loading of cell i on PC j and N is the total number of recorded neurons (see “Correlation and PCA sorting
1724 methods”). The angular distance d between any two cells in the PCA sorting was calculated as the
1725 difference between their angles wrapped in the interval $[-\pi, \pi)$ (see Fig. 2f left),

$$1726 \quad d_{i,j} = (\theta_i - \theta_j), \quad (\text{Equation 2})$$

1727 where $1 \leq i \leq N, 1 \leq j \leq N$. The Matlab function “angdiff” was used for computing this distance. Note
1728 that the angular distance maps how far apart two cells are in the raster plot when cells are sorted
1729 according to the PCA method.

1730 To estimate the joint distribution of cross correlation time lags and angular distances in the PCA sorting,
1731 the cross correlations between all pairs of cells were calculated using a maximum time lag of 248 s. For
1732 each cell pair the time lag at which the cross correlation peaked (τ) and the angular distance in the PCA
1733 sorting (d) were calculated. A discrete representation was used for these two variables: in all analyses,
1734 and unless stated otherwise, the range of possible τ values, i.e. $[-248, 248]$ s, was discretized into 96 bins
1735 of size $\Delta\tau = \frac{496 \text{ s}}{96} \sim 5 \text{ s}$ and the range of possible d values, i.e. $[-\pi, \pi)$ rad, was discretized into 11 bins of
1736 size $\Delta d = \frac{2\pi}{11} \sim 0.57 \text{ rad}$. Using those bins, the joint distribution of τ and d was expressed as a 2D
1737 histogram that counted the number of cell pairs observed for every combination of τ bins and d bins,
1738 normalized by the total number of cell pairs.

1739

1740

1741 Oscillation score

1742 While striking population oscillations were observed in multiple sessions and animals, the population
1743 activity exhibited considerable variability, ranging from non-patterned activity to highly stereotypic and
1744 periodic sequences (Extended data Fig. 4a). This variability prompted us to quantify, for each session,
1745 the extent to which the population activity was oscillatory, which we did by computing an oscillation
1746 score. For each session, we first calculated the phase of the oscillation $\varphi(t)$ (bin size = 129 ms, Equation
1747 1), which tracks the progression of the population activity in the presence of population oscillations (see
1748 “Phase of the oscillation” and Fig. 2e). Next the PSD of $\sin(\varphi(t))$ was calculated using Welch’s method
1749 with Hamming windows of 17.6 min (8192 bins of 129 ms in each window) and 50% of overlap between
1750 consecutive windows (“pwelch” Matlab function, see “Autocorrelations and spectral analysis of single
1751 cell calcium activity”). If the PSD peaked at 0 Hz and the PSD was strictly decreasing, the phase of the
1752 oscillation was not oscillatory and hence the population activity was not periodic in the analysed session.
1753 In this case the oscillation score was set to zero. Otherwise, prominent peaks in the PSD at a frequency
1754 larger than 0 Hz were identified. In order to disentangle large-amplitude peaks from small fluctuations
1755 in the PSD, a peak at frequency f_{max} was considered prominent and indicative of periodic activity if its
1756 amplitude was larger than (i) 9 times the mean of the tail of the PSD (i.e. $\langle \text{PSD}(f > f_{max}) \rangle$, where $\langle \rangle$
1757 indicates the average over frequencies) and (ii) 9 times the minimum of the PSD between 0 Hz and f_{max}
1758 (i.e. $\min(\text{PSD}(f < f_{max}))$). If no peak in the PSD met these criteria the oscillation score was set to zero.
1759 Otherwise, the presence of a prominent peak in the PSD calculated on $\sin(\varphi(t))$ was considered
1760 indicative of periodic activity at the population level. Yet a crucial component for observing oscillatory
1761 sequences is that cells fire periodically and that the time lag that maximizes the cross correlations
1762 between the calcium activity of pairs of cells that are located at a fixed distance in the sequence comes
1763 in integer multiples of a minimum time lag, which ensures that cells oscillate at a fixed frequency and
1764 that the calcium activity of one cell is temporally shifted with respect to the other. To quantify the extent
1765 to which these features were present in the data, we computed the joint distribution of time lags and
1766 angular distance in the PCA sorting (τ was discretized into 240 bins and d was discretized into 11 bins,
1767 see “Joint distribution of cross correlation time lag and angular distance in the PCA sorting”). Next for
1768 each bin i of d , $1 \leq i \leq 11$, we calculated the PSD of the distribution of τ conditioned on the distance
1769 bin i (Welch’s methods, Hamming windows of 128 τ bins with 50% overlap between consecutive
1770 windows, “pwelch” Matlab function). The presence of a peak in this signal indicated that for bin i of d ,
1771 the time lag that maximizes the cross correlations between cells was oscillatory (i.e. it peaked at
1772 multiples of one specific time lag), as expected when cells are active periodically with an approximately
1773 fixed frequency and also with harmonics of the primary frequency. The presence (or absence) of a peak
1774 that satisfied the condition of being larger than (i) 10 times the mean of the tail of the PSD (same
1775 definition as above), and (ii) 4.5 times larger than the minimum between 0 Hz and the frequency at
1776 which the PSD peaked, was identified (same definition as above, the parameters are different from the
1777 ones used above because the signals are very different). The oscillation score was then calculated as the
1778 fraction of angular distance bins for which a peak was identified.

1779 Based on the bimodal distribution of oscillation scores obtained in the MEC data (Extended data Fig. 4c),
1780 a session was considered to express population oscillations if the oscillation score was ≥ 0.72 , which was
1781 equivalent to asking that at least 8 out of the 11 distributions of τ conditioned on bin i of d , $1 \leq i \leq$
1782 11 , had a significant peak in their PSD. This choice of cut-off also accounted for the fact that for distances
1783 in the PCA sorting that are close to zero, cells exhibit instantaneous coactivity rather than coactivity
1784 shifted by some specific time lag, which makes the conditional probability not oscillatory. After applying
1785 the cut-off, 15 of 27 MEC sessions in 5 animals were classified as oscillatory (Extended data Fig. 4c), and
1786 among those 15 sessions, 10 were recorded with synchronized behavioural tracking (see “Self-paced
1787 running behavior under sensory-minimized conditions”). The number of recorded cells in the oscillatory

1788 sessions ranged from 207 to 520. In the rest of the data set, 0 of 25 PaS sessions in 4 animals were
1789 classified as oscillatory, 0 of 19 VIS sessions in 3 animals were classified as oscillatory.

1790 **Oscillation bin size**

1791 The population oscillation progressed at frequencies < 0.1 Hz that varied from session to session. The
1792 “oscillation bin size” was a temporal bin size representative of the time scale of the population
1793 oscillation in each session. It was used to quantify single cell and neural population dynamics, for which
1794 describing the neural activity at the right time scale was fundamental (e.g. see “Transition probabilities
1795 and graph representation”). For each oscillatory session the period of the population oscillation,
1796 denoted by P_{osc} , was calculated as the inverse of the frequency f_{max} at which the PSD of the signal
1797 $\sin(\varphi(t))$ peaked (see Equation 1 and “Oscillation score”), i.e. $P_{osc} = f_{max}^{-1}$. Note that this estimate
1798 of the period was reliable when during most of the session the network engaged in the population
1799 oscillation, in which case the estimate was equivalent to the length of the session divided by the total
1800 number of oscillation cycles. However, it became less reliable the more interrupted the population
1801 oscillation was.

1802 The oscillation bin size T_{osc} was computed as the period of the population oscillation divided by 10,

$$1803 \quad T_{osc} = \frac{P_{osc}}{10} = \frac{1}{10 \cdot f_{max}}. \quad (\text{Equation 3})$$

1804 This choice of bin size was made so that each cycle of the population oscillation would progress across
1805 ~ 10 time points. Across 15 oscillatory sessions, the oscillation bin size ranged from 3 to 17 s (see
1806 Extended data Fig. 7).

1807 In sessions without population oscillations, there was not a well-defined peak in the PSD of $\sin(\varphi(t))$,
1808 and therefore the oscillation bin size was not possible or meaningful to calculate. Yet, to perform the
1809 quantifications of network dynamics at temporal scales similar to the ones investigated in oscillatory
1810 sessions, the mean oscillation bin size computed across all oscillatory sessions was used (mean
1811 oscillation bin size = 8.5 s).

1812 Unless otherwise indicated, the utilized bin size was 129 ms.

1813 **Identification of individual oscillation cycles**

1814 The characterization of the population oscillation required multiple analyses that relied on identifying
1815 individual cycles, for example to quantify the length of the cycles and their variability. The procedure for
1816 identifying individual cycles was based on finding the time points at which each cycle began (visualized
1817 typically at the bottom of the raster plot) and ended (visualized typically at the top of the raster plot,
1818 see Extended data Fig. 5a). Note that the beginning and the end of the cycle are arbitrary because of the
1819 periodic boundary conditions in the cycle progression, and therefore a different pair of phases that are
1820 2π apart could have been used for defining the beginning and the end of the cycle.

1821 One cycle was defined as one full turn of the phase of the oscillation (see “Phase of the oscillation”), i.e.
1822 during one cycle the phase of the oscillation traversed 2π . To calculate the phase of the oscillation and
1823 determine the time epochs during which it traversed 2π , we smoothed the calcium activity of all cells
1824 (bin size = 129 ms) using a gaussian kernel of width equal to the oscillation bin size. Next, the phase of
1825 the oscillation was calculated and discretized into 10 bins (i.e. the range $[-\pi, \pi]$ was discretized into 10
1826 bins). Time points at which the phase of the oscillation belonged to a bin that was 3 or more bins away
1827 from the bin in the previous time point were considered as discontinuity points and were used to define
1828 the beginning and the end of putative cycles. Putative cycles were classified as cycles if the phase of the
1829 oscillation smoothly traversed the range $[-\pi, \pi]$ rad in an ascending manner. To account for variability,
1830 decrements of up to 1 bin of the phase of the oscillation were allowed. Points of sustained activity were

1831 disregarded. Segments of cycles in which the phase of the oscillation covered at least 5 bins (i.e. 50% or
1832 more of the range $[-\pi, \pi)$ rad) were also identified.

1833 **Cycle length, population oscillation frequency and inter-cycle interval**

1834 The length of individual cycles (cycle length) was defined as the amount of time that it takes the phase
1835 of the oscillation to cover the range $[-\pi, \pi)$ in a smooth and increasing manner, which is consistent with
1836 the population activity completing one full turn along the ring-shaped manifold. To calculate the cycle
1837 length, the time interval between the beginning and the end of the cycle was determined (see
1838 “Identification of individual oscillation cycles”).

1839 To quantify the variability in cycle length within and between sessions, two approaches were adopted.
1840 In approach 1 (Extended data Fig. 5e left), the standard deviation of cycle lengths was computed for
1841 each oscillatory session. To estimate significance, in each of 500 iterations all cycles across 15 oscillatory
1842 sessions were pooled (421 cycles in total) and randomly assigned to each session while keeping the
1843 original number of cycles per session unchanged. For each iteration the standard deviation of the cycle
1844 lengths randomly assigned to each session was calculated. In approach 2 (Extended data Fig. 5e right),
1845 for each session $i, 1 \leq i \leq 15$, where 15 is the total number of oscillatory sessions, we considered all
1846 pairs of cycles within session i (“within session” group) or alternatively all pairs of cycles such that one
1847 cycle belongs to session i and the other cycle to session $j, j \neq i$ (“between session” group). For each
1848 cycle pair in each group, the ratio between the shortest cycle length and the longest cycle length was
1849 calculated. The mean was computed over pairs of cycles in each group for each session separately.
1850 Notice that the larger this ratio the more similar are the cycle lengths.

1851 The frequency of the population oscillation was calculated as the total number of identified individual
1852 cycles in a session, divided by the total amount of time the network engaged in the population oscillation
1853 during the session, which was computed as the length of the temporal window of concatenated cycles.

1854 The inter-cycle interval was defined as the length of the epoch from the termination of one cycle and
1855 the beginning of the next one.

1856 **Mean event rate during segments of the oscillation cycle**

1857 To determine how population activity varied during individual cycles of the population oscillation
1858 (Extended data Fig. 5c), the following approach was adopted. For each oscillatory session (see
1859 “Oscillation score”) all individual cycles were identified (see “Identification of individual oscillation
1860 cycles”). Each cycle was divided into 10 segments of equal length. For each cycle segment, the mean
1861 event rate was calculated as the total number of calcium events across cells divided by cycle segment
1862 duration and number of cells. For each session the mean event rate per segment was calculated over
1863 cycles.

1864 **Locking to the phase of the oscillation**

1865 To calculate the extent to which individual cells were tuned to the population oscillation, two quantities
1866 were used: the locking degree and the mutual information between the calcium event counts and the
1867 phase of the oscillation. For each oscillatory session, the phase of the oscillation $\varphi(t)$ was computed
1868 (see Equation 1) and individual cycles were identified (see “Identification of individual oscillation
1869 cycles”). Next, the time points that corresponded to all individual cycles in one session were
1870 concatenated, which generated a new matrix of calcium activity in which the network engaged in the
1871 population oscillation uninterruptedly.

1872 The locking degree was computed for each cell as the mean resultant vector length over the phases of
1873 the population oscillation at which the calcium events occurred (bin size = 129 ms, function “circ_r” from

1874 the Circular Statistics Toolbox for Matlab¹⁰⁶). The locking degree has a lower bound of 0 and upper bound
1875 of 1. It is equal to 1 if all oscillation phases at which the calcium events occurred are the same, i.e. perfect
1876 locking, and equal to zero if all phases at which the calcium events occurred are evenly distributed (total
1877 absence of locking). To estimate significance, for each cell a null distribution of locking degrees was built
1878 by temporally shuffling the calcium activity of that cell 1000 times while the phase of the oscillation
1879 remained unchanged, and by computing, for each shuffle realization, the locking degree (shuffling was
1880 performed as in “Sorting of temporally shuffled data”). The 99th percentile of the estimated null
1881 distribution was used as a threshold for significance.

1882 In order to assess the robustness of the locking degree, the obtained results were compared with a
1883 second measure based on information theory¹⁰⁷: the mutual information between the counts of calcium
1884 events (“event counts”) and the phase of the oscillation (bin size = 0.52 s). To estimate the reduction in
1885 uncertainty about the phase of the oscillation (P) given the event counts of the calcium activity (S),
1886 Shannon’s mutual information was computed as follows¹⁰⁸:

1887
$$MI(S,P) = \sum_{p,s} Prob(p,s) \log_2 \frac{Prob(p,s)}{Prob(p)Prob(s)}, \text{ (Equation 4)}$$

1888 where $Prob(p,s)$ is the joint probability of observing a phase of the oscillation p and an event count s ,
1889 $Prob(s)$ is the marginal probability of event counts and $Prob(p)$ is the marginal probability of the phase
1890 of the oscillation. All probability distributions were estimated from the data using discrete
1891 representations of the phase of the oscillation and the event counts. The event counts were partitioned
1892 into $s_{\max}+1$ bins to account for the absence of event counts as well as all possible event counts, where
1893 s_{\max} is the maximum number of event counts per cell in a 0.52 s bin, and the phase of the oscillation was
1894 discretized into 10 bins of size $\frac{2\pi}{10}$.

1895 The mutual information is a non-negative quantity that is equal to zero only when the two variables are
1896 independent, i.e. when the joint probability is equal to the product of the marginals $Prob(p,s) =$
1897 $Prob(p)Prob(s)$. However, limited sampling can lead to an overestimation in the mutual information
1898 in the form of a bias¹⁰⁹. In order to correct for this bias, the calcium activity was temporally shuffled (as
1899 in “Sorting of temporally shuffled data”) and the mutual information between the event counts of the
1900 shuffled calcium activity and the phase of the oscillation, which remained unchanged, was calculated.
1901 This procedure, which destroyed the pairing between event counts and phase of the oscillation, was
1902 repeated 1000 times and the average mutual information across the 1000 iterations was computed and
1903 used as an estimation of the bias in the mutual information calculation. In the right panel of Fig. 3a, we
1904 report both the mutual information and the bias. In Extended data Fig. 6a, the corrected mutual
1905 information was reported (MI_c), where the bias ($\langle MI_{sh} \rangle_{\text{iterations}}$) was subtracted out from the Shannon’s
1906 mutual information (MI): $MI_c = MI - \langle MI_{sh} \rangle_{\text{iterations}}$.

1907 Note that the locking degree and the mutual information between the event counts and the phase of
1908 the oscillation yielded consistent results (see Fig. 3a and Extended data Fig. 6a).

1909 **Tuning of single cells to the phase of the oscillation**

1910 The selectivity of each cell to the phase of the oscillation was visualized through tuning curves and
1911 quantified through their preferred phase.

1912 Tuning curves: The phase of the oscillation $\varphi(t)$ was estimated (Equation 1) and the range of phases
1913 $[-\pi, \pi)$ was partitioned into 40 bins of size $\frac{2\pi}{40}$ rad. For each cell the tuning curve in the phase bin j , $j =$
1914 $0, \dots, 39$, was calculated as the total number of event counts that occurred at phases within the range
1915 $\left[-\pi + j \frac{2\pi}{40}, -\pi + (j + 1) \frac{2\pi}{40}\right)$ divided by the total number of event counts during the population
1916 oscillation.

1917 Preferred phases: The preferred phase of each cell was calculated as the circular mean over the
1918 oscillation phases at which the calcium events occurred (function “circ_mean” from the Circular
1919 Statistics Toolbox for Matlab¹⁰⁶).

1920 To determine the extent to which the preferred phases across locked cells were uniformly distributed
1921 in one recorded session, the distribution of the cells’ preferred phases, that we shall denote Q , was
1922 estimated by discretizing the preferred phases into 10 bins of size $\frac{2\pi}{10}$ rad. The entropy of this distribution
1923 $H_Q = -\sum_{x=1}^{10} Q(x)\log_2(Q(x))$ was calculated and used to compute the entropy ratio H_{ratio} , which
1924 quantifies how much Q departs from a flat distribution:

1925
$$H_{ratio} = \frac{H_Q}{H_{flat}} \quad (\text{Equation 5})$$

1926 where H_{flat} is the entropy of a flat distribution using 10 bins, i.e. $H_{flat} = 3.32$ bits. The closer H_{ratio} is
1927 to 1 the flatter Q is, and therefore all preferred phases tend to be equally represented. The smaller
1928 H_{ratio} is, the more uneven Q is and some preferred phases tend to be more represented than others.

1929 To estimate significance, for each session the procedure for calculating H_{ratio} was repeated for 1000
1930 iterations of a shuffling procedure where the preferred phase of the cells was calculated after the values
1931 of the phase of the oscillation were temporally shuffled. In Extended data Fig. 6f, both panels, for each
1932 session the 1000 shuffle realizations were averaged.

1933 **Participation index**

1934 The Participation Index (PI) quantifies the extent to which a cell’s calcium events were distributed across
1935 all cycles of the population oscillation, or rather concentrated in a few cycles. The participation index
1936 was calculated for each cell separately as the fraction of cycles needed to account for 90% of the total
1937 number of calcium events. To compute the participation, individual cycles were identified (see
1938 “Identification of individual oscillation cycles”), and for each cell the number calcium events per cycle
1939 was calculated and normalized by the total number of calcium events across all concatenated cycles,
1940 which yields the fraction of calcium events per cycle. This quantity was sorted in an ascending manner
1941 and its cumulative sum was calculated. The participation index is the minimum fraction of the total
1942 number of the cycles for which the cumulative sum of the fraction of calcium events per cycle ≥ 0.9
1943 (results remain unchanged when the cumulative sum is required to be ≥ 0.95).

1944 **Relationship between tuning to the phase of the oscillation and single-cell oscillatory frequency**

1945 To determine whether the frequency of oscillation of single cell calcium activity was correlated with the
1946 extent to which the cell was locked and participated in the population oscillation, for each cell the ratio
1947 between its oscillatory frequency (see “Autocorrelations and spectral analysis of single cell calcium
1948 activity”) and the frequency of the population oscillation (see “Cycle length, population oscillation
1949 frequency and inter-cycle interval”) was calculated and denoted “relative frequency”. Next, for each
1950 session cells were divided into two groups: one group had cells with relative frequency ~ 1 (cells whose
1951 oscillatory frequencies were most similar to the population oscillation frequency), and the other group
1952 had cells with relative frequency $\neq 1$ (cells whose oscillatory frequencies were most different from the
1953 population oscillation frequency). The size of each group was the same and was given by a percentage
1954 α of the total number of recorded cells in a session. For each group the locking degree (see “Locking to
1955 the phase of the oscillation”) and the participation index (see “Participation index”) were compared. For
1956 the quantification across all 15 oscillatory sessions, the mean locking degree and participation index
1957 were calculated for each group separately and for each session separately, and all 15 sessions were
1958 pooled. α was varied from 5% to 50%.

1959

1960 **Anatomical distribution of preferred phases and participation indexes**

1961 To determine whether the entorhinal population oscillation resembled travelling waves, during which
1962 neural population activity moves progressively across anatomical space⁴³⁻⁴⁸, the distributions of
1963 anatomical pairwise distances for cells with similar and different (1) preferred phase and (2)
1964 participation index were computed. To perform these quantifications the first step was to calculate, for
1965 each session, the anatomical distance between all pairs of cells. To calculate those pairwise distances
1966 we used the centroid of each cell in the FOV (Suite2P³⁹).

1967 Preferred phase: Because the progression of the neural population activity during the population
1968 oscillation can be tracked by the phase of the oscillation (Fig. 2e), we determined whether there is
1969 topography in the cells' preferred phases. The preferred phase of all cells in one session were computed
1970 (see "Tuning of single cells to the phase of the oscillation") and cells were divided into two groups, one
1971 of preferred phases ~ 0 rad, and one of preferred phases $\sim \pi$ rad (Extended data Fig. 6i). The size of each
1972 group was the same and was given by a percentage α of the total number of locked cells in a session
1973 (see "Locking to the phase of the oscillation"). All cells in each group were locked to the phase of the
1974 oscillation. α was varied from 5% to 50%. Pairwise anatomical distances between the cells with preferred
1975 phase ~ 0 rad were calculated and assigned to the group "similar". Pairwise anatomical distances in the
1976 "different" group were determined such that one cell of each pair had a preferred phase ~ 0 rad and the
1977 other cell a preferred phase $\sim \pi$ rad. A comparison of the two groups of pairwise distances is shown for
1978 one example session in Fig. 3f left. For quantification across all 15 oscillatory sessions, in Fig. 3f right,
1979 the means for the two groups, similar and different, were computed for each session separately. Notice
1980 that there were no significant differences in the pairwise anatomical distances between cells with similar
1981 and different preferred phases regardless of the value of α (Extended data Fig. 6j).

1982 Participation index: Given that several properties of MEC cells follow a dorsoventral or mediolateral
1983 organization^{2,3,42} we determined whether there is topography in the neurons' participation in the
1984 oscillation cycles (see "Participation index"). The same procedure as described for the preferred phases
1985 was followed. Cells were divided into two groups. The size of each group was the same and was given
1986 by a percentage α of the total number of locked cells in a session. One group comprises the cells with
1987 the lowest participation indexes, and the other group the cells with the highest participation indexes
1988 (Extended data Fig. 6k). Pairwise anatomical distance between all cell pairs in the low participation index
1989 group were calculated and assigned to the group "similar". Pairwise anatomical distances for the
1990 "different" group were determined for all pairs of cells such that one cell of the pair belonged to the low
1991 participation index group, and the other cell to the high participation index group. Notice that there
1992 were no significant differences in pairwise anatomical distances between cells with similar and different
1993 PIs regardless of the value of α (Extended data Fig. 6l).

1994 **Procedure for merging steps**

1995 In order to average out the variability observed in single cells at the level of oscillatory frequency, locking
1996 degree and participation index while preserving the temporal properties of the population oscillation,
1997 an iterative process that defines new variables from combining the calcium activity of cells in small
1998 neighborhoods was implemented for each session separately (Extended data Fig. 7a). This process is
1999 similar to a coarse-graining approach¹¹⁰.

2000 First, the N recorded cells in one session were sorted according to the PCA method. In the first iteration
2001 of the procedure, named merging step one, the calcium activity (see "Binary deconvolved calcium
2002 activity and matrix of calcium activity") of pairs of cells that were positioned next to each other in the
2003 PCA sorting were added up (merging step 1 in Extended data Fig. 7a). This resulted in $\frac{N}{2}$ new variables,
2004 which in merging step 2 were grouped together in pairs of adjacent variables by adding up their activity,

2005 which yielded $\frac{N}{4}$ new variables. Note that because in the PCA sorting cells whose activity is synchronous
 2006 are positioned adjacent to each other, the new variables consist of groups of co-active cells.

2007 In general, merging step j generates $\frac{N}{2^j}$ variables by adding up the activity of pairs of $\frac{N}{2^{j-1}}$ variables from
 2008 merging step $j - 1, j > 1$, with each new variable defined as:

2009
$$\tilde{\sigma}_i = \frac{\sigma_{2i-1} + \sigma_{2i}}{2} \quad i = 1, \dots, \frac{N}{2^j}$$

2010 where $\tilde{\sigma}_i$ is the i^{th} new variable that results from adding up σ_{2i-1} and σ_{2i} , which were computed in the
 2011 previous merging step, $j - 1$. In merging step 1, σ_{2i-1} and σ_{2i} are the calcium activity of cells in the
 2012 position $2i - 1$ and $2i, 1 \leq i \leq N$, in the sorting obtained with the PCA method.

2013 This procedure was repeated 6 times until ~ 10 variables were obtained in each session (the exact
 2014 number of variables depended on the number of recorded cells, N , in each session). If N was an odd
 2015 number, the last cell in the sorting obtained with the PCA method was discarded and the procedure was
 2016 applied to the first $N - 1$ cells in the sorting. In every merging step the participation index (see
 2017 "Participation index") of each new variable was calculated (see Extended data Fig. 7b).

2018 **Division of cells into ensembles**

2019 After 5 merging steps (and for approximately 10 variables), the participation index reached a plateau
 2020 (Extended data Fig. 7b). This motivated the decision to split the recorded cells into 10 variables, which
 2021 we later used to quantify the network dynamics (see "Analysis of network dynamics using ensembles of
 2022 co-active cells"). From now on we will refer to those variables as "ensembles", to highlight the fact that
 2023 cells in each ensemble are co-active. The same number of ensembles was used in sessions that did not
 2024 exhibit population oscillations.

2025 To distribute cells into 10 ensembles, cells were sorted according to the PCA method. If $\frac{N}{10}$ is an integer,
 2026 where N is the total number of cells in one session, then each ensemble contains $\frac{N}{10}$ cells and the set of
 2027 cells that belong to ensemble $i, 1 \leq i \leq 10$, is $\left\{ (i - 1) \cdot \frac{N}{10} + 1, (i - 1) \cdot \frac{N}{10} + 2, \dots, i \cdot \frac{N}{10} \right\}$. If $\frac{N}{10}$ is not
 2028 an integer then ensembles 1 to 9 contain $\left\lfloor \frac{N}{10} \right\rfloor$ cells and ensemble 10 contains $N - 9 \cdot \left\lfloor \frac{N}{10} \right\rfloor$ cells, where
 2029 $\lfloor x \rfloor = \max\{m \in \mathbb{N} / m \leq x\}$ and \mathbb{N} is the set of natural numbers. In this case the set of cells that
 2030 belongs to each ensemble is:

2031
$$\left(\begin{array}{l} \left\{ (i - 1) \cdot \left\lfloor \frac{N}{10} \right\rfloor + 1, (i - 1) \cdot \left\lfloor \frac{N}{10} \right\rfloor + 2, \dots, i \cdot \left\lfloor \frac{N}{10} \right\rfloor \right\}, \quad 1 \leq \text{ensemble} \leq 9 \\ \left\{ 9 \cdot \left\lfloor \frac{N}{10} \right\rfloor + 1, 9 \cdot \left\lfloor \frac{N}{10} \right\rfloor + 2, \dots, N \right\}, \quad \text{ensemble} = 10 \end{array} \right)$$

2032

2033 Note that each cell was assigned to only one ensemble.

2034 After each cell was assigned to one of the 10 ensembles, the activity of each ensemble as a function of
 2035 time was calculated as the mean calcium activity across cells in that ensemble.

2036 Finally, to calculate the oscillation frequency of ensemble activity, the PSD was calculated (Welch's
 2037 methods, 8.8 min Hamming window with 50% overlap between consecutive windows, "pwelch" Matlab
 2038 function). The oscillation frequency was estimated as the frequency at which the PSD peaked. For each
 2039 session, the oscillation frequency of the activity of the ensembles was compared to the frequency of the
 2040 population oscillation, which was computed as the total number of cycles in the session divided by the

2041 amount of time the network engaged in the population oscillation. The latter was calculated as the
2042 length of the temporal window of concatenated cycles (see “Identification of individual oscillation
2043 cycles”).

2044 **Tuning of single-cell activity to ensemble activity**

2045 To quantify the degree of tuning of a cell’s calcium activity to the ensemble activity, and hence
2046 determine whether ensemble activity was representative of single cell calcium activity, we calculated,
2047 for all cells in a recorded session, the Pearson correlation between the calcium activity and the ensemble
2048 activity. Cells were divided into 10 ensembles (see “Division of cells into ensembles”) and the activity of
2049 each ensemble as a function of time was calculated as the mean calcium activity across cells in the
2050 ensemble (bin size = 129 ms). For each neuron i , $1 \leq i \leq N$, where N is number of recorded cells in the
2051 session, the Pearson correlation $P_{i,j}$ between the neuron’s calcium activity and the activity of ensemble
2052 j , $1 \leq j \leq 10$, was calculated for each ensemble separately. When calculating this set of 10 correlations,
2053 the activity of the cell for which the tuning is being computed was excluded in the calculation of the
2054 ensemble activity (note that by construction each cell is assigned to only one ensemble). Next, for each
2055 cell i , the most representative ensemble was calculated as the one for which the Pearson correlation
2056 was maximal, i.e.,

$$2057 \quad \text{most_representative_ensemble}_i = \arg \max_j P_{i,j}. \text{ (Equation 6)}$$

2058 In order to determine whether the activity of the ensemble a cell was assigned to (see “Division of cells
2059 into ensembles”) was the most representative of the single cell calcium activity, we quantified how
2060 similar the most representative ensemble and the ensemble assigned based on the PCA sorting were,
2061 expecting that the most representative ensemble and the assigned ensemble would coincide. For each
2062 cell the distance between these was computed subject to periodic boundary conditions in the ensembles
2063 (for example, the distance between ensemble one and ten was one and not nine).

2064 For each session the fraction of cells that displayed specific distances between their assigned ensemble
2065 based on the PCA sorting and their most representative ensemble was calculated for the entire range of
2066 distances and presented as a probability. Probabilities were next averaged across sessions (Extended
2067 data Fig. 7f). To estimate significance, for each cell in a session the procedure for identifying the most
2068 representative ensemble was repeated in 500 iterations of a shuffle realization where the ensemble
2069 activity remained fixed but the calcium activity was temporally shuffled (as in “Sorting of temporally
2070 shuffled data”). For each of the 500 shuffle realizations per session the probabilities of observing specific
2071 distances between the PCA-assigned and the most representative ensemble were calculated and
2072 averaged, yielding the mean shuffled probability per session. These probabilities (15 in total for the 15
2073 oscillatory sessions) were then pooled and compared to the recorded data.

2074 The probability that the assigned ensemble based on the PCA method and the most representative
2075 ensemble coincide was large for MEC (Extended data Fig. 7f), intermediate for VIS and low for PaS
2076 (Extended data Fig. 10c).

2077 **Anatomical distribution of ensembles**

2078 Analyses performed on the preferred phases and participation indexes of single cells indicated that the
2079 population oscillation is not topographically organized, and hence it is not a travelling wave (see
2080 “Anatomical distribution of preferred phases and participation indexes” and Fig. 3e-h). To determine
2081 whether this result was upheld when cells were sorted in ensembles of co-active neurons, the centroid
2082 of each cell in the FOV (provided by Suite2P³⁹) was used to calculate the anatomical distance between
2083 all pairs of cells in a session. Next, for each session the pairwise anatomical distances were divided into
2084 two groups: the “within ensemble” group and the “across ensemble” group. In the former, only pairwise

2085 anatomical distances between cells that were assigned to the same ensemble were considered (see
2086 “Division of cells into ensembles”). In the latter, we considered pairwise anatomical distances between
2087 cells of different ensembles, such that one cell of the pair was assigned to ensemble i , $i = 1, \dots, 10$, and
2088 the other to ensemble j , $j = 1, \dots, 10$, $i \neq j$. This was done for each session and each ensemble
2089 separately. In Extended data Fig. 7j, for each ensemble of the example session shown in Fig. 2a, the
2090 “within ensemble” group was compared to the “across ensemble” group. Next, for the example session,
2091 the data in both groups was pooled and the two groups were compared in the left panel of Extended
2092 data Fig. 7k. For the quantification across all 15 oscillatory sessions in the right panel of Extended data
2093 Fig. 7k (including the session in Extended data Fig. 7j), the means in both groups were calculated for
2094 each session separately.

2095 **Analysis of network dynamics using ensembles of co-active cells**

2096 We adopted an ensemble approach to quantify the network dynamics (see “Procedure for merging
2097 steps” and “Division of cells into ensembles”). With a total of 10 ensembles this approach averaged out
2098 the variability observed in single-cell oscillation frequency, locking degree and participation index while
2099 keeping the temporal progression of the oscillatory sequences (Extended data Fig. 7n). In sessions with
2100 population oscillations, all individual cycles were identified (see “Identification of individual oscillation
2101 cycles”) and the corresponding time bins were concatenated, which yielded a new matrix of calcium
2102 activity in which the population oscillation was uninterrupted. Next, cells were divided into ensembles
2103 (see “Division of cells into ensembles”) and ensemble activity was downsampled using as bin size the
2104 oscillation bin size of the session (see “Oscillation bin size”). This procedure yielded a matrix, the
2105 “ensemble matrix”, with the activity of each ensemble corresponding to a single row (10 rows in total),
2106 and as many columns as time points when sampled at the oscillation bin size. In non-oscillatory sessions,
2107 the full matrix of calcium activity was used and the temporal downsampling was conducted at the mean
2108 oscillation bin size computed across all 15 oscillatory sessions; i.e. bin size = 8.5 s (see “Oscillation bin
2109 size calculation” for a description of the bin size used in non-oscillatory sessions). For both types of
2110 sessions (with and without oscillations), the activity of the 10 ensembles was described through a vector
2111 expressing, at each time point, the ensemble number with the highest activity at that time point (see
2112 Extended data Fig. 7m,n). This vector was used to perform the following analyses (i-iii).

2113 (i) Transition probabilities and graph representation: The transition probability from ensemble i to
2114 ensemble j was quantified as the number of times the transition $i \rightarrow j$ was observed in the data of one
2115 session, normalized by the total number of transitions in one session. Transitions were identified from
2116 the vector that contained the ensemble number with maximum activity at each time point (transitions
2117 to the same ensemble between consecutive time points were disregarded). Transitions were allocated
2118 in a matrix of transition probabilities T of size 10x10, since 10 ensembles were used. In this matrix, the
2119 component (i, j) expressed the transition probability from ensemble i to ensemble j .

2120 To establish statistical significance of the transition probabilities, the data was shuffled 500 times. In
2121 each shuffle realization, each row of the matrix of calcium activity (with concatenated cycles in the case
2122 of oscillatory sessions) was temporally shuffled (as in “Sorting of temporally shuffled data”), and the
2123 procedure for calculating the ensemble matrix and transition probabilities was applied to the shuffled
2124 data. For each transition $i \rightarrow j$ the 95th percentile of the null distribution was used to define a cut-off.

2125 The matrices of transition probabilities obtained from the recorded data and from the shuffle
2126 realizations were used as adjacency matrices to create graphs. In the graph representation each node
2127 represents one ensemble, each edge indicates the transition probability between two nodes, the
2128 thickness of the edge is proportional to the transition probability, and the arrow indicates the transition
2129 direction. In Extended data Fig. 7p and Extended data Fig. 10d, the edges in red indicate that the
2130 corresponding transition probabilities were larger than the cut-off for significance.

2131 (ii) Probability of sequential activation of ensembles: To determine whether preferences in ensemble
2132 transitions gave rise to sequences of ensemble activity, we calculated the probability of sequential
2133 ensemble activation according to the following procedure. From the vector expressing the ensemble
2134 number with the highest activity at each time point (sampled at the oscillation bin size), strictly
2135 increasing sequences of all possible lengths (from 2 to 10 ensembles) were identified. The number of
2136 ensembles in each sequence was the number of ensembles that were active in consecutive time points
2137 (epochs of sustained activity were disregarded). While the sequences had to be strictly increasing, they
2138 did not have to be continuous. Sequences could skip ensembles, in which case the maximum number of
2139 ensembles in one sequence was less than 10. The probability of the sequential activation of k
2140 ensembles, $k = 2, \dots, 10$, was next estimated as the number of times a sequence of k ensembles was
2141 found, normalized by the total number of identified sequences. Note that all subsequences were also
2142 included in this estimation. For example, if the ensembles 1, 2 and 3 were active in consecutive time
2143 points, a sequence of three ensembles was identified, as well as three subsequences of two ensembles
2144 each: 1,2, as well as 2,3 and 1,3.

2145 In order to test for significance, the shuffled data from “Transition probabilities and graph
2146 representation” was used. The procedure to compute the probability of sequential activation of
2147 ensembles was applied to each of the 500 shuffle realizations performed per session. Shuffled data was
2148 compared with recorded data.

2149 (iii) Sequence score: The *sequence score* measures how sequential the ensemble activity is. It is
2150 calculated from the probability of sequential activation of ensembles as the probability of observing
2151 sequences of 3 or more ensembles. The sequence score was calculated for each session of the dataset
2152 separately. To determine if the obtained scores were significant, for each session the 500 shuffle
2153 realizations used in “Probability of sequential activation of ensembles” for assessing significance of the
2154 probability of sequential activation of ensembles were used to calculate the sequence score on shuffled
2155 data. Those values were used to build a null distribution, and the 99th percentile of this distribution was
2156 chosen as the threshold for significance.

2157 **Estimation of number of completed laps on the wheel, speed and acceleration**

2158 Features of the animal’s behaviour were used to determine whether the MEC population oscillation was
2159 modulated by movement.

2160 The wheel had a radius of 8.54 cm (see “Self-paced running behavior under sensory-minimized
2161 conditions”) and a perimeter of 53.66 cm. Therefore animals had to run for ~53.7 cm to complete one
2162 lap on the wheel. For each session, we estimated the number of completed laps on the wheel from the
2163 position on the wheel recorded as a function of time. The number of completed laps during one cycle
2164 of the oscillation (see “Identification of individual oscillation cycles”) was calculated as the total distance
2165 run during the cycle divided by 53.7 cm.

2166 The speed of the animal was numerically calculated as the first derivative of the position on the wheel
2167 as a function of time (the sampling frequency of the position was 40 Hz for mice 60355 (MEC), 60353,
2168 60354 and 60356 (PaS). The sampling frequency was 50 Hz for mice 60584 and 60585 (MEC), 60961,
2169 92227 and 92229 (VIS). For mice 59911, 59914 (MEC) and 59912 (PaS), the wheel tracking was not
2170 synchronized to the ongoing image acquisition; see “Self-paced running behavior under sensory-
2171 minimized conditions”. The obtained speed signal from the former group of mice was interpolated so
2172 that the speed values matched the downsampled imaging time points (sampling frequency = 7.73 Hz),
2173 and smoothed using a square kernel of 2 s width. A threshold was applied such that all speed values that
2174 were less than 2 cm/s were set to zero and all speed values larger than 2 cm/s remained unchanged.
2175 The obtained speed signal was used to define immobility (running) bouts as the set of consecutive time
2176 points (bin size=129 ms) for which the speed was equal to (larger than) zero (a similar approach was

2177 used in ref. 36). The acceleration was numerically calculated as the first derivative of the speed signal.
2178 Notice that in this case no interpolation was needed.

2179 Because the available data did not have enough statistical power, it was not possible to compare the
2180 animals' behaviour, for example in terms of its running speed and acceleration, between periods with
2181 and without ongoing population oscillations.

2182 **Estimation of the probability of observing population oscillations**

2183 To determine whether the MEC population oscillation was observed during different behavioural states,
2184 the probability of observing the population oscillation was calculated conditioned on whether the
2185 animal was running or immobile. For each oscillatory session with behavioural tracking synchronized to
2186 the imaging data (10 sessions over 3 animals, see "Self-paced running behavior under sensory-
2187 minimized conditions" and "Oscillation score"), all individual cycles were identified (see "Identification
2188 of individual oscillation cycles"). The subset of time bins that belonged to individual cycles of the
2189 oscillation were extracted and labeled as "oscillation". Next, a second label was assigned to the time
2190 bins depending on whether they occurred during running or immobility bouts (bin labelled as "running"
2191 and "immobility" respectively, see "Estimation of number of completed laps on the wheel, speed and
2192 acceleration"). After applying this procedure, each time bin had two labels, one indicating the running
2193 behavior, and one indicating the presence (or absence) of population oscillation. To estimate the
2194 probability of observing the population oscillation conditioned on the animal's running behavior, all bins
2195 labelled as running or immobility were identified and from each subset, the fraction of bins labelled as
2196 oscillation was calculated. These probabilities were computed for each session separately.

2197 **Sequences during immobility bouts of different lengths**

2198 The population oscillation occurred both during running and immobility bouts. To quantify the extent
2199 to which individual cycles progressed during different lengths of immobility bouts, the following
2200 procedure was adopted. First, for each session, all immobility bouts were identified and assigned to bins
2201 of different lengths (see "Estimation of number of completed laps on the wheel, speed and
2202 acceleration"; length bins = 0-3s, 3-5s, 5-10s, 10-15s, 15-20s, >25 s). Second, all individual oscillation
2203 cycles were identified (see "Identification of individual oscillation cycles"). Third, for each session and
2204 each length bin, the fraction of immobility bouts that were fully occupied by continued cycles was
2205 calculated. To estimate significance, for each session the time bins that belonged to all individual cycles
2206 were temporally shuffled. The third step of the procedure described above was performed for 500
2207 shuffle iterations per session. In Fig. 5c, the recorded data has 10 data points per length bin, and the
2208 shuffled data has 5000 data points per length bin, since 500 shuffled realizations per session were
2209 pooled.

2210 **Analysis of speed and cycle onset**

2211 To determine whether the onset of the MEC population oscillation cycles was modulated by the animal's
2212 running speed, changes in speed before and after cycle onset were investigated. For each session all
2213 individual cycles were identified (see "Identification of individual oscillation cycles") and for each cycle
2214 the mean speed over windows of 10 s before and after cycle onset was calculated. Because no
2215 differences in the mean speed were observed before and after onset (Extended data Fig. 2d left panel),
2216 we next determined whether changes in speed were correlated with the onset of oscillation epochs,
2217 which were defined as epochs with uninterrupted oscillations, i.e. epochs with successive cycles. The
2218 same analysis described above was repeated but only for the subset of cycles that were 10 s or more
2219 apart, i.e. for cycles that belonged to different oscillation epochs.

2220

2221 **Manifold visualization for example session in VIS and PaS**

2222 To visualize whether the topology of the manifold underlying the population activity in example sessions
2223 recorded in VIS and PaS was also a ring, PCA was used and a similar procedure to the one described in
2224 “Manifold visualization for MEC sessions” was adopted.

2225 For each example session, one corresponding to VIS and one corresponding to PaS (Fig. 6a-d), PCA was
2226 applied to the matrix of calcium activity, which first had each row convolved with a gaussian kernel of
2227 width equal to four times 8.5 s, which is the mean oscillation bin size computed across oscillatory
2228 sessions (see “Oscillation bin size”). Neural activity was projected onto the embedding generated by PC1
2229 and PC2. Extended data Fig. 9b shows the absence of a ring-shaped manifold in VIS and PaS example
2230 sessions.

2231 **Coactivity and synchronization in PaS and VIS sessions**

2232 Sessions recorded in PaS and VIS did not exhibit population oscillations. To further characterize their
2233 population activity, synchronization and neural co-activity were calculated.

2234 Synchronization: Neural synchronization was calculated as the absolute value of the Pearson correlation
2235 between the calcium activity of pairs of cells (bin size = 129 ms). For each session, the Pearson
2236 correlation was calculated for all pairs of calcium activity (correlations with the same calcium activity
2237 were not considered) and used to build a distribution of synchronization values. In Extended data Fig.
2238 10j, these distributions were averaged across sessions for each brain area separately.

2239 Co-activity: For each time bin in a session (bin size = 129 ms) the co-activity was calculated as the number
2240 of cells that had simultaneous calcium events divided by the total number of recorded cells in the
2241 session. This number represented the fraction of cells that was active in individual time bins. Using all
2242 time bins of the session, a distribution of co-activity values was calculated. In Extended data Fig. 10k,
2243 the distributions were averaged across sessions for each brain area separately.

2244 **Data analysis and statistical analysis**

2245 Data analyses were performed with custom-written scripts in Python and Matlab (R2021b). Results were
2246 expressed as the mean \pm SEM unless indicated otherwise. Statistical analysis was performed using
2247 MATLAB and p-values are indicated in the figure legends and figures (n.s.: $p > 0.05$, * $p < 0.05$, ** $p < 0.01$,
2248 *** $p < 0.001$). Student t-tests were used for paired and unpaired data. For data that displayed no
2249 Gaussian distribution and that was unpaired, the Wilcoxon rank-sum test was used. For paired data or
2250 one-sampled data, the Wilcoxon signed-rank test was used. Two-tailed tests were used unless otherwise
2251 indicated. Correlations were determined using Pearson or Spearman correlations. Friedman tests were
2252 used for analyses between groups. No statistical methods were used to predetermine sample sizes but
2253 our sample sizes were similar to those reported in previous publications from the lab and in other
2254 publications in the field.

2255 **Code availability**

2256 Code for reproducing the analyses in this article will be available after publication at Figshare and/or
2257 GitHub.

2258 **Data availability**

2259 The datasets generated during the current study will be available after publication at Figshare.

2260

2261

2262 **Methods references:**

- 2263 99. Donato, F., Jacobsen, R. I., Moser, M. B., & Moser, E. I. (2017). Stellate cells drive maturation of the
2264 entorhinal-hippocampal circuit. *Science*, 355(6330), eaai8178.
- 2265 100. Low, R. J., Gu, Y., & Tank, D. W. (2014). Cellular resolution optical access to brain regions in
2266 fissures: imaging medial prefrontal cortex and grid cells in entorhinal cortex. *Proceedings of the*
2267 *National Academy of Sciences*, 111(52), 18739-18744.
- 2268 101. Paxinos, G., & Franklin, K. B. (2019). *The Mouse brain in Stereotaxic Coordinates*. Academic press.
- 2269 102. Stringer, C., Pachitariu, M., Steinmetz, N., Reddy, C. B., Carandini, M., & Harris, K. D. (2019).
2270 Spontaneous behaviors drive multidimensional, brainwide activity. *Science*, 364(6437), eaav7893.
- 2271 103. Van Der Maaten, L., Postma, E., & Van den Herik, J. (2009). Dimensionality reduction: a
2272 comparative review. *J Mach Learn Res*, 10(66-71), 13.
- 2273 104. McInnes, L., Healy, J. & Melville, J. UMAP: Uniform manifold approximation and projection for
2274 dimension reduction. Preprint at <https://arxiv.org/abs/1802.03426> (2018).
- 2275 105. Connor Meehan, Jonathan Ebrahimian, Wayne Moore, and Stephen Meehan (2022). Uniform
2276 Manifold Approximation and Projection (UMAP)
2277 (<https://www.mathworks.com/matlabcentral/fileexchange/71902>), MATLAB Central File Exchange.
- 2278 106. Berens, P. (2009). CircStat: a MATLAB toolbox for circular statistics. *Journal of Statistical*
2279 *Software*, 31, 1-21.
- 2280 107. Shannon, C. E. (1948). A mathematical theory of communication. *The Bell System Technical*
2281 *Journal*, 27(3), 379-423.
- 2282 108. Cover, T.M., and Thomas, J. A. (2006). *Elements of Information Theory*. New Jersey, NJ: Wiley.
- 2283 109. Panzeri, S., Senatore, R., Montemurro, M. A., & Petersen, R. S. (2007). Correcting for the sampling
2284 bias problem in spike train information measures. *Journal of Neurophysiology*, 98(3), 1064-1072.
- 2285 110. Meshulam, L., Gauthier, J. L., Brody, C. D., Tank, D. W., & Bialek, W. (2019). Coarse graining, fixed
2286 points, and scaling in a large population of neurons. *Physical Review Letters*, 123(17), 178103.
- 2287

Figure 1

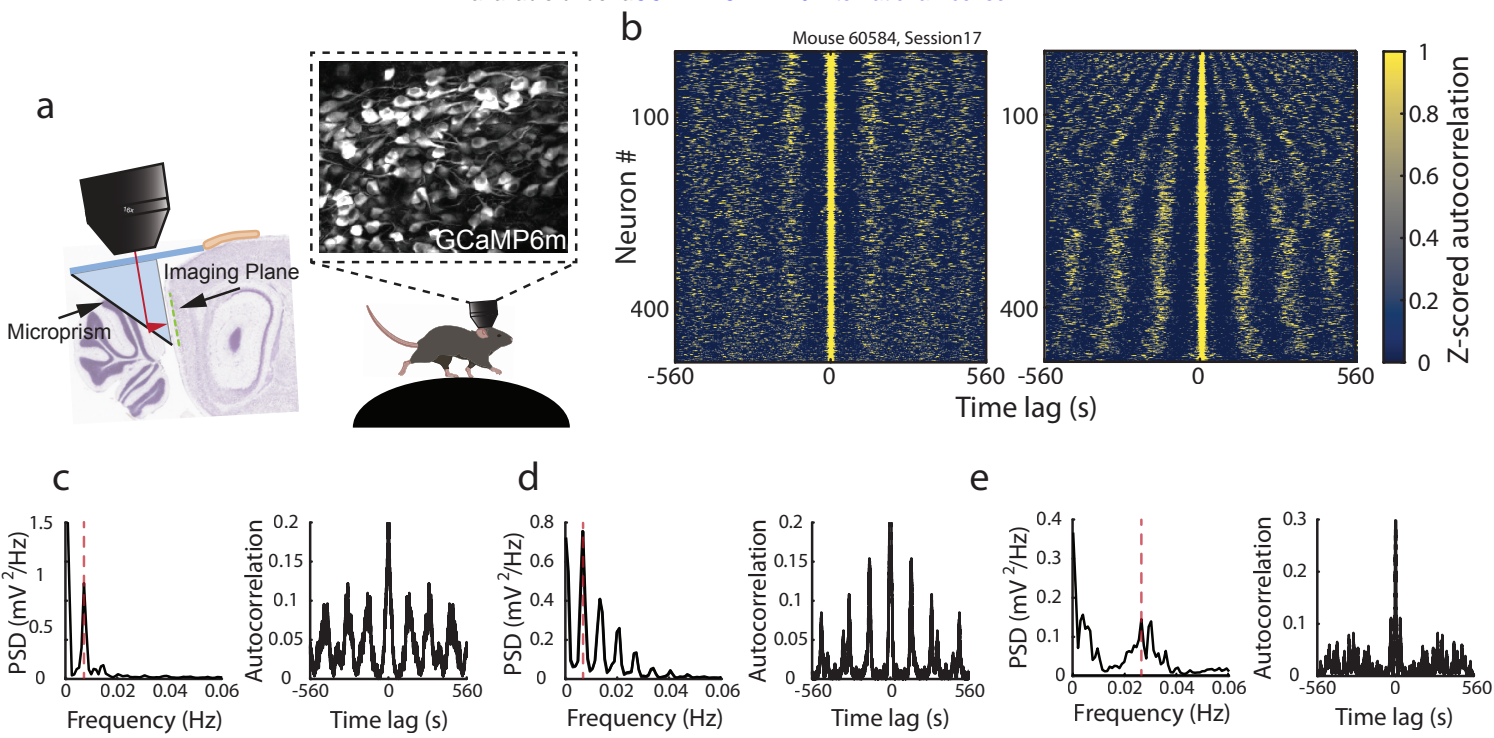
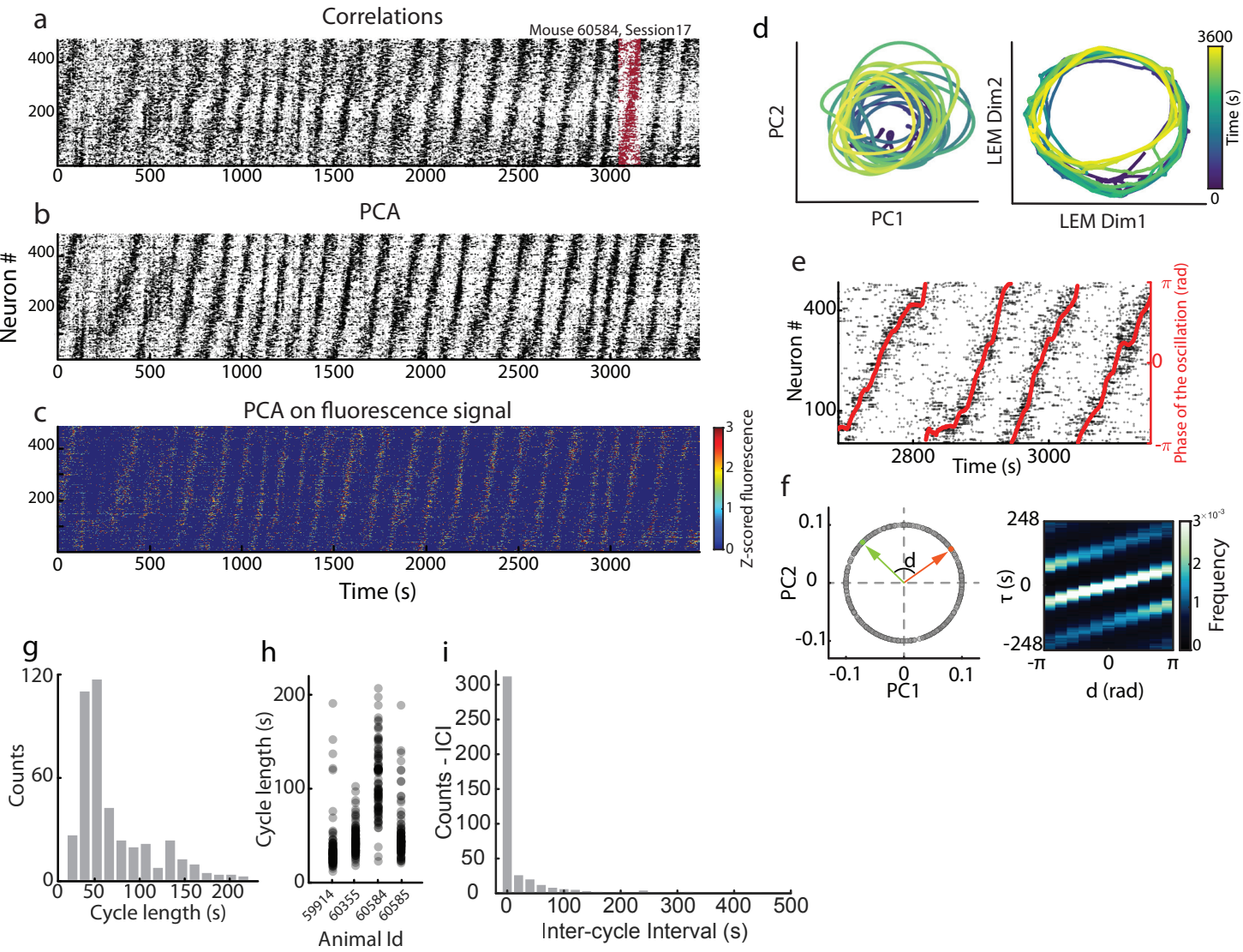
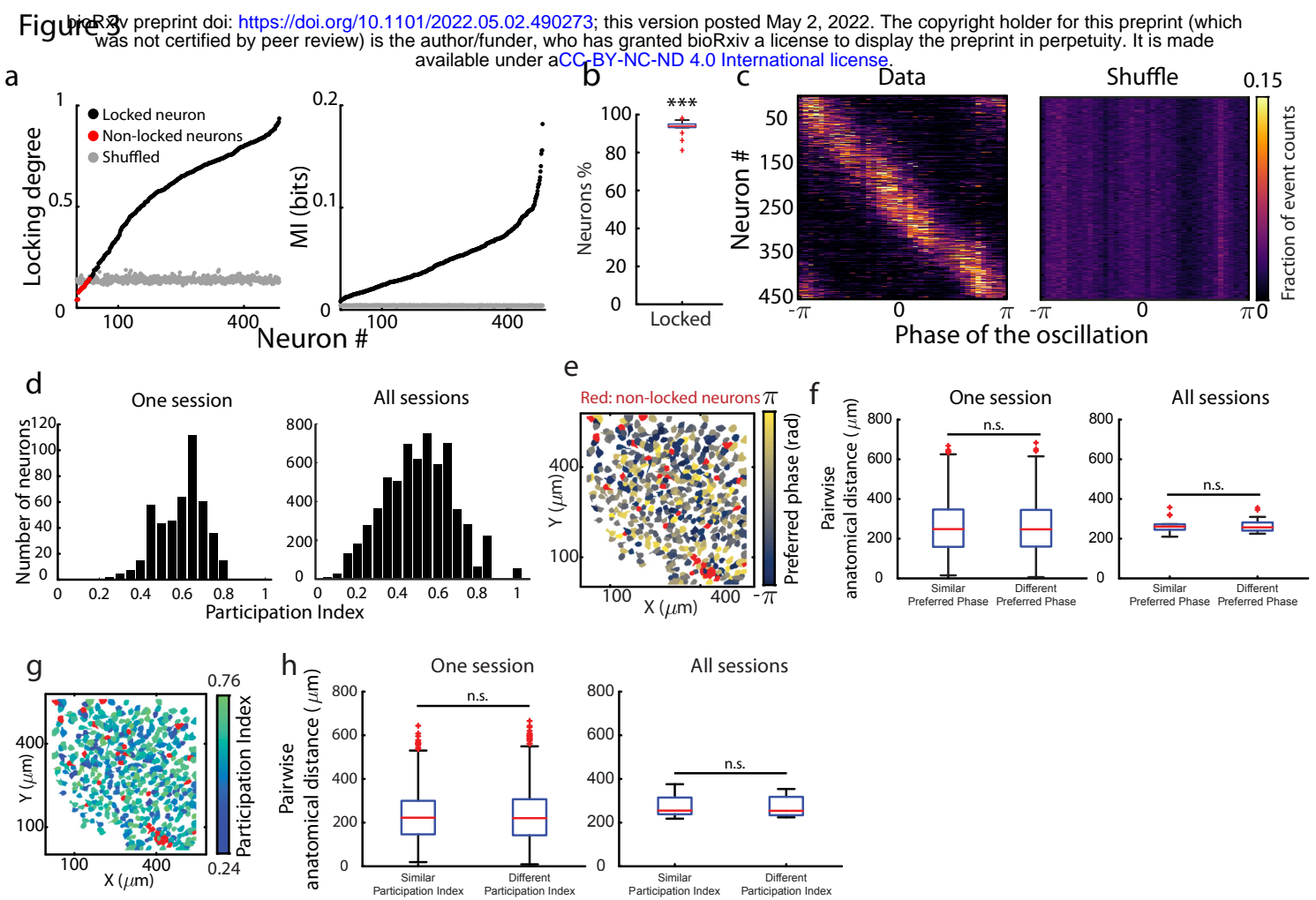


Figure 2





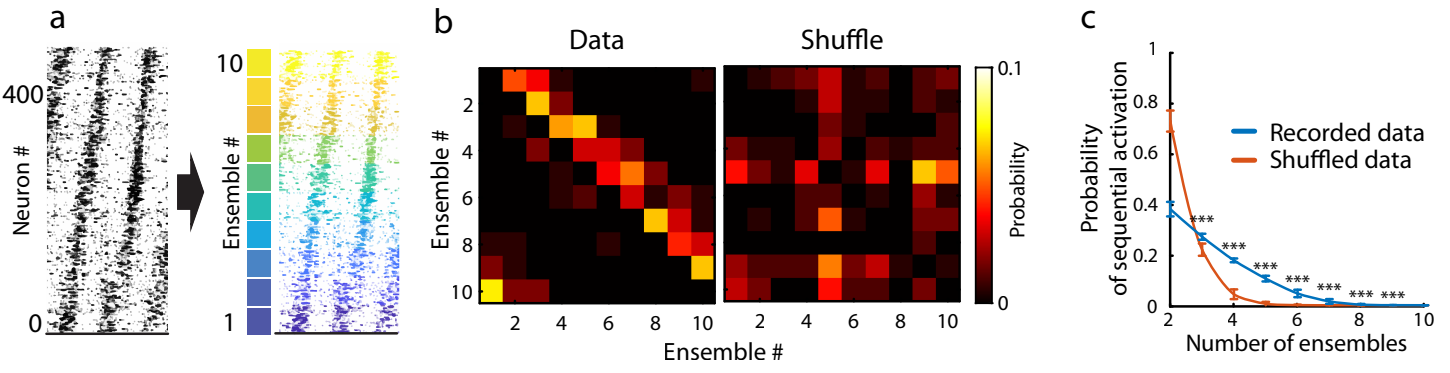


Figure 5

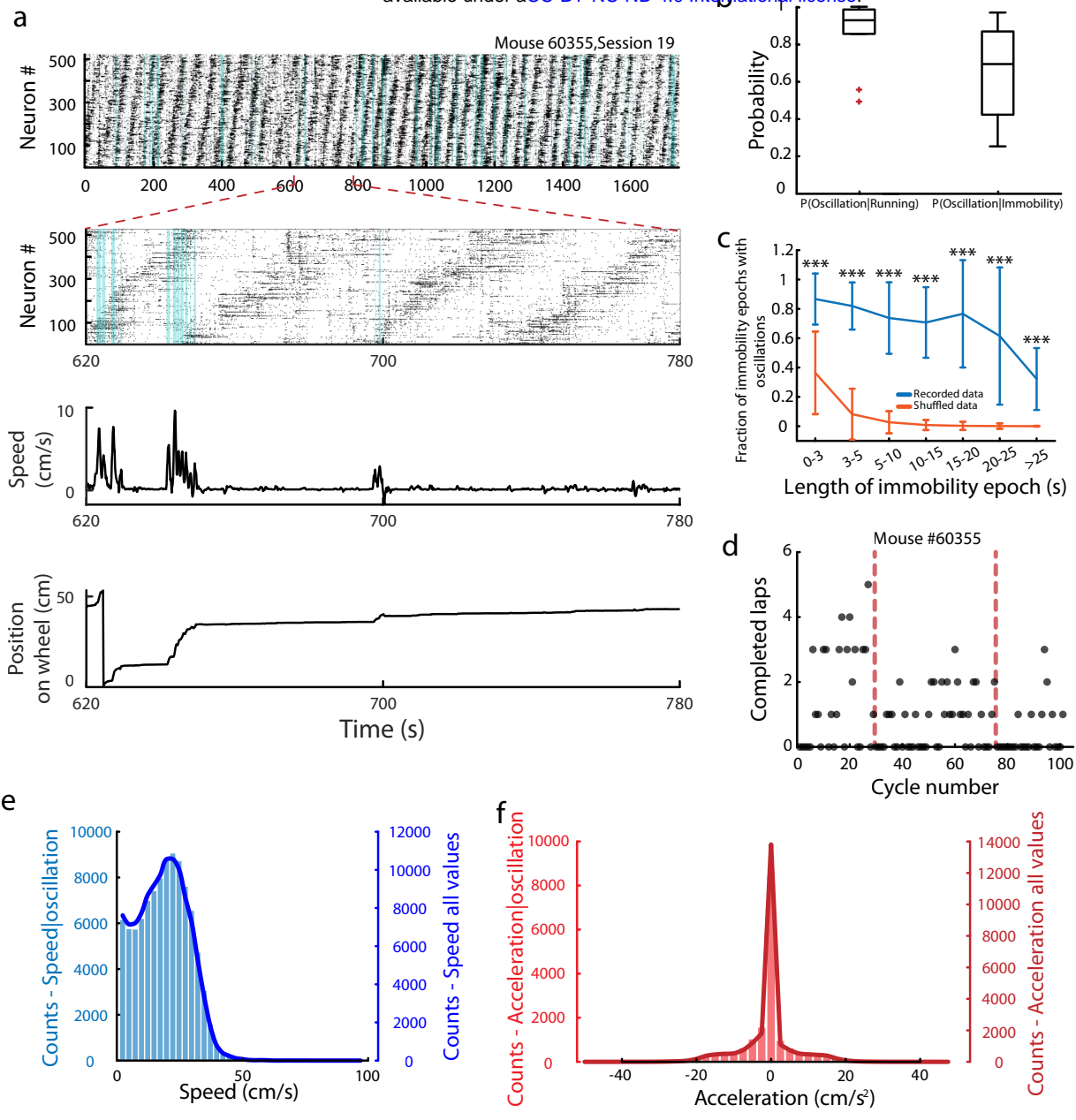
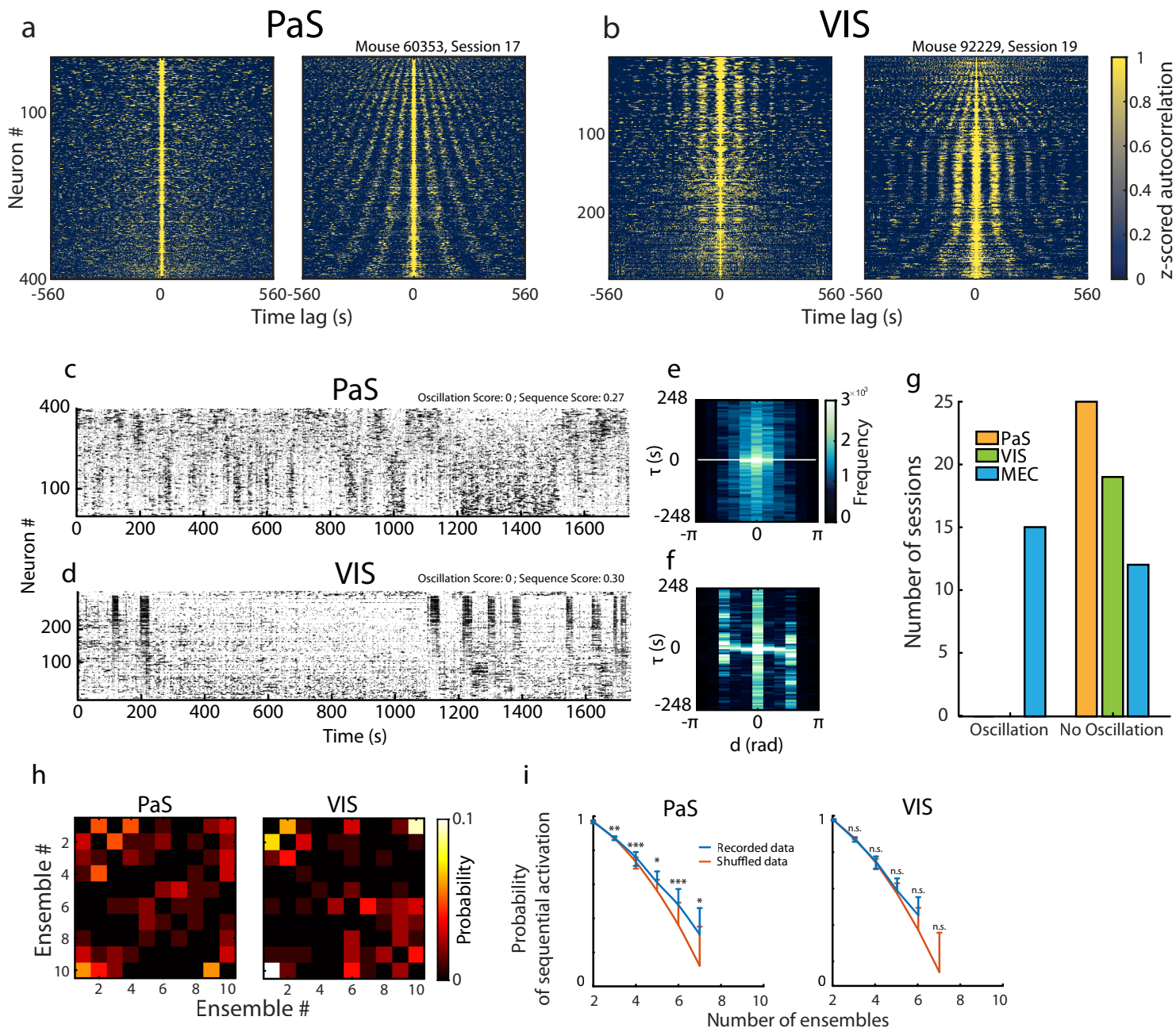
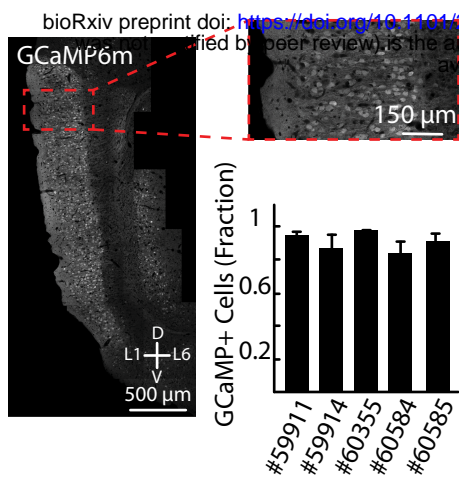


Figure 6



Extended data Figure 1

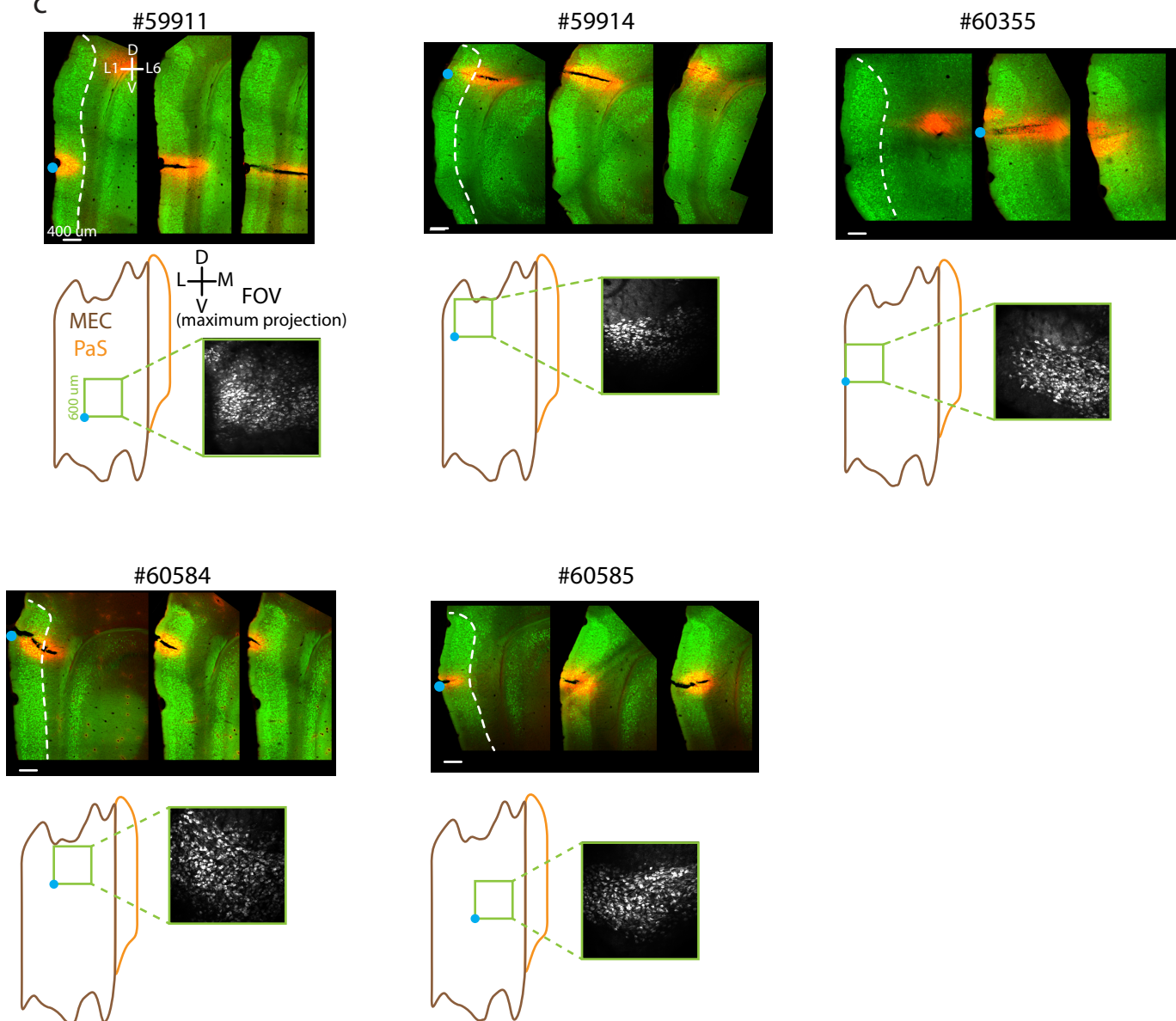
a



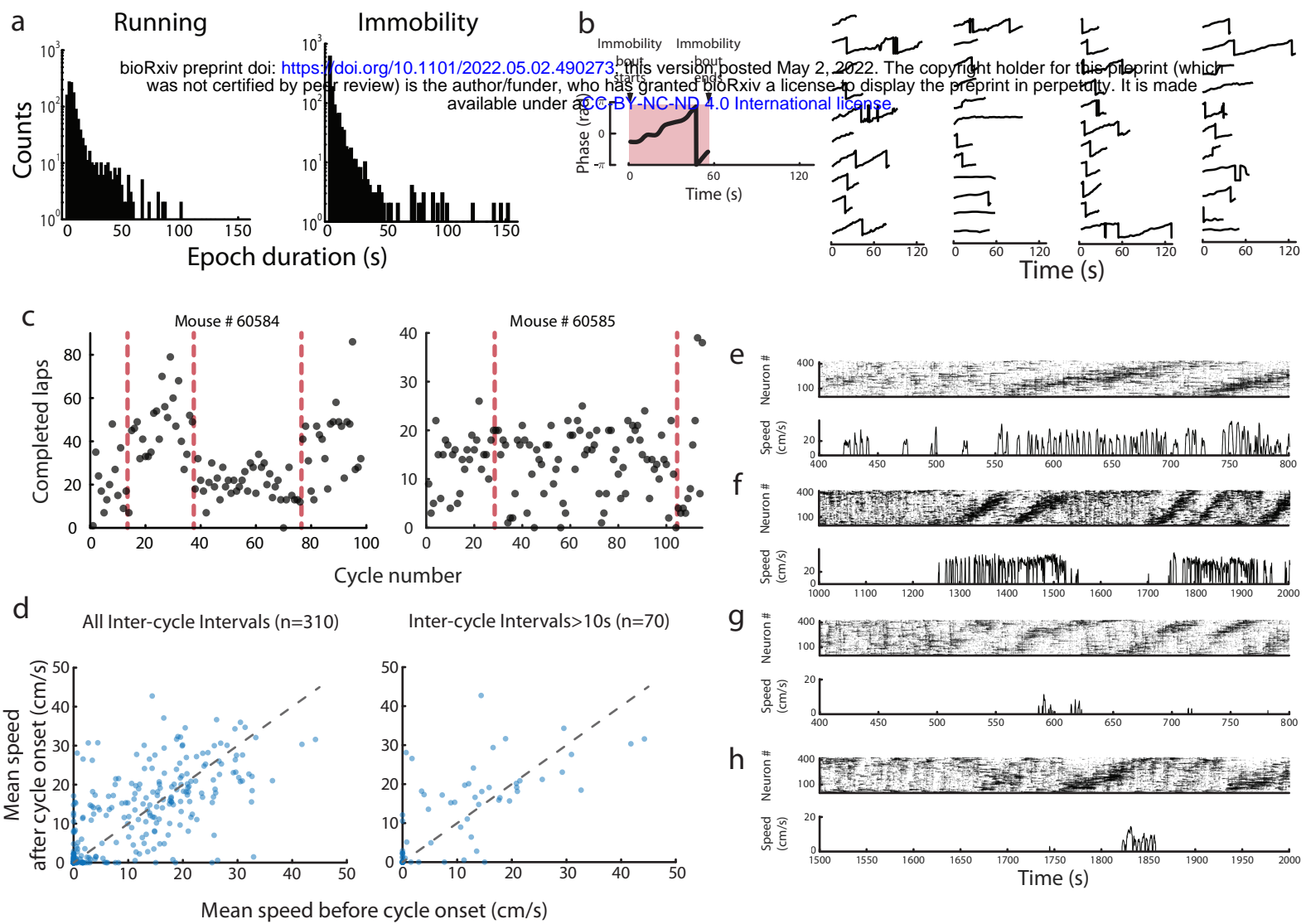
b

Mouse #	Ventro-lateral edge of the prism 3 mm M/L	Area occupied by GCaMP+ cells (μ m x μ m)
59911	2.03 mm D/V	600 x 486
59914	3.5 mm M/L 0.726 mm D/V	600 x 275
60355	3.7 mm M/L 1.2 mm D/V	550 x 470
60584	3.3 mm M/L 0.825 mm D/V	600 x 600
60585	3.2 mm M/L 1.3 mm D/V	600 x 405

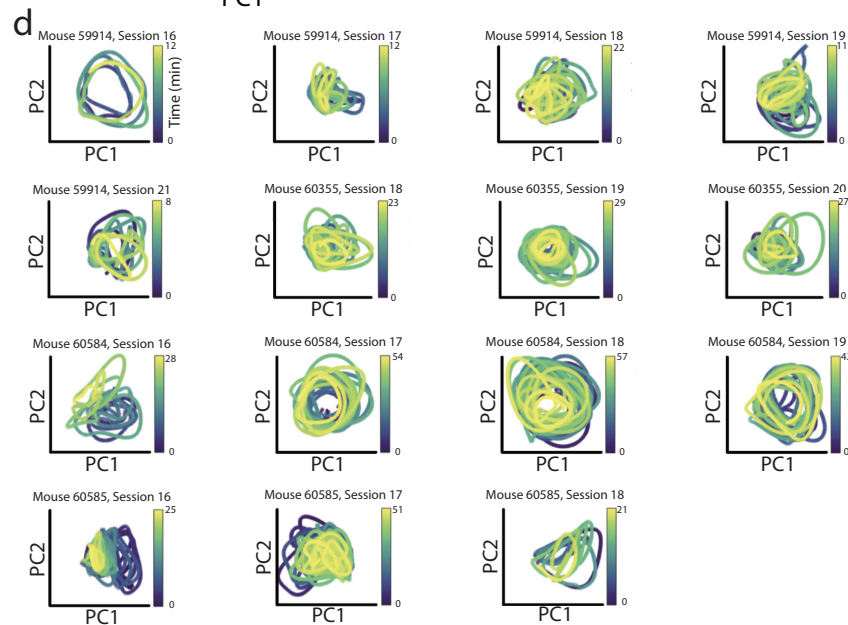
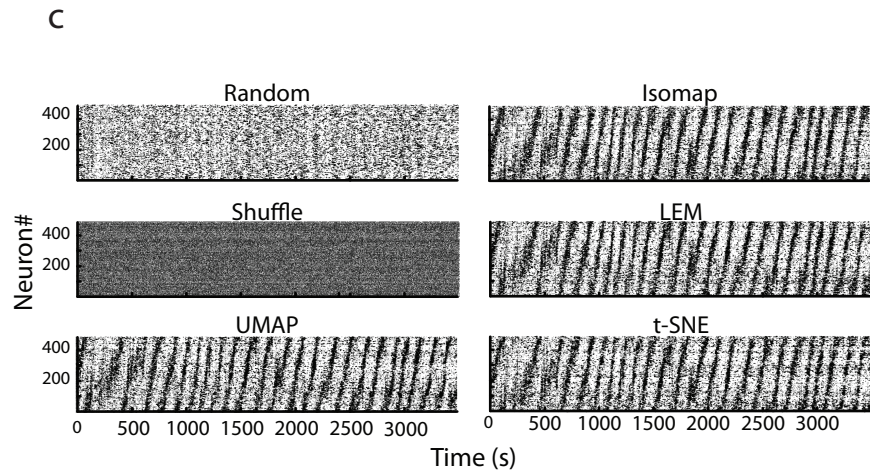
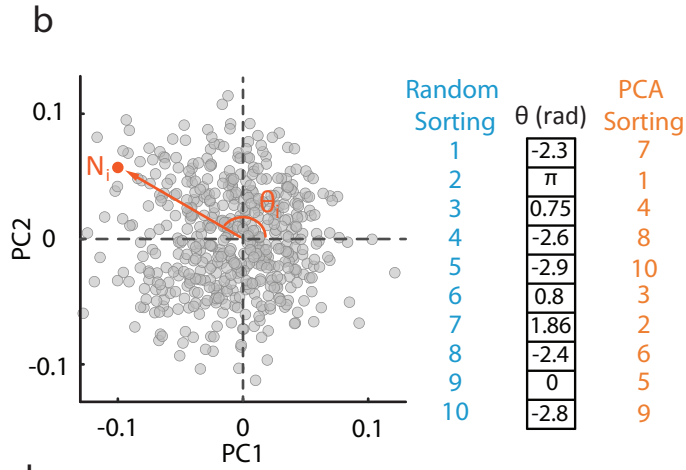
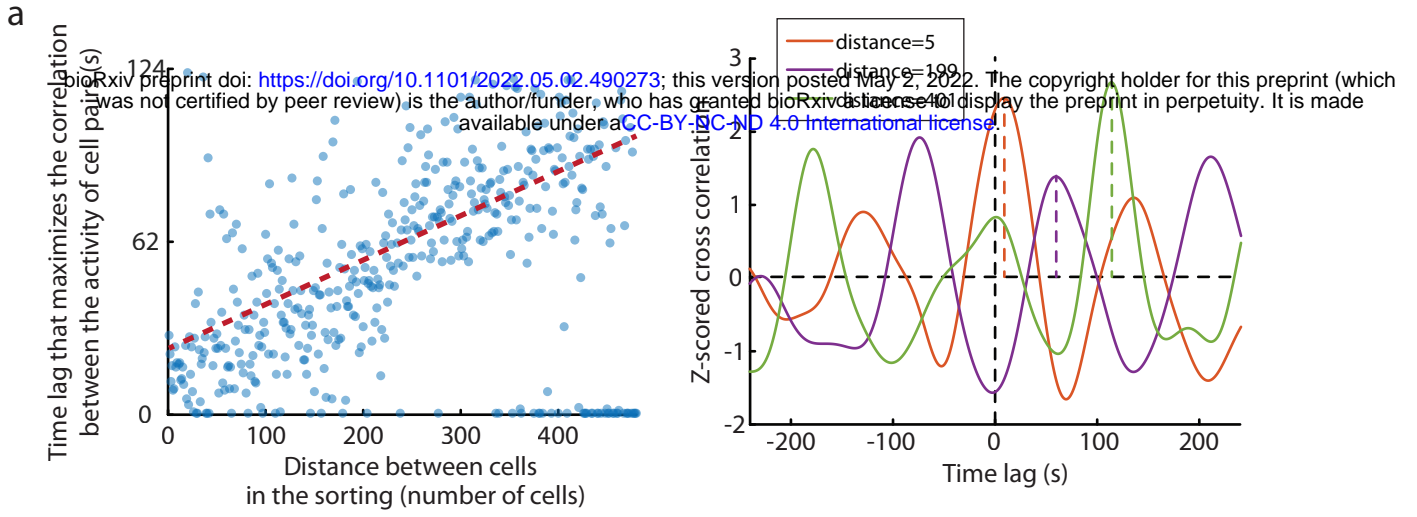
c



Extended data Figure 2

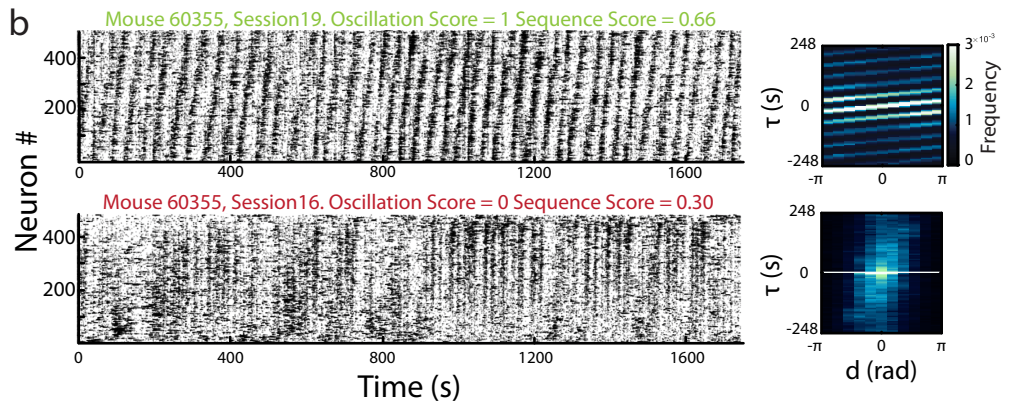
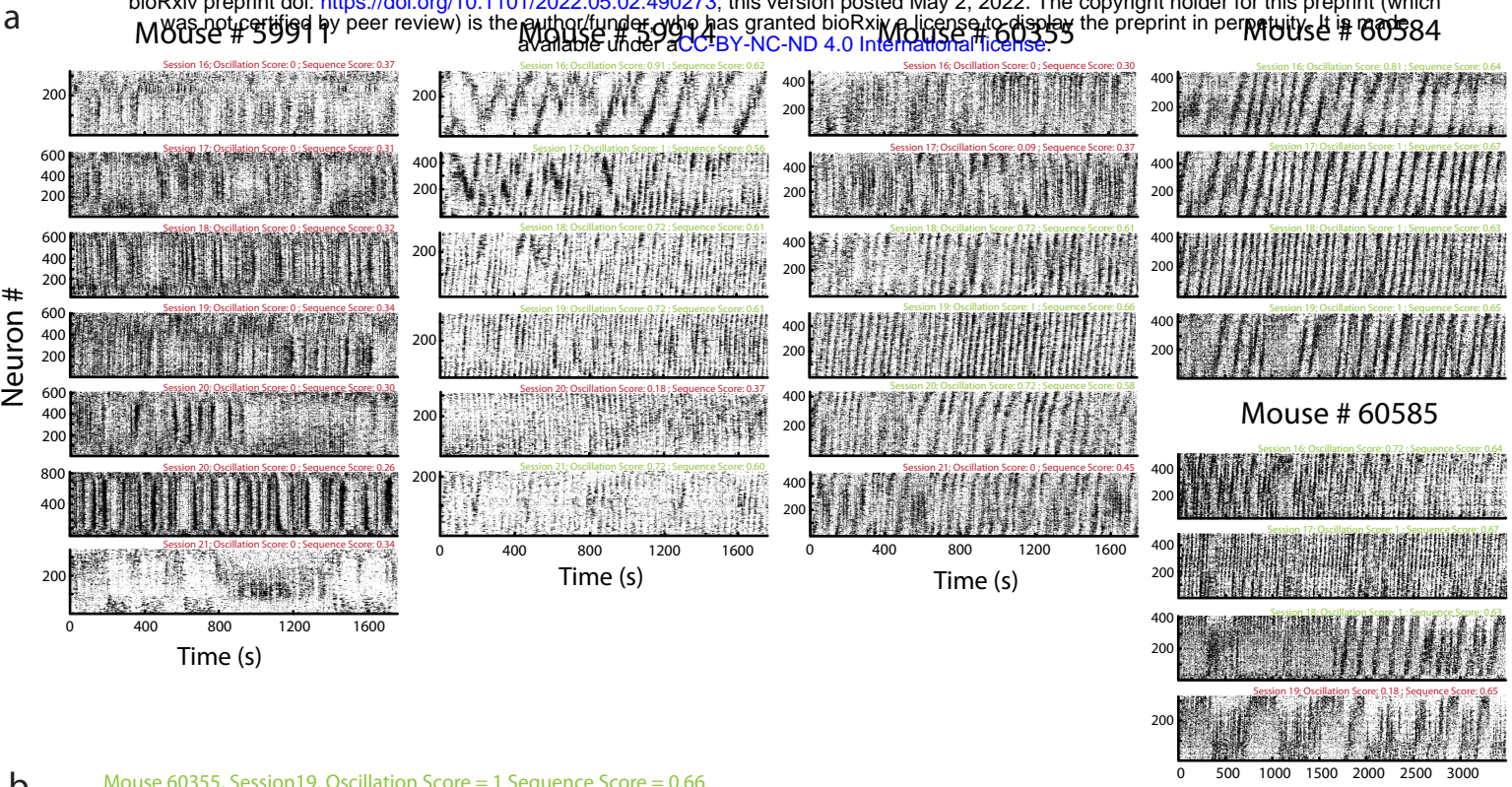


Extended data Figure 3

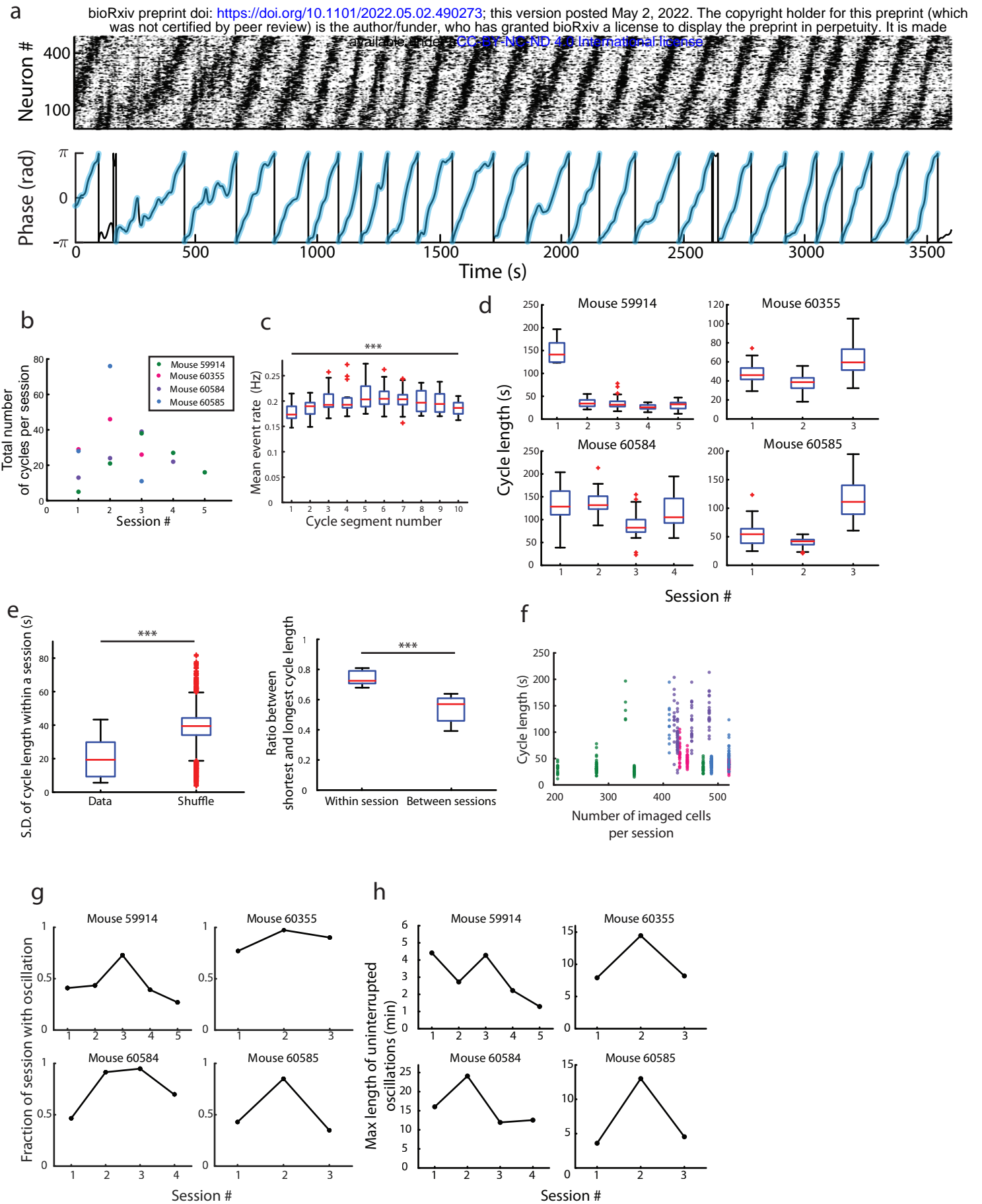


Extended data Figure 4

bioRxiv preprint doi: <https://doi.org/10.1101/2022.05.02.490273>; this version posted May 2, 2022. The copyright holder for this preprint (which was not certified by peer review) is the author/funder, who has granted bioRxiv a license to display the preprint in perpetuity. It is made available under aCC-BY-NC-ND 4.0 International license.

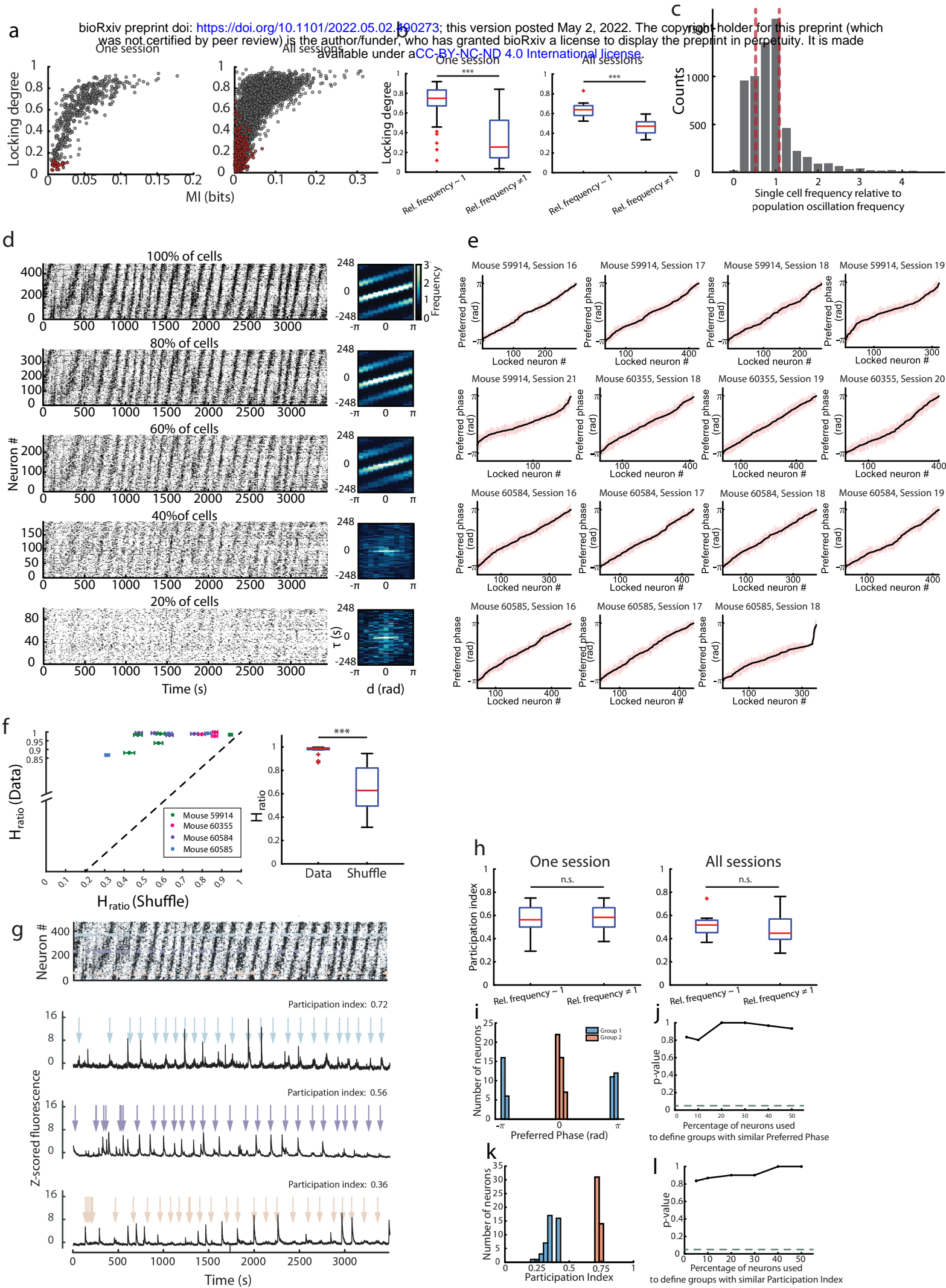


Extended data Figure 5

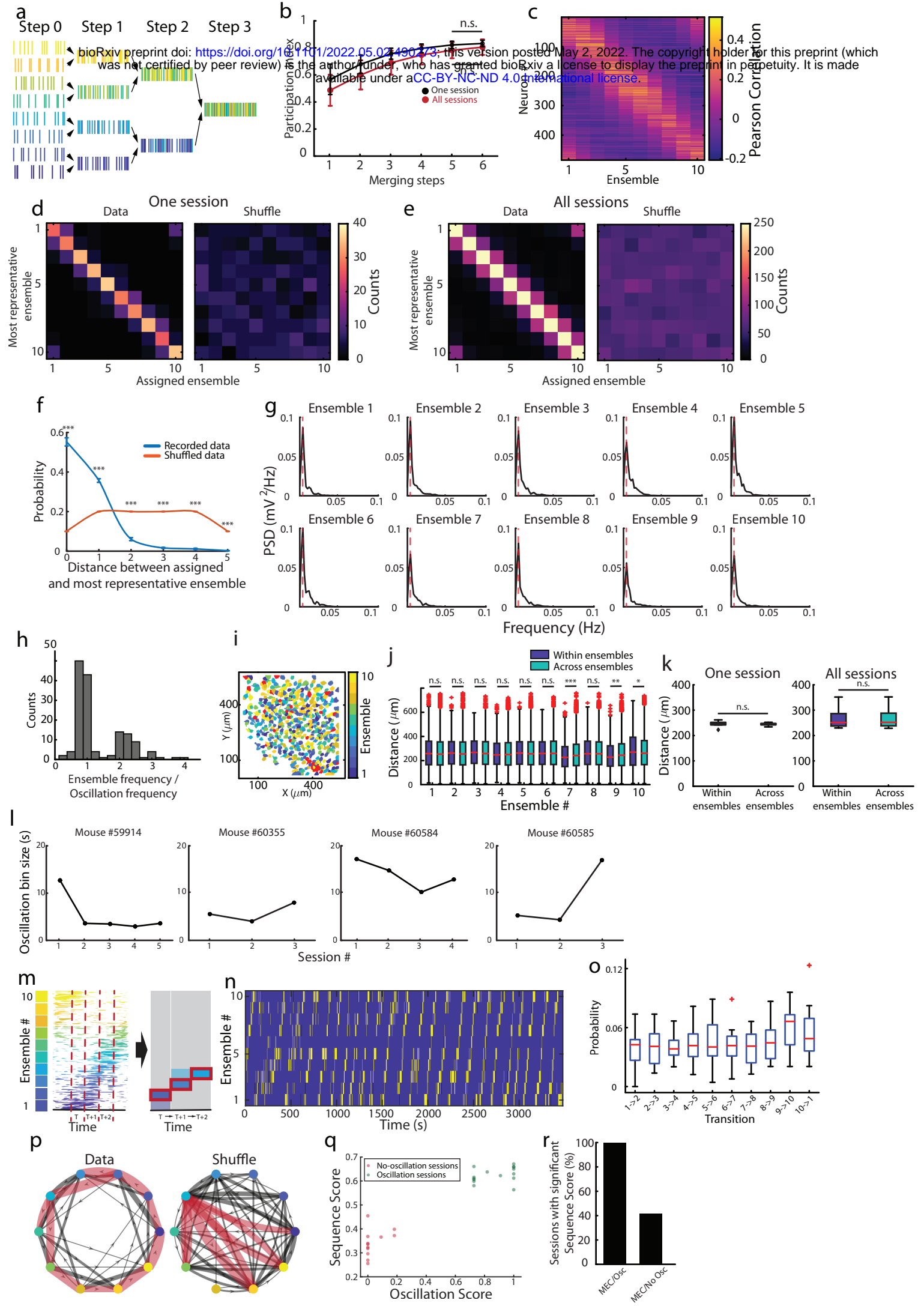


Extended data Figure 6

bioRxiv preprint doi: <https://doi.org/10.1101/2022.05.02.490273>; this version posted May 2, 2022. The copyright holder for this preprint (which was not certified by peer review) is the author/funder, who has granted bioRxiv a license to display the preprint in perpetuity. It is made available under aCC-BY-NC-ND 4.0 International license.



Extended data Figure 7

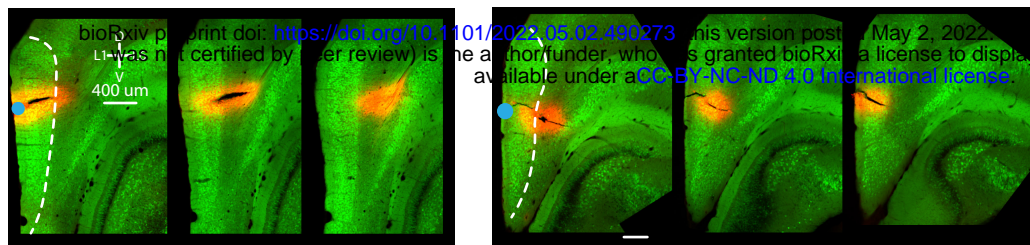


Extended data Figure 8

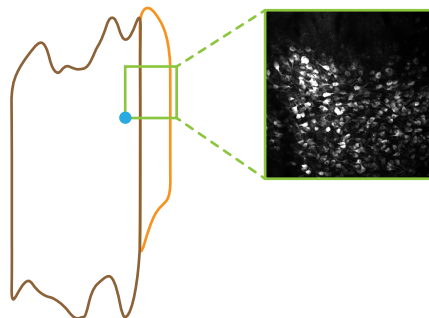
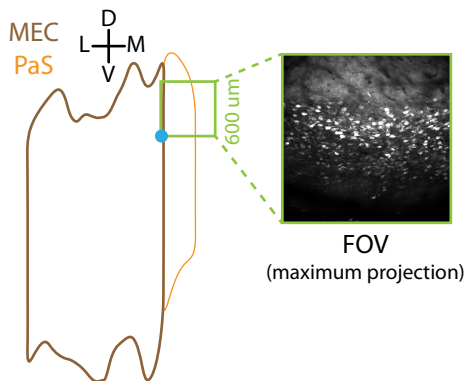
a

#59912

#60353

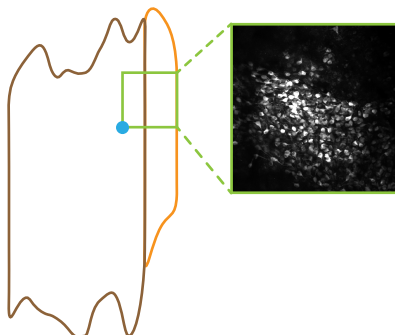
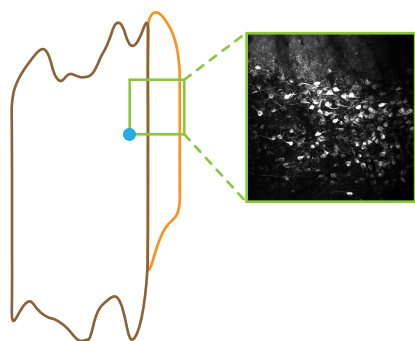
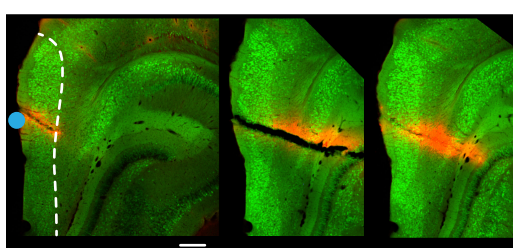
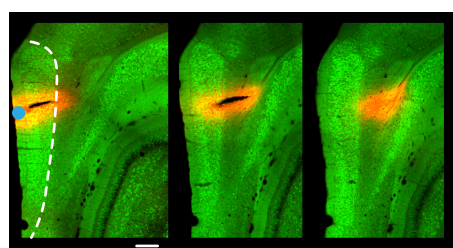


bioRxiv preprint doi: <https://doi.org/10.1101/2022.05.02.490273>; this version posted May 2, 2022. The copyright holder for this preprint (which was not certified by peer review) is the author/funder, who has granted bioRxiv a license to display the preprint in perpetuity. It is made available under aCC-BY-NC-ND 4.0 International license.



#60354

#60356

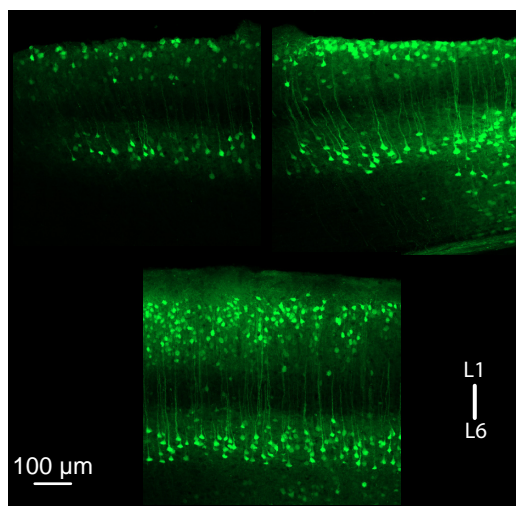


b

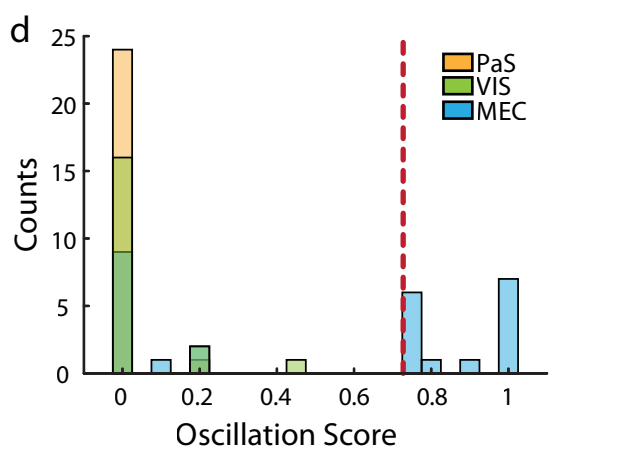
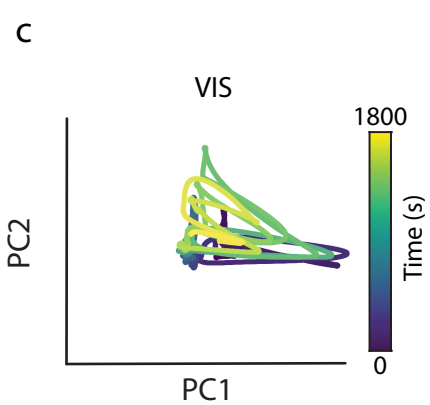
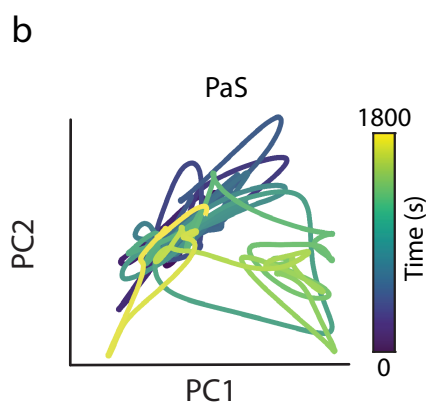
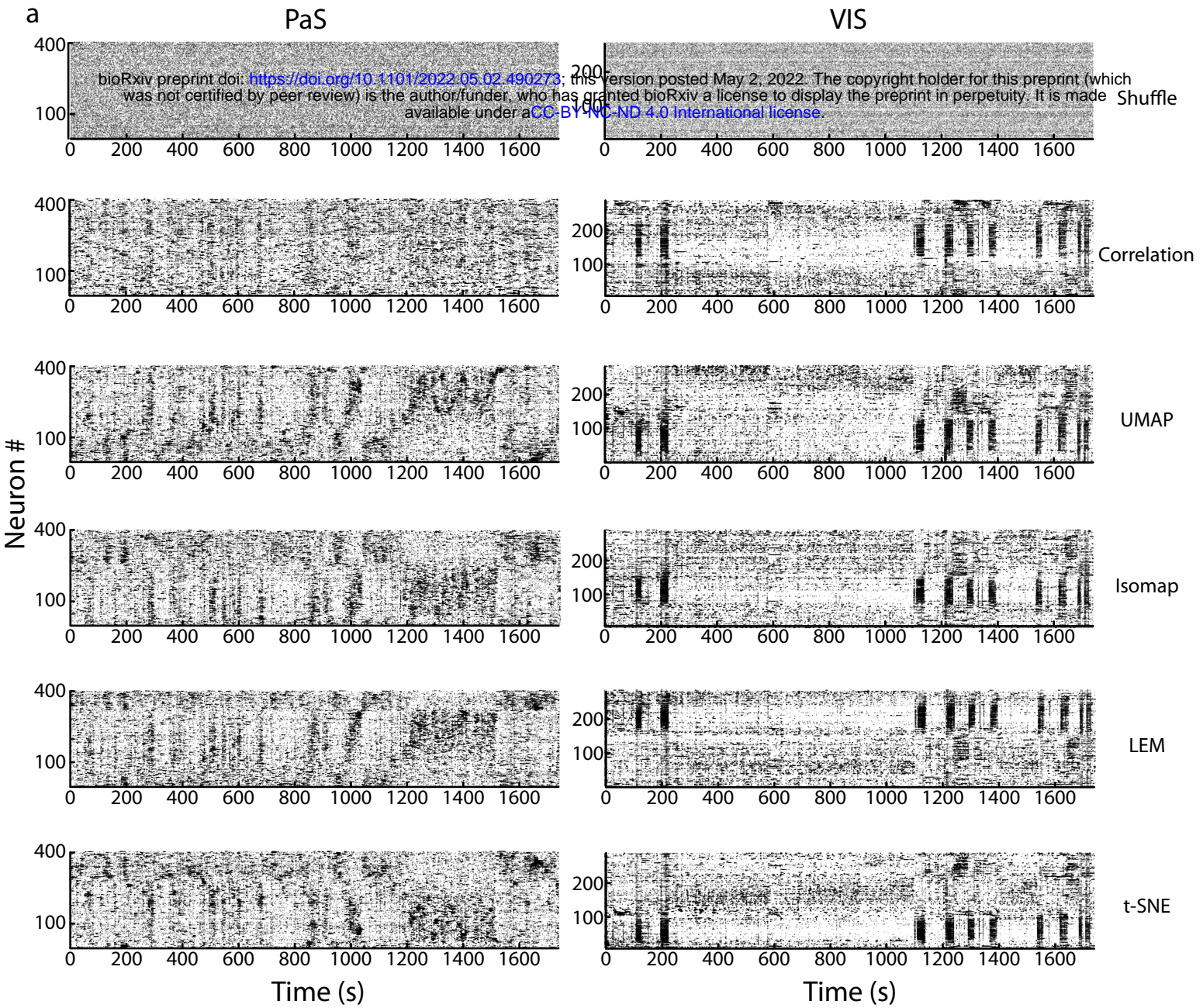
Mouse #	Ventro-lateral edge of the prism	Area occupied by GCaMP+ cells ($\mu\text{m} \times \mu\text{m}$)
59912	2.52 mm M/L 0.72 mm D/V	600 x 360
60353	2.64 mm M/L 1.12 mm D/V	600 x 493
60354	2.64 mm M/L 1.2 mm D/V	550 x 462
60356	2.7 mm M/L 1.12 mm D/V	520 x 520

c

VIS



Extended data Figure 9



Extended data Figure 10

